Carbide Derived Carbon from MAX-Phases and their Separation Applications

A Thesis

Submitted to the Faculty

of

Drexel University

by

Elizabeth N. Hoffman

in partial fulfillment of the

requirements for the degree

of

Doctor of Philosophy

September 2006

Dedications

This work is dedicated to my wonderful parents, Carol and Jeffrey Hoffman, who have provided never-ending support and encouragement from day one.

I also dedicate this work to my loving husband, Bradley Pickenheim. His reassuring presence has kept me grounded.

Acknowledgements

I greatly appreciate the assistance I received from numerous people throughout the course of this work. Foremost, I would like to thank my advisors, Prof. Michel Barsoum and Prof. Yury Gogotsi. Their enthusiasm and passionate approach to research is inspiring. I have learned so much from their experience and guidance, beyond the technical aspects of research.

I would also like to convey thanks to the other members of my thesis committee- Prof. Ihab Kamel, Prof. Guiseppe Palmese from Drexel University and Prof. John Fischer from the University of Pennsylvania. Their suggestions and insights along the way have improved to this work.

In addition to committee members, I would like to thank Prof. Gleb Yushin for his guidance and patience during this research. From fixing equipment to interpreting data, he was always willing to help and offer advice.

During the course of this work, several collaborations transpired. I would like to thanks Dr Tamer El-Raghy of 3one2 Inc. for supplying MAX-phase carbides. Additionally, I would like to thank Prof. Sergey Mikhalovsky, from the University of Brighton, and members of his research group including Dr. Carol Howell and Dr. Susan Sandeman for their efforts in ELISA testing to determine protein sorption. Also, I would like to thank Prof. Bogdan Wendler from Lódz Technical University for his expertise in the deposition of TiC for carbon membrane development.

Furthermore, I would like to thank Dr. Ranjan Dash for all his continual help and patience. I would also like to thank Mr. John Chimola, Ms. Z. Goknur Cambaz, Dr. Giovanna Laudisio, Mr. Daniel Vryhof, and Ms. Saujanya Yachamaneni of the carbide-derived carbon group for their time, questions, and suggestions on this work. I would also like to thank Mr. Aiguo Zhou, Dr. Surojit Gupta, Dr. Adrish Ganguly, and Mr. Sandip Basu from the MAX-phase group for their time, questions, and suggestions on this work. Additionally, I would like to thank Dr. Dmitry Filimonov, Dr. Vadym Mochalin, and Dr. Mickael Havel for taking time to discuss this work.

Many thanks to Mrs. Judith Trachtman for help with administrative issues throughout my time at Drexel University, and Mr. Andrew Marx for help with computer issues.

I would like to thank Prof. Roger Doherty for first introducing me to scientific research, and making it an enjoyable experience.

This work was funded by the National Science Foundation's IGERT Fellowship (DGE-0221664), along with Drexel University's Dean's Fellowship.

Table of Contents

List of Tables

List of Figures

Abstract

Carbide Derived Carbon from MAX-Phases and their Separation Applications
Elizabeth Hoffman
Michel W. Barsoum, PhD and Yury Gogotsi, PhD

Improved sorbents with increased selectivity and permeability are needed to meet growing energy and environmental needs. New forms of carbon based sorbents have been discovered recently, including carbons produced by etching metals from metal carbides, known as carbide derived carbons (CDCs). A common method for the synthesis of CDC is by chlorination at elevated temperatures. The goal of this work is to synthesize CDC from ternary carbides and to explore the links between the initial carbide chemistry and structure with the resulting CDCs properties, including porosity.

CDC was produced from MAX-phase carbides, in particular Ti_3SiC_2, Ti_3AlC_2, Ti_2AlC, and Ta_2AlC. Additionally, CDC was produced from Ta-based binary carbides, TaC and Ta_2C, and one carbo-nitride $Ti_2AlC_{0.5}N_{0.5}$. The CDC structure was characterized using XRD, Raman microspectroscopy, and HRTEM. Porosity characterization was performed using sorption analysis with both Ar and N_2 as adsorbates. It was determined the microporosity of CDC is related to the density of the initial carbide. The layered structure of the MAX-phase carbides lent toward the formation of larger mesopores within the resulting CDCs, while the amount of mesopores was dependent on the chemistry of the carbide. Furthermore, CDC produced from carbides with extremely high theoretical porosity resulted in small specific surface areas due to a collapse of the carbon structure.

To expand the potential applications for CDC beyond powder and bulk forms, CDC membranes were produced from a thin film of TiC deposited by magnetron sputtering onto porous ceramic substrates. The TiC thin film was subsequently chlorinated to produce a bilayer membrane with CDC as the active layer. Both gases and liquids are capable of passing the membrane. The membrane separates based on selective adsorption, rather than a size separation molecular sieving effect.

Two applications for CDC produced from MAX-phases were investigated: protein adsorption and gas separation. Sorbents capable of adsorbing large protein molecules efficiently are desirable for many medical applications, including the treatment of sepsis. Primarily mesoporous Ti_2AlC-CDC and Ti_3AlC_2-CDC were proven to adsorb a significant amount of proteins compared to two current carbon adsorbents. When tested for gas separation, CDC was capable of selectively adsorbing gases including SF_6, CO_2, CH_4, and H_2. However, the gases were not separated based on their size, but rather on their interaction with the CDC surface.

1 Introduction

Separation processes have exploded into a wide range of applications from the processing of food, fuel, water and waste within recent history. Mixtures of gases, liquid, and solids can be separated creating an endless range of possible applications. Historically, sorbents have been used for medicinal purposes in ancient times, to military uses starting in World War I. Furthermore, during World War II, membranes were first used to clean drinking water in Europe.

Over time, sorbents have improved and new separation applications have been discovered. Zeolites, having been invented in 1959 are now a $100 million industry [1, 2]. In the past two decades, new nanoporous materials such as pillared clays, sol-gel derived metal oxides, and mesoporous molecular sieves have been developed. Multiple forms of nanoporous carbon have also been discovered, including carbon molecular sieves, activated carbon fibers, carbon nanotubes, and graphitic nanofibers.

Modern drug delivery systems require membranes to control permeation of chemicals into the body. Further improvements in adsorption and separation processes will enable emerging energy technologies, such as fuel cells. As the world becomes more populated and industrialized, stricter environmental standards will require improved air and water quality, thereby providing challenges to further improved sorbents with enhanced selectivity and improved permeability.

This work explores the porous properties and separation ability of another new form of carbon, nanoporous carbon produced from metal carbides. The connection between initial carbide chemistry and resulting porosity of carbon was explored. A new method for producing a thin film multi-layer membrane with nanoporous carbon as the

active layer was developed, opening doors for future applications requiring thin film porous carbon. Furthermore, carbide derived carbon was investigated in two very different separation applications, protein adsorption and gas separation.

2 Literature Review

Various porous materials exist for separations processes [3]. Porous carbon in particular has proven to be a considerable industrial adsorbent [4]. Although numerous porous carbon are available for use, prior to the discovery of the material discussed in this work, a porous carbon derived from an inorganic precursor did not exist that has tunable porosity on the nanoscale. Carbide derived carbon is a porous carbon material with tunable porosity [5]. Although several materials are commercially used as membrane for separation, carbon membranes have been limited in their use.

2.1 Methods of Separation

The opposite of mixing, separation may be defined as a process that converts a mixture of two or more substances into products that differ in terms of composition [6]. Separation processes result in major production costs in chemical, petrochemical, and pharmaceutical industries; therefore, methods to improve the efficiency and selectivity of separation processes are desirable. [2] Several methods have been developed for separation processes. Two major routes for separation include adsorption and membrane processes [7].

2.1.1 Adsorption

The specific surface area of the adsorbent or sorbent, also known as a mass separating agent, is key to separation processes based on adsorption. Adsorption separation may be based on steric, kinetic, or equilibrium effects [2]. Similar to molecular sieves and zeolites, the steric effect occurs when the molecules are small enough and of proper shape to diffuse into the adsorbent, while other larger molecules are excluded and are not adsorbed. Kinetic separation is based on the differences in diffusion

rates of different molecules. The pore size is critical in kinetic separation and must be tailored to lie between the kinetic diameters of the two molecules that require separation. Separation based on the equilibrium effect involves the polarizability, magnetic susceptibility, permanent dipole moment, and quadrupole moment of the molecules within the mixture. [2]

2.1.1.1 Carbon

Carbon-based adsorbents have unique surface properties compared to other adsorbents since their surfaces are nonpolar or slightly polar [2]. Carbon sorbents are not fouled by moisture compared to other adsorbents, therefore stringent moisture removal is not necessary and carbon can be used as a sorbent for treatment of aqueous solutions. Due to carbon's large accessible internal surface area, it adsorbs more nonpolar and/or weakly polar organic molecules better than other sorbents. The heat of adsorption in carbon is generally lower for carbon sorbents, and therefore it requires less energy to remove molecules from carbon surfaces during regeneration [2].

Being a $1 billion industry [1], carbon has been used in several applications. In charcoal form, carbon has been used since at least 1550 B.C. in Egypt to remove toxins from the body [8]. Since that time, the sorption capabilities of carbon have been medically employed for a variety of applications including to the elimination of toxic by-products that cause anemia in cancer patients; to disinfect and deodorize wounds; to filter toxins from the blood in liver and kidney diseases; to purify blood in hemoperfusions; to treat poisonings and overdoses of aspirin, Tylenol and other drugs; to treat some forms of dysentery, diarrhea, dyspepsia, and colic; and to treat poisonous snake, spider and insect bites [8]. More recently its ability to adsorb cholesterol has been reviewed. [9]

A wide range of carbon sorbents are available. The following subsections briefly describe each type.

2.1.1.1.1 Activated Carbon

Activated carbon, manufactured since the 19th century, is the most commonly used adsorbent. [10] Production of activated carbon, generally in powder or pellet shape, includes: raw material preparation, low-temperature carbonization, and activation. Raw materials used to form activated carbon include wood, peat, coals, petroleum coke, bones, coconut shells and fruit nuts. [2] The raw materials are carbonized at 400-500 °C to eliminate contaminants, such as volatile matter, and then partial gasification at 800-1000 °C is performed to promote porosity and increase surface area. [2] To develop uniform porosity, a mild oxidizing gas, which has a surface reaction rate slower than the pore diffusion rate is used in the gasification reaction. In addition to gas activation, chemical activation has also been employed.

Chemical activation does not require a pre-carbonization step. Activators such as phosphoric acid, zinc chloride, or potassium sulfide are blended with the material, most commonly lignin based precursor such as sawdust. [10-14] The mixture is heated to 500-900 °C. Upon heating, the remaining chemicals are removed from carbon by water or an acid wash. The critical influence of the activation process on porosity was proven with the development of activation by molten KOH. During the activation process, KOH is mixed with coke and the mixture is subsequently heated for around 2 h at ~700-800 °C in an inert atmosphere. [15] Cage-like pores, generally less than 2 nm in diameter, develop during the activation. Generally the Brunauer-Emmett-Teller (BET) surface area is ≈ 2800 m^2/g, but can be as high as 4060 m^2/g. [15, 16]

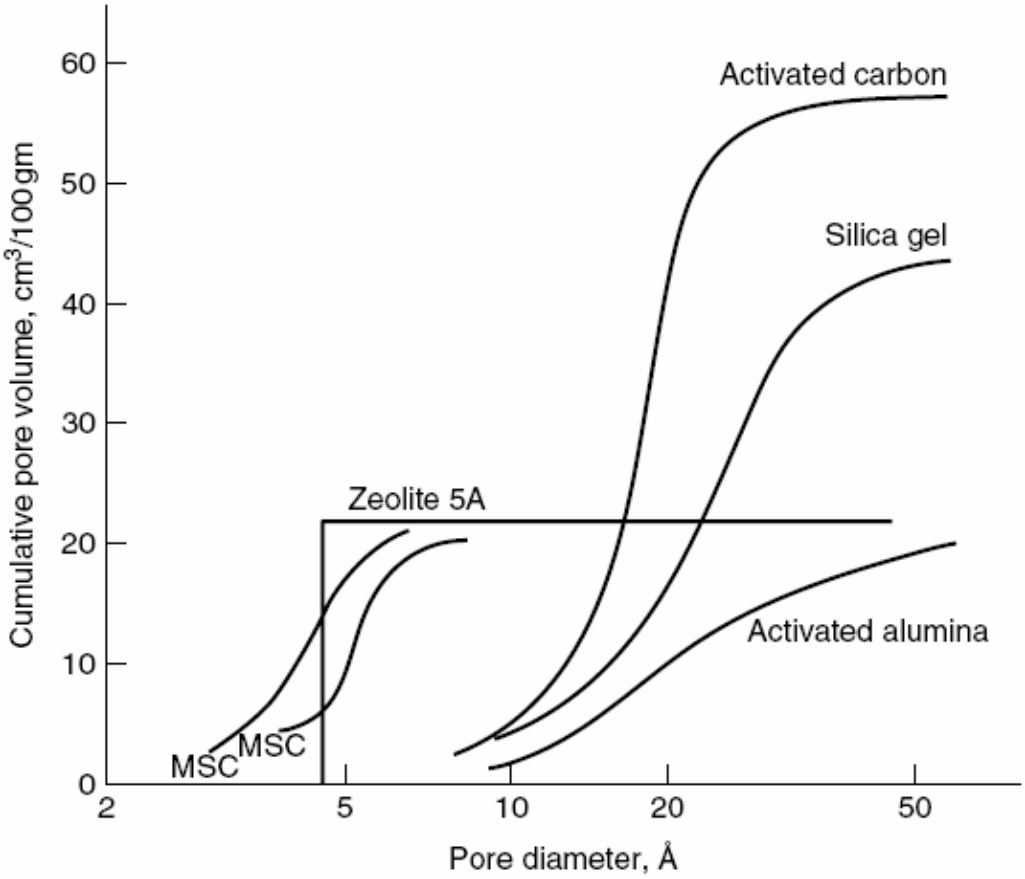

Figure 2.1 Pore size distributions of activated carbons, silica gel, activated alumina, carbon molecular sieves, and zeolite 5 Å [6].

Activated carbons consist of a broad range of BET specific surface areas (SSAs) between 300-4000 m^2/g. Often activated carbons have polymodal pore size distributions (PSDs). [2] The pore structure can be described as being a combination of numerous small pores, sometimes referenced as adsorption pores or dead-end pores, connected by larger pores, also known as transport or feeder pores. [2] Unlike some sorbents, activated carbons contain significant volumes of both micro- and mesoporosity, resulting in significant overall surface area (Figure 2.1).

2.1.1.1.2 Activated Carbon Fibers

Carbon fibers, having high tensile strengths and elasticity, are produced from polymeric fibers, cellulose, and pitches. [2] Following carbonization, they are activated typically by a gas activation process. Considerably more graphitic than activated carbons, carbon fibers have BET surface areas ranging from around 1000 m^2/g to over 2000 m^2/g. [2] Additionally, they have strong interactions with sorbates, due to a narrow and uniform pore size distribution; fast uptake and desorption because of small and uniform fiber diameters; conductive and more heat resistant due to their graphitic nature, and a high degree of flexibility in the shapes and forms of sorbents such as clothes and papers due to their high strengths and elasticity. Although activated carbon fibers have several advantageous properties, their use is limited because they are relatively more expensive. [2]

2.1.1.2 Zeolites

Over 40 zeolites occur naturally, and around 150 zeolites have been synthesized [2]. Zeolites are hydrated alumino-silicate minerals, with a structure capable of accommodating a wide variety of positive ions, such as Na^+, K^+, Ca^{2+}, Mg^{2+} and others. The cations are weakly bonded and can readily be exchanged. The zeolite structure is based on tetrahedra of silicon and aluminum, SiO_4 and AlO_4. [2] An example of a zeolite unit cell is given in **Figure 2.2**. Their chemical composition can be described as:

$$M_{x/n}((AlO_2)_x(SiO_2)_y)\cdot zH_2O$$

where x and y are integers with y/x equal to, or > 1, n is the valence of cation M, and z is the number of water molecules in each unit cell.

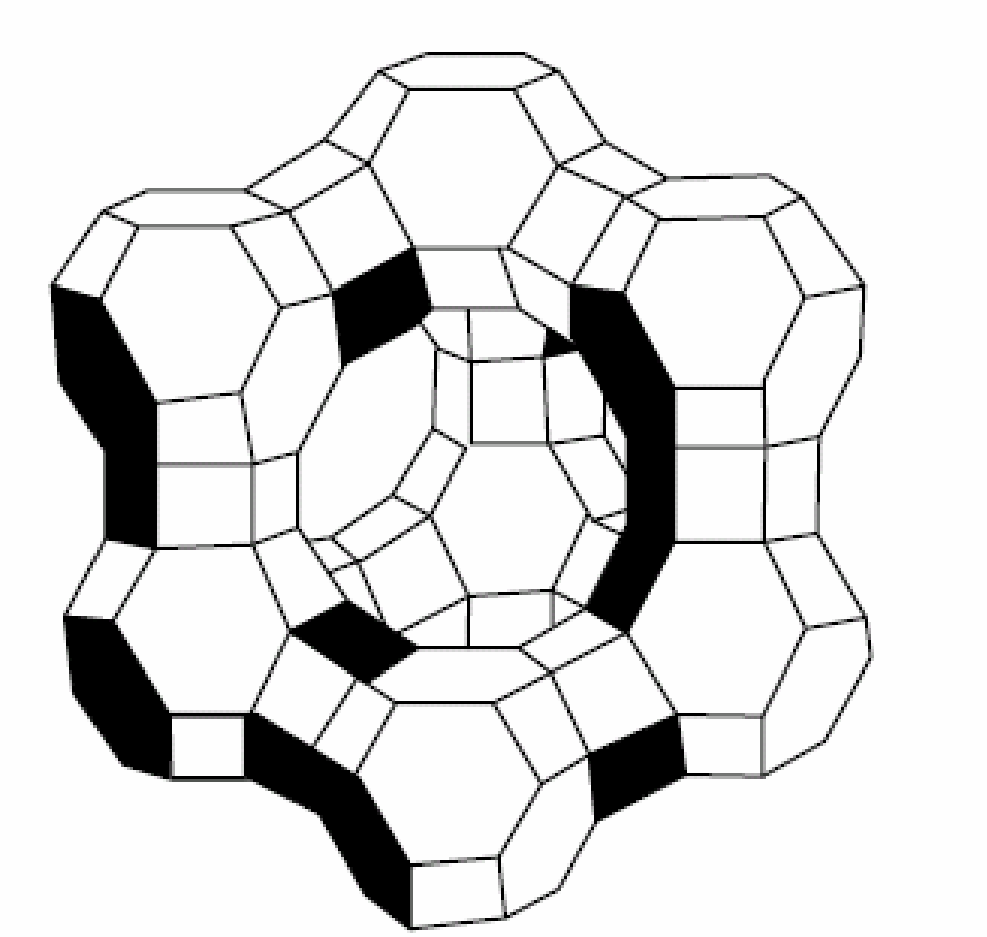

Figure 2.2 Unit cell of zeolite adsorbent. [6]

Based on the way the tetrahedra are arranged, more than 800 crystalline structures are possible. [2, 17] By the substitution of Al and/or Si for other elements, a molecular sieve can be produced. The largest pores available in zeolites are from 12-membered oxygen rings, resulting in a diameter of 8.1 Å. [2]

Zeolites have been utilized for gas separation applications, including N_2 and O_2 separation, and vapor separation applications, including H_2O and ethanol. [2] Additionally, zeolites are used for liquid bulk separations, for example, separation of fructose and glucose, and detergent-range olefins and paraffins.

2.1.1.3 Activated Alumina

Synthesis of activated alumina is performed by thermal dehydration or activation of aluminum trihydrate, $Al(OH)_3$. Activated alumina contains a significant amount of pores greater than 50 Å, in addition to micropores (defined here and in the literature as pores with diameters <2 nm). The pore structure depends on the heat-treatment. [2] Processes involved in heat-treatment include dehydration, crystal transformation, gas evolution, and sintering. The surface area generally found in activated alumina ranges from 250-350 m^2/g, with pore sizes ranging from 25-50 Å [18].

Applications for activated alumina include removal of HCl and HF from gases and liquids, removal of As^{5+}, PO_4^{3-}, Cl^- and F^- from water, and removal of acidic gases from hydrocarbons. [2]

2.1.1.4 Silica Gels

Mesoporous commercial silica gel sorbents can be formed either by polymerization of silicic acid or by aggregation of particles of colloidal silica. The amorphous structure of silica gel is comprised of small globular particles ranging from 10-20 Å in diameter. The surface area for silica gels ranges from 350-700 m^2/g, with pore sizes ranging from 20-140 Å. [18]

Silica gel is primarily used as a desiccant due to its relatively weak bonds with water and large mesoporosity volume. Therefore, silica gel is capable of adsorbing a large volume of water and is easily regenerated. [2]

2.1.2 Membranes

Membranes must be able to control the rate of permeation of different species. Solution-diffusion and pore flow models are two mechanisms for species permeation through membranes. In the solution-diffusion model, permeants dissolve into the

membrane, and diffuse through the membrane driven by the concentration gradients of permeants. Separation processes occur based on differences in diffusivity stemming from surface interactions with the membrane material. In the pore flow model, permeants flow through holes within the membrane by a pressure-driven convective flow. In this model, pore size relative to the permeant is critical. [17]

2.1.2.1 Carbon Membranes

Adsorption-selective carbon membranes (ASCMs) were first produced in the 1950s by compressing high-surface area carbon powders at high temperatures. [19] At the present, the membranes are generally fabricated either by directly pyrolyzing hollow-fiber materials or pyrolizing a thin layer of polymer coated on a macroporous support. Polymer precursors successfully used to form carbon membranes include polyimides [20, 21], cellulose acetate [22], polyvinylidene chloride (PVDC) [23, 24], and perfluoroalkoxy resin (PFA) [25]. ASCMs separate gas mixtures by selectively adsorbing one component within the mixture on the pore surface followed by surface diffusion of the adsorbed molecule across the pores. Typical pore sizes for ASCMs are 5-7 Å [26], and are practical in separating mixtures containing a strongly adsorbing (hydrocarbons, NH_3, SO_2, H_2S, and chlorofluorocarbons) and a weakly adsorbing (H_2, N_2, etc.) phase [27, 28]. More recently, molecular sieves carbon membranes (MSCMs) have been synthesized by pyrolysis of polymers such as polyimide or polyacrylonitrile membranes in inert atmosphere or vacuum at 500-800 °C [29, 30]. MSCMs, with a pore size < 4 Å, separate gas mixtures based on the shape and size of the molecules. Gas mixtures such as O_2-N_2, CO_2-N_2, and CO_2-CH_4, can be effectively separated. [31-33]

A recent drive has occurred to develop carbon, as well as other inorganic membranes, due to a superior combination of permeability and selectivity, as well as their resistance to high temperatures and corrosive environments. [26] While having exceptional separation properties for gas mixtures, carbon membranes are brittle and difficult to produce defect-free on a large scale. [17] Additionally, the cost of carbon membranes is 1-3 orders greater than polymeric membranes. [34] Compared to cellulose acetate, PFA, and other polymers, phenolic resins are a low cost polymer and have been successfully tested for gas separation applications. [35, 36]

In measuring the gas permeation properties of carbon membranes, several parameters will inflence the resulting selectivity and permeability of gas mixtures, including polymer precursor, pyrolysis methods, and post-treatment conditions. [17]

Additionally, when carbon membranes are produced by pyrolysis of amine polymers, the amine precursor has an influence on the resulting carbon porosity. Carbon layers have been synthesized from tetramethlammonium bromide (TMAB), tetrapropylammonium bromide (TPAB), and cetyltrimethylammonium bromide (CTAB) with pore sizes of 4 Å, 5 Å, and 5.5 Å, respectively [37].

The pyrolysis temperature has an effect on porosity, and subsequently molecular permeation. The influence of pyrolysis temperature in carbon membranes produced by pyrolysis of poly(2,6-dimethyl-1,4-phenylene oxide) (PPO) deposited on macroporous alumina ceramic supports was shown to influence the permeance of CO_2 through the carbon membranes derived from PPO ranges between ~$1x10^{-7}$ to $1x10^{-8}$ mol/m^2-secPa depending on the pyrolysis temperature, see Figure 2.3a. Also, an increase in the

permselectivity of a CO_2/CH_4 gas mixture occurred at low pyrolysis temperatures to peak at 973 K, then decreased at higher temperatures, see Figure 2.3b [37, 38].

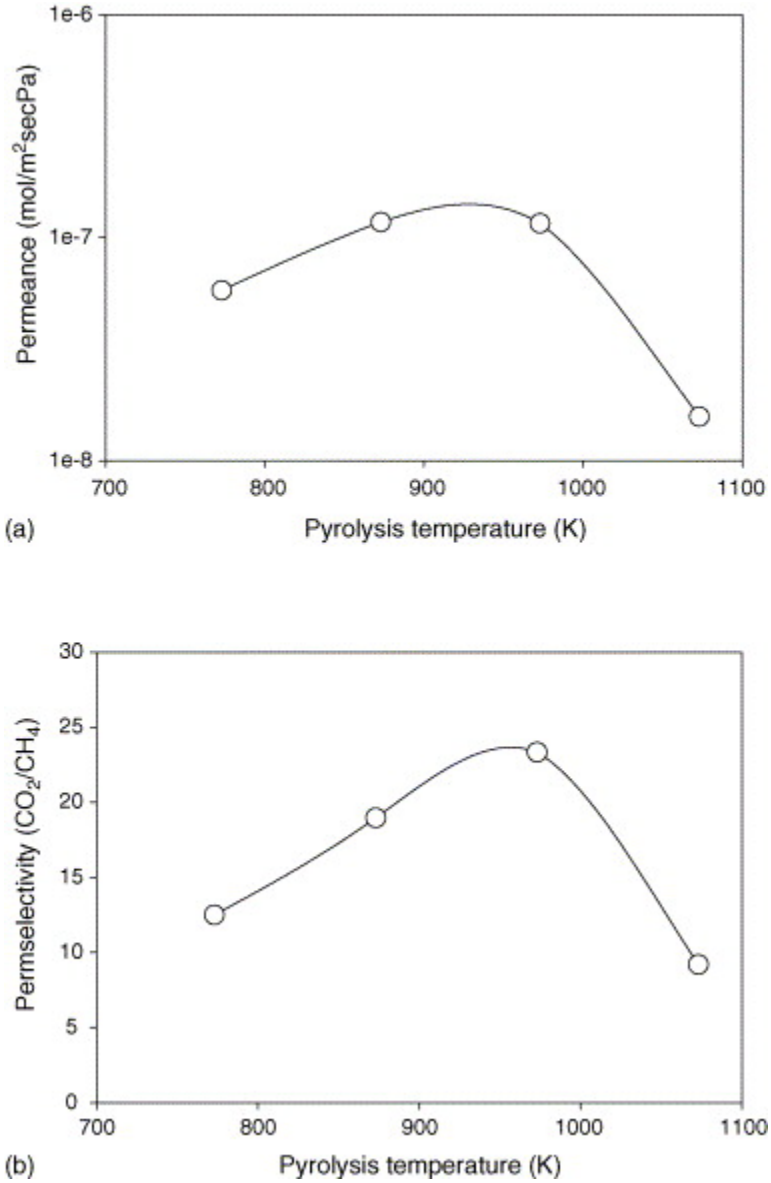

Figure 2.3 Influence of pyrolysis temperature on the, (a) permeation performance of CO_2, (b) permselectivity of CO_2/CH_4 [38].

Carbon membranes with a thickness of 14.2 μm were produced from poly(furfuryl alcohol) attached to a porous stainless steel support have reported permeances between 10^{-12} and 10^{-9} mol/m^2/s/Pa when measured between 25-225 °C and over a pressure range of 100-700 kPa. Heats of adsorption were found to be 2.06, 5.87, 4.12, 5.89, and 2.19 kcal/mol for He, N_2, O_2, Ar, and CO_2 respectively. [39] The work concluded that gas transport occurred through micropores with a pore size of 0.5 nm, as well as through a few larger defect pores with pore diameters around 50 nm.

It is, however, possible to produce a defect-free carbon membrane by infiltrating microporous carbon within the pores of a mesoporous support. For example, a thin phenolic resin can be applied to a mesoporous γ-Al_2O_3 support using a dip-coating process. Once fully cured, the polymer layer can then be carbonized at 700 °C to form microporous glassy carbon [40].

2.1.2.2 Metal Oxide Membranes

Metal oxide membranes made from alumina, titania, or silica have been developed for ultrafiltration and microfiltration applications. Ceramic membranes are advantageous since they are stable at high temperatures and are chemically inert. [17] They are often used for food, biotechnology, and pharmaceutical applications were membranes are subjected to steam sterilization and aggressive cleaning solutions. Pore diameters range from 0.01 to 10 μm and are generally made by slip coating-sintering methods. [17] In the latter process, a porous ceramic support tube is made by pouring a dispersion of fine-grain ceramic powder and a binder into a mold and sintering at high temperatures. Since the pores between the interparticle porosity in the support ceramic are large, one surface of the tube is then coated with a suspension of finer particles in a

solution of cellulosic polymer or polyvinyl alcohol, which acts as a binder and viscosity enhancer to hold the particles in suspension. [41] This mixture is called a slip suspension, and when it dries and is sintered at high temperatures, a layer of fine microporous surface remains. This process is used to make pores from 100-200 Å. [41, 42] Sol-gel processing has been used to form membranes with pores of 10-100 Å. [43]

2.1.2.3 Metal Membranes

Metal membranes are advantageous for high-temperature membrane reactor applications. Hydrogen, for example, is capable of permeating into several metals including tantalum, niobium, vanadium, nickel, copper, iron, and platinum. [17] The metal membrane must remain at high temperatures for fast gas permeation and the prevention of hydrogen embrittlement. Oxygen, although having a lower permeation rate compared to hydrogen, is also known to permeate metal membranes.

2.1.2.4 Polymer Membranes

Polymer membranes are widely used for gas separation applications since they can be made extremely thin, while being defect free, to provide economical fluxes. [17] Early techniques for the production of polymeric membranes include solvent evaporation. Later, solvent evaporation was combined with absorption of water vapor to produce microfiltration membranes. [17]

2.1.2.5 Multi-layer Composite Membranes

To increase the permeation fluxes while maintaining membrane strengths, a multilayered composite membrane has been developed. [17] Generally, a microporous support membrane made from a tough glassy material is coated with a thin layer of selective polymer, often a different material from the support. Additional protective

layers, often made of silicone rubber, can be added to protect the selective layer and seal any defects. [17]

Multi-layer composite membranes using carbon as the selective layer opposed to a porous polymer has also been developed. Nanoporous carbon layers were formed on porous stainless steel supports by pyrolysis of polyfurfuryl alcohol deposited by a spin coating method. [44]

2.2 Carbide Derived Carbon

Microporous carbide derived carbon (CDC) is formed from the etching of metals and metalloids from metal carbides. [5, 45, 46] Commonly, metals are etched via high temperature halogenation reactions resulting in the formation of metal halides and porous carbon. Halogens including Cl_2, Br_2, F_2, and I_2 along with their compounds such as HF, CCl_4, and many others can be used to produce CDCs. The porosity of CDC is dependent on the halogen chosen for removal of metals and metalloids. [47] CDCs can also be formed by hydrothermal leaching and reaction of certain metal carbides with inorganic salts.[5] Most commonly, chlorination is used as a synthesis route for CDC. The chlorination process has been used to produce metal chlorides from metal carbides since 1918, while the remaining carbon was overlooked [48]. In the 1950s, the remaining amorphous carbon was investigated [49], and by the 1970's, it was determined that the residual carbon was a porous material containing significant quantities of pores less than 2 nm. [50] Attention is now focused on the formed carbon, with numerous binary carbide powders including Al_4C_3 [51], B_4C [52], Cr_3C_2 [53], HfC [53], Mo_2C [53], NbC [53], SiC [54], TaC [53], TiC [55], VC [53] and ZrC [56] explored as precursors for CDCs. In addition to powders, CDC has been synthesized from other carbide forms including bulk,

nano-wires [57], and whiskers [58]. Additionally, bulk samples have been partially chlorinated to produce thin-film CDC layers [59, 60].

Several carbon structures can form upon chlorination ranging from amorphous carbon, turbostratic graphite, to highly ordered graphitic carbon depending on chlorination temperature [61], as well as the chemistry of the initial carbide [62]. As a result of the variations in structure, the degree of porosity varies depending on the metal carbide used as precursor and the synthesis parameters, in particular temperature [51, 52, 56, 63, 64]. Depending on the chlorination temperature and precursor carbide used in the synthesis of CDC, BET surface areas above 2000 m^2/g can be achieved [52]. The porosity formed during chlorination is interconnected since a path is required for, 1) chlorine to interact with the carbide, and, 2) the formed metal chlorides to leave the material.

Recently, initial attempts were taken to study porosity in ternary carbides based CDCs, and it was proven that sub-nanometer control of porosity in CDCs can be performed through the use of argon adsorption technique, see Figure 2.4. The structure of the resulting CDC was studied using transmission electron microscopy (TEM) and Raman spectroscopy. It was found that similar to CDC made from binary carbides, the carbon structure transforms from amorphous carbon at low synthesis temperature, to a more ordered turbostratic structure containing carbon ribbons which can be seen in the TEM micrographs, see Figure 2.5 [64]. Similar to what was found in the work on binary carbides, as a result of the structure change in CDC with varying chlorination temperature, the porosity was found to vary. Pore size was found to increase with increasing chlorination temperature as measured by both CH_3Cl adsorption and small

angle x-ray scattering (SAXS), Figure 2.6. In Ti_3SiC_2 derived carbon produced at temperatures greater than 700 °C, Type IV isotherms were measured by gas adsorption, denoting the presence of mesoporosity. While the pore volumes were similar for CDC produced at 700, 900, and 1100 °C, the pore size distributions were different. Larger amounts of mesopores were found in CDC produced at higher temperatures [64]. Despite the initial investigations into Ti_3SiC_2-CDC, no further ternary carbides were explored. Additionally, no systematic study on the effect of ternary carbide chemistry has been performed.

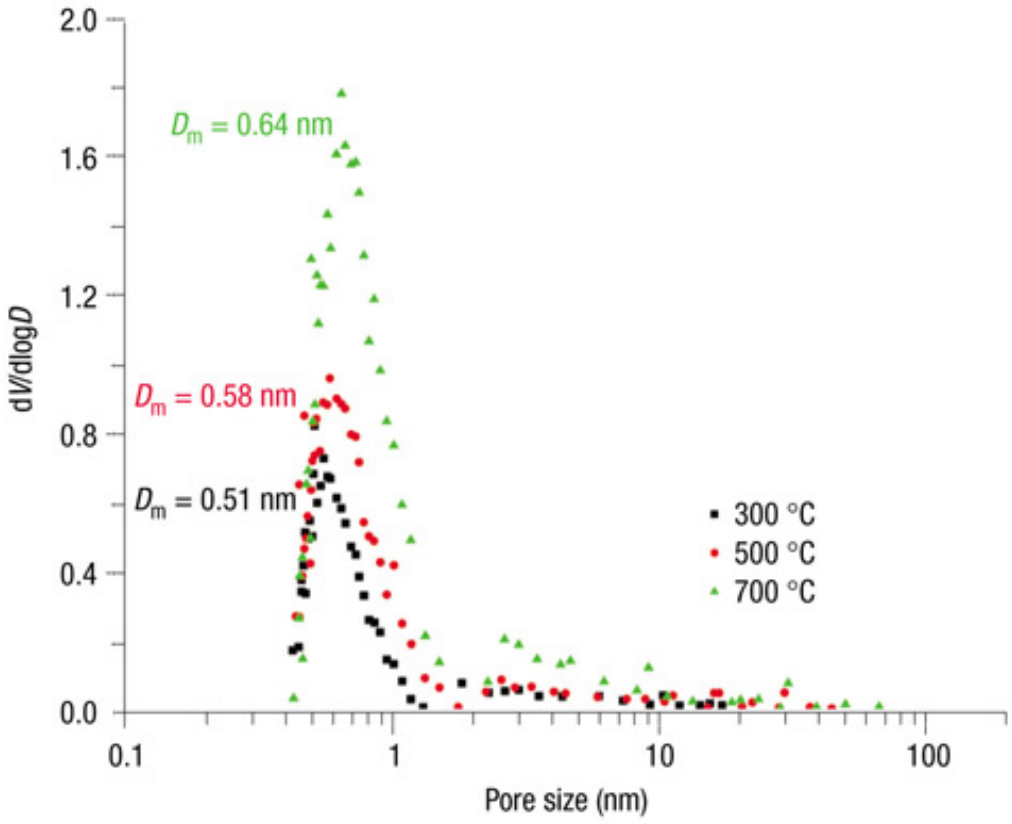

Figure 2.4 Pore size distributions for Ti_3SiC_2-CDC chlorinated at 300 °C, 500 °C, and 700 °C [64].

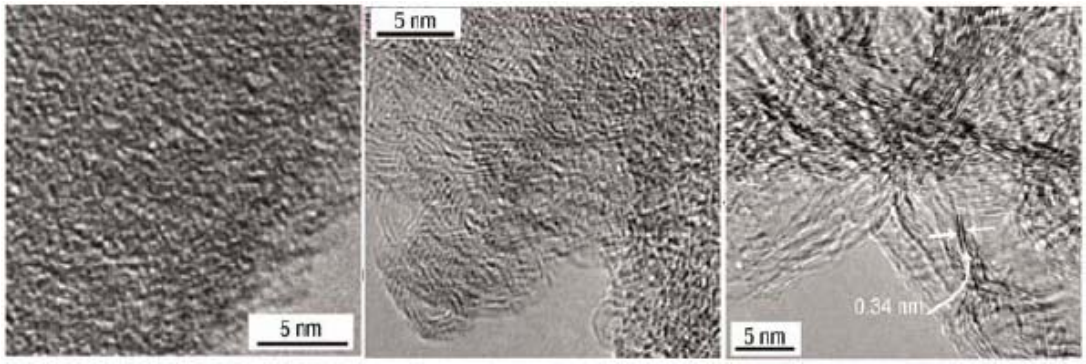

Figure 2.5 Transmission electron microscopy images of CDC produced from Ti_3SiC_2-CDC at chlorination temperatures of a) 300 °C, b) 700 °C, c) 1200 °C [64].

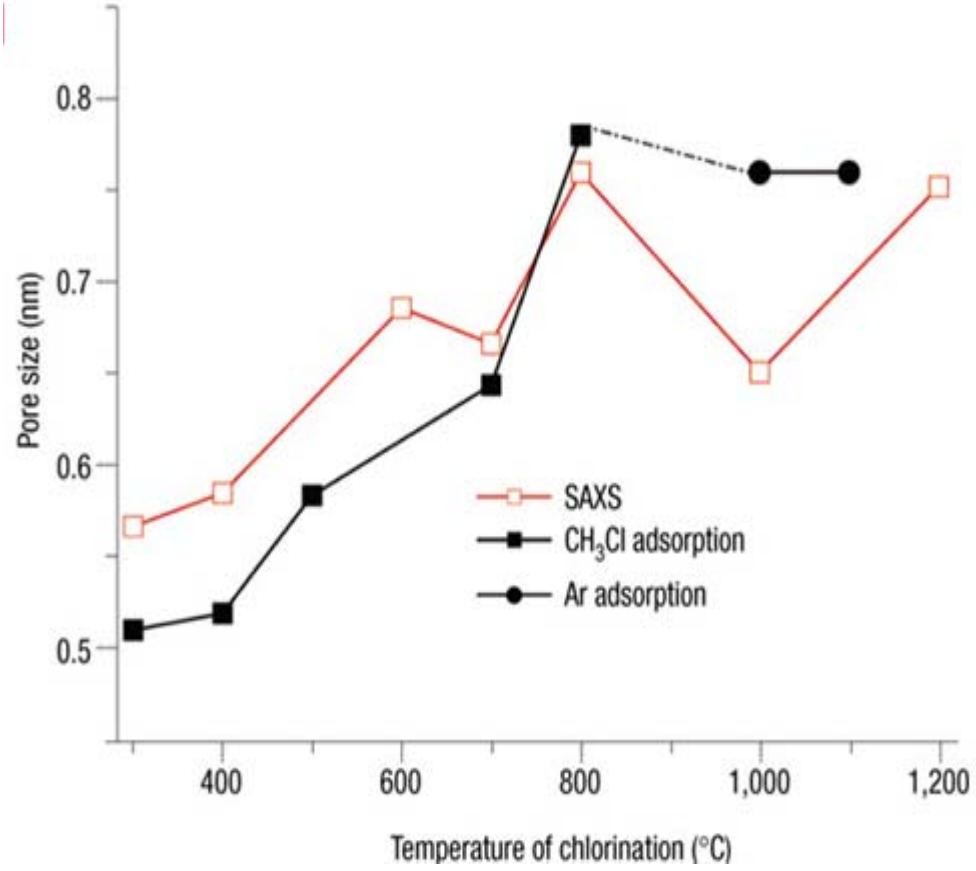

Figure 2.6 Pore size comparison of SAXS and CH_3Cl/Ar adsorption on Ti_3SiC_2-CDC over varying chlorination temperatures [64].

Due to their tunable porosity and high surface areas, CDCs have been investigated and shows promise for a variety of uses including supercapacitors [65], gas storage [63],

and tribology [66]. Investigations of thin film tribology applications found CDCs are self lubricating, providing a low coefficient of friction, particularly in dry nitrogen environments. [67] Electrochemical studies have correlated increased specific capacitance to CDC containing large micropore volumes, while also identifying pore shape of CDCs affect the electrochemical properties [65]. Although tunable porosity and high surface area are advantageous for separation applications, CDCs have not been investigated for this purpose to date due to the lack of a porous membrane comprised CDC.

2.3 Objective

Although a significant effort has been placed into understanding the porosity of CDCs, to date, little is known about the carbon derived from ternary carbides, and no systematic study on the effect of carbide chemistry has been performed. The objective of this work is to synthesize and characterize carbon derived from select ternary carbides residing in a group of carbides known as MAX-phase carbides. In characterizing the CDCs from these select carbides, parameters upon which pore size depends will be determined. In addition to understanding the effect of carbide chemistry on the resulting carbon porosity, investigations into CDC's separation capacity as an adsorbent and a membrane will be examined. To understand CDC's ability to separate as a membrane form, CDCs must be synthesized as membranes. Therefore, synthesis routes for the production of CDCs membrane will be explored.

3 Materials and Experimental Details

3.1 Carbide Selection

Several ternary carbides, binary carbides, and a carbo-nitride were selected for CDC synthesis.

3.1.1 MAX Phase Carbides

The MAX phases are a group of ternary carbides/nitrides with $M_{n+1}AX_n$ chemistry where *M* is an early transition element, *A* is an A-group element, *X* is carbon and/or nitrogen, and *n* is an integer 1, 2, or 3 [68]. The MAX phases are readily machinable and possess a lamellar structure. Several different structures exist within the group depending on the value of *n*, thereby forming different unit cells (Fig. 3.1) [68]. The carbon spacing in the 211 structure is the most evenly spaced, followed by the 312 and 413 structures. The ratio of the unit cell height to its width, *c*/*a*, for a particular structure gives an estimate of the uniformity of the carbon spacing. A material with a ratio approaching 1 has more uniformly distributed carbon than a material with a higher ratio. Also, assuming the transformation from carbide to carbon is conformal; the carbon density within the initial carbide should suggest the carbon density in the resulting CDC. Figure 3.2 shows that MAX-phase carbides tend to cluster together according to their respective structure, 211, 312, or 413 in terms of initial carbon density and c/a ratio.

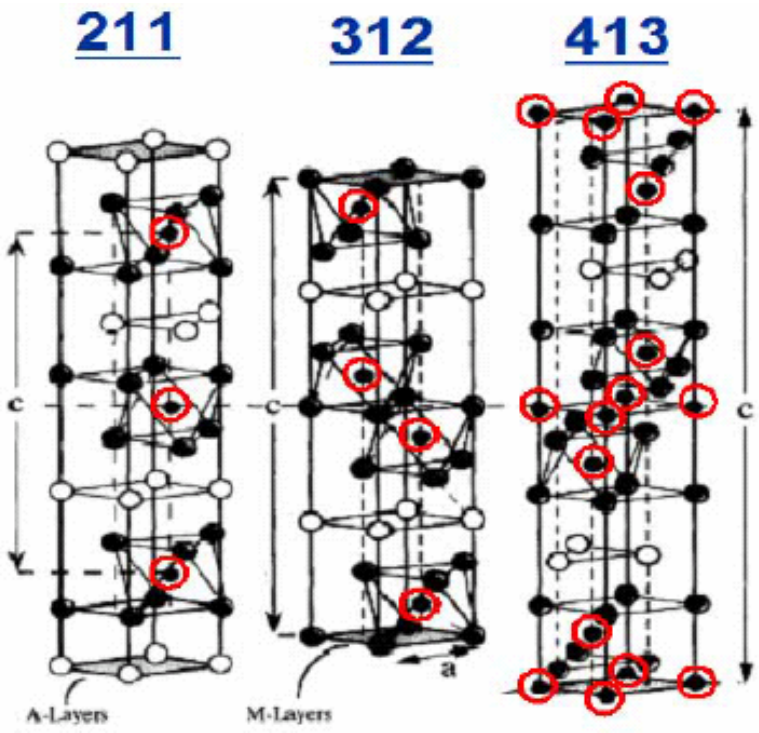

Figure 3.1 Unit cell structures of MAX-phase carbides. Carbon atom locations within the structures are circled. The unit cell width, *a*, and length, *c*, are shown.

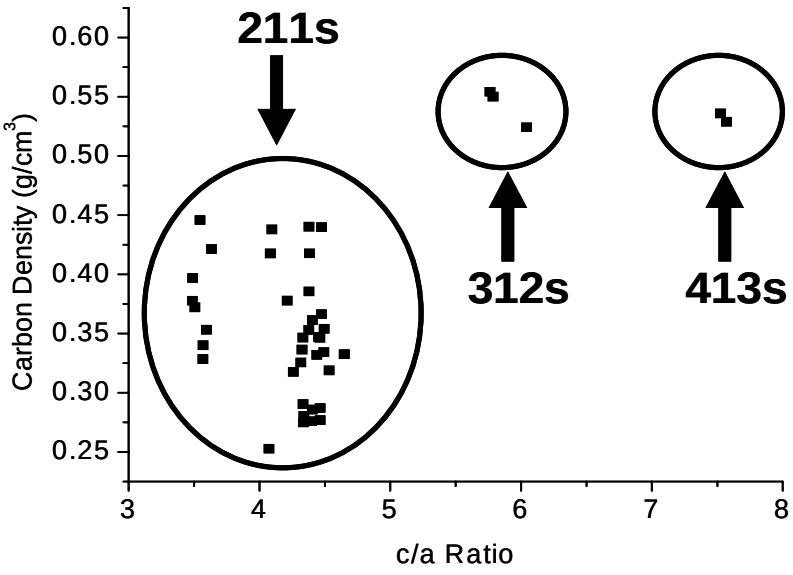

Figure 3.2 Carbon density of the initial carbide versus the c/a ratio of the initial carbide.

Over 40 different MAX phases carbides exist [68]. To evaluate the effect of carbide chemistry and stoichiometry, the following MAX-phase carbide powders were investigated:

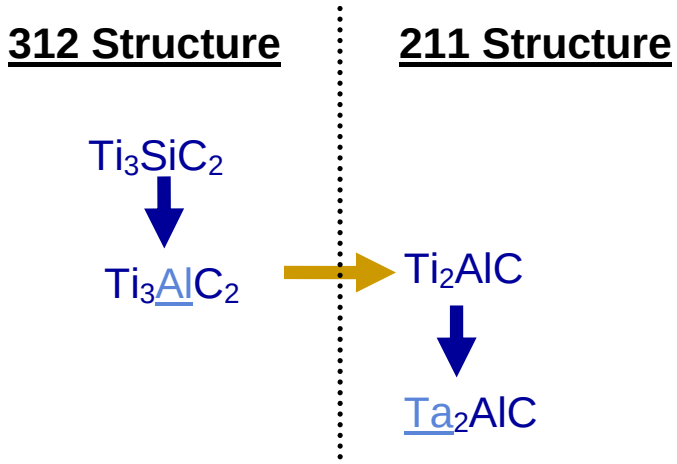

Ti_3SiC_2-CDC was compared to Ti_3AlC_2-CDC to determine the effect of the A-group element. Ti_2AlC-CDC was compared to Ta_2AlC-CDC to determine the effect of the transition element, and Ti_3AlC_2-CDC was compared to Ti_2AlC-CDC to determine the effect of stoichiometry, i.e. the value of *n*, on the resultant carbon porosity. Material parameters for the carbides used are listed in Table 3.1

Table 3.1 Material properties of carbides used to produce CDC.

Carbide	Structure	Unit Cell Width (Å)	Unit Cell Length (Å)	Carbide Density (g/cm^3)	Calculated CDC Density (g/cm^3)
Ti_3SiC_2	Hexagonal	3.06	17.67	4.52	0.55
Ti_3AlC_2	Hexagonal	3.07	18.57	4.50	0.52
Ti_2AlC	Hexagonal	3.04	13.60	4.11	0.36
$Ti_2AlC_{0.5}N_{0.5}$	Hexagonal	3.00	13.6	4.19	0.18
Ta_2AlC	Hexagonal	3.07	13.8	11.82	0.35
TaC	Rock salt	3.01	3.01	13.9	0.86
Ta_2C	Hexagonal	3.01	3.01	15.0	0.48

CDC density was calculated by the following equation:

$$\rho_{CDC} = \frac{n(M_c)}{M_{MC}} \rho_{MC} \quad (3.1)$$

ρ_{CDC} is the carbide derived carbon density, n is the number of moles of carbon within one mole of carbide, M_c is the molecular weight of carbon, M_{MC} is the molecular weight of carbide, and ρ_{MC}. ρ_{CDC} can also be considered the density of carbon within the initial carbide since the transformation from initial carbide to carbon is conformal.

3.1.2 Binary Carbides

Tantalum containing binary carbide powders, namely TaC and Ta_2C, were investigated to compare their porosity to Ta_2AlC-CDC, because it was found that some of the largest surface areas were obtained with the latter. Thin films of TiC deposited by magnetron sputtering were used for the formation of a carbon membrane.

3.1.3 Carbo-Nitride

To evaluate a CDC with extremely high theoretical porosity, a carbo-nitride, in particular, $Ti_2AlC_{0.5}N_{0.5}$ was investigated.

The general chlorination reactions for carbides (R3.1), nitrides (R3.2), and carbo-nitrides (R3.3) are listed below:

$$M^a_xM^b_yC_z + (a + b)/2\ Cl_{2(g)} \rightarrow z\ C(s) + x\ M^aCl_a + y\ M^bCl_b \quad (R3.1)$$

$$M^a_xM^b_yN_z + (a + b + 3)/2\ Cl_{2(g)} \rightarrow x\ M^aCl_a + y\ M^bCl_b + z\ NCl_3 \quad (R3.2)$$

$$M^a_xM^b_yC_zN_w + (a + b + 3)/2\ Cl_{2(g)} \rightarrow z\ C(s) + x\ M^aCl_a + y\ M^bCl_b + z\ NCl_3 \quad (R3.3)$$

The chlorination of carbides produces metal chlorides and porous carbon, while the chlorination of metal nitrides produces metal chlorides and nitrogen chloride with no porous carbon. The reaction between $Cl_{2(g)}$ and a carbo-nitride produces both porous carbon and nitrogen (III) chloride, in addition to the metal chlorides that form.

3.2 Carbide Derived Carbon Synthesis

Chlorination was preformed on powder, bulk, and thin film carbides and carbo-nitrides. Reactive and purging gases used during chlorination experiments were high purity Cl_2 (Air Gas, 99.5%) and high purity Ar (Air Gas, 99.998%), respectively. The carbide material was loaded into a horizontal quartz tube furnace (Fig. 3.33.). The tube was purged with Ar for 30 minutes, followed by heating to the desired temperature at the rate of 30°C/min. A bubbler containing sulfuric acid was attached to the exhaust tubing to prevent back-flow of air into the system. Once the desired temperature was achieved, which was within the range of 400-1200 °C, the Ar flow was stopped and the Cl_2 flow was started at a rate of 10 sccm. After the desired period of time at elevated temperature, ranging from 5 minutes to 6 hours, the sample was cooled under an Ar environment to remove residual metal chlorides.

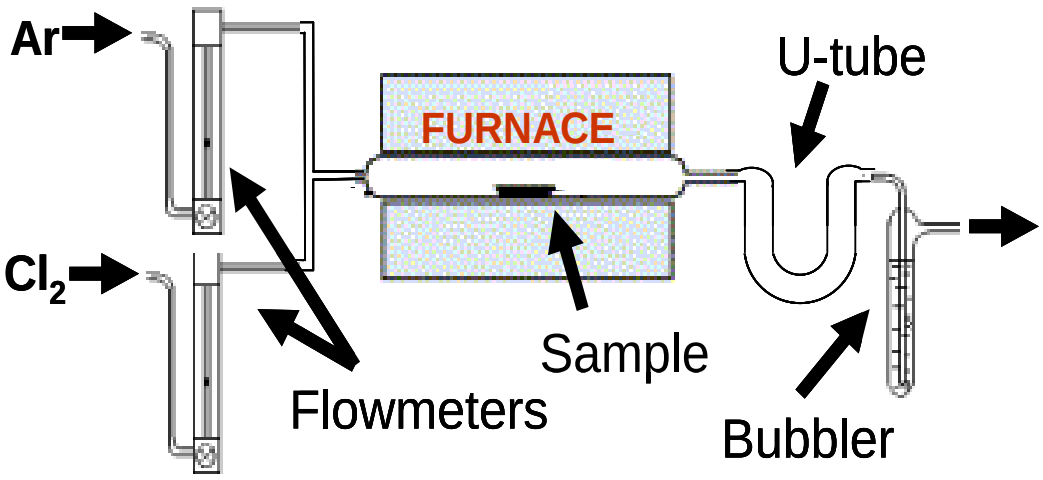

Figure 3.3 Experimental setup for chlorination of metal carbides.

Hydrogen annealing was performed on some samples to remove residual chlorine by the reaction:

$$H_2 + Cl_2 \rightarrow 2HCl \quad \text{(R3.4)}$$

When H_2 annealing was included, once chlorination was finished, Ar was used to flush the atmosphere while the furnace was heated or cooled to the H_2 annealing temperature. If the chlorination and H_2 annealing temperature were the same, Ar was still purged to remove residual Cl_2 gas to prevent the formation of HCl in the system. Subsequently, the H_2 was passed for a desired amount of time, followed by cooling in an Ar environment.

3.3 Thermodynamic Calculations

FactSage v 5.4, thermodynamic Gibbs energy minimization software, was used to calculate the amount of reaction species formed in equilibrium during the chlorination process at 1 atm total pressure with varying temperatures and mole ratios of metal carbide to chlorine. The software assumes the reactions occur in a closed system.

3.4 Characterization

The structure of CDC was characterized after chlorination at the various temperatures using the following characterization techniques:

3.4.1 X-ray Diffraction

Powder samples were mounted on frosted glass slides using ethanol as a solvent to adhere the powder. Spectra were measured using a Rigaku diffractometer operated at 30 mA and 45 kV with CuK_α radiation ($\lambda = 0.154$ nm). A 2Θ step size of 0.05 ° with a 2 s hold time was used during data collection.

3.4.2 Raman Spectroscopy

A Renishaw 1000 micro-Raman spectrometer with an Ar-ion laser (514.5 nm) and an objective of 500X was used to collect Raman spectra. D- and G-bands, located at 1360 and 1590 cm^{-1} [69], respectively, were fit by Gaussian model and full-width-at-half-maximum (FWHM) measured using GRAMS/32 spectroscopic software.

3.4.3 Electron Microscopy

3.4.3.1 Transmission Electron Microscopy

A JEOL 2010F microscope with accelerating voltage of 200 kV was used to image powder samples placed on a copper grid coated with lacey carbon for increased adherence. Powder samples were applied to the lacey carbon by swabbing the grid in an ultrasonicated mixture of carbon powder and ethanol. Experiments were performed at the regional materials characterization facility, LRSM, at the University of Pennsylvania.

3.4.3.2 Scanning Electron Microscopy

A Philips XL-30 environmental field-emission FESEM with an accelerating voltage of 20 kV was used to image samples. Platinum sputter coatings or variable pressure mode was required for membrane samples supported on alumina discs to increase their conductivity and overcome charging effects. To verify the chemical composition of the CDC, SEM analysis was always accompanied by energy dispersive spectroscopy (EDS) with an accelerating voltage of 20 kV, spot size of 4, and a working distance of 12.5 mm.

3.4.4 Gas Sorption Analysis

Gas sorption analysis was used to characterize the porosity of the CDC materials. Isotherms were measured up to 760 mm Hg at various temperatures ranging from 77K to 25 °C. Measurements were performed on Autosorb-1 using Autosorb 1 version 1.5

software for analysis and Quadrasorb using QuadraWin version 1.1 software for analysis, both by Quantachrome Instruments.

Both instruments measure an excess isotherm by measuring the volume of gas adsorbed and subsequently desorbed from the surface of the adsorbent at an equilibrium vapor pressure at a constant temperature, below the critical temperature of the adsorbate [70]. The excess isotherm can be plotted by the volume of adsorbate absorbed and desorbed versus relative pressure. Various isotherms exist based on the classification system by Brunauer, Deming, Deming and Teller (BDDT system) [71] (Fig. 3.4).

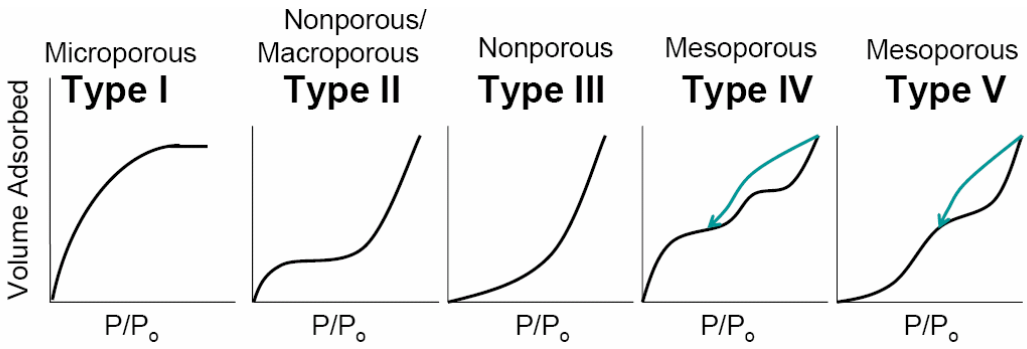

Figure 3.4 Isotherm types according to the BDDT classification system.

To prepare samples for analysis, samples are outgassed for at least 16 h in an independent outgasser, FlowValve by Quantachrome Instruments, capable of reaching 100 torr. The outgassing process removes surface contaminants, purifying the surface. Samples are carefully weighed just after outgassing due to the removal of heavy vapors and hydrocarbons.

The primary adsorbates used were Ar and N_2 at 77K for the analysis of micro and mesoporosity, respectively. Argon is used as an adsorbate for microporosity because it easily fills the smallest pores [72]. Since Ar is a monoatomic gas with a nonpolar,

spherical molecule it interacts very slightly, with the carbon surface. Nitrogen being a nonspherical, diatomic molecule interacts more strongly with carbon since it has a quadruple moment. Since it also does not glide along the carbon surface as easily as Ar, it cannot fill the smallest pore like Ar and therefore is better used to evaluate the mesoporosity of carbon. Additional adsorbates such as CO_2, H_2, CH_4, and SF_6 were also used to determine the gas separation ability of CDC. Properties for the adsorbate gases are given in Table 3.2.

Table 3.2 Adsorbate gas properties.

Gas	Manufacturer	Purity (%)	Kinetic Diameter (nm)	Condensation Temperature (°C)
Ar	Air Gas	99.998	0.34	-150
N_2	Air Gas	99.99	0.36	-160
CO_2	Air Gas	99.9	0.33	-43
CH_4	Air Gas	99.9	0.38	-126
O_2	Air Gas	99.9	0.36	-147
H_2	Air Gas	99.99	0.28	-217
SF_6	Wesco	99.9	0.513 [73]	-28

3.4.4.1 Pore Size Distribution

Pore size distributions were evaluated using Non-Local Density Functional Theory (NLDFT) method [74]. Density functional theory methods provide an accurate estimate for pore size analysis with materials containing significant microporosity. The pore size distribution for adsorbents is determined through a generalized adsorption isotherm equation:

$$N(P/P_o) = \int_{W_{\min}}^{W_{\max}} N(P/P_o, W) \times f(W) \times dW \ldots \quad (3.2)$$

where $N(P/P_o)$ is the experimental adsorption isotherm of adsorbed volume versus relative pressure. W is the pore width, $N(P/P_o,W)$ is the isotherm on a single pore of width W, and f(W) is the pore size distribution function. The adsorption isotherms in model pores are determined based on intermolecular potentials of the fluid-fluid and solid-fluid interactions and compared to the experimental results.

Based on a slit-pore model, which is a reasonable assumption due to the layered structure of the MAX phases, the recommended pore width ranges for the various adsorbates are the following:

Table 3.3 Common adsorbates and the recommended pore range at analysis temperature.

Adsorbate	Analysis Temperature	Pore Range
Ar	77 K	0.35-8 nm
N_2	77 K	0.35-35 nm

Although both Ar and N_2 are capable of measuring pores as small as 0.35 nm, Ar is able to measure a larger amount of smaller pores compared to N_2 since N_2 extends over a broader pore size range. Therefore, it is necessary to use both adsorbates to thoroughly investigate the porosity of a material containing both micro and mesoporosity.

3.4.4.2 Pore Volume

Assuming the transformation from carbide to carbon is conformal, the theoretical pore volumes per gram of CDC were calculated using the following equation:

$$v_{pore} = \frac{1}{\rho_{CDC}} - \frac{1}{\rho_C} \tag{3.3}$$

ρ_C is the density of graphitic carbon, 2.24g/cm^3. Calculated pore volumes per gram of CDC are given in Table 3.4.

Table 3.4 Theoretical pore volumes.

Carbide	Theoretical Pore Volume (cm^3/g)
Ti_3SiC_2	1.37
Ti_3AlC_2	1.47
Ti_2AlC	2.33
$Ti_2AlC_{0.5}N_{0.5}$	5.11
Ta_2AlC	2.41
TaC	0.71
Ta_2C	1.63

Experimental pore volumes were determined based on the NLDFT method.

3.4.4.3 Specific Surface Area Calculations

Specific surface area, SSA, calculations were performed using both the NLDFT and multi-point Brunauer-Emmett-Teller (BET) methods [75].

The BET method is the most widely used procedure for the determination of surface area in solid porous materials. The BET equation is the following:

$$\frac{1}{W((\frac{P_o}{P})-1)} = \frac{1}{W_m C} + \frac{C-1}{W_m C}\left(\frac{P}{P_o}\right) \tag{3.4}$$

where W is the adsorbed gas weight at relative pressure, P/P_o, W_m is the weight of the gas adsorbed equaling one monolayer covering the surface, C is the BET constant related to the energy of adsorption of the first monolayer. The value of C relates to the degree of interaction between the adsorbent and adsorbate.

Multipoint BET requires a linear plot of $1/(W(P/P_o)-1$ versus P/P_o. Usually values are utilized in the range of P/P_o for which a linear relationship exists; that range is usually

between 0.05-0.35. When the molecular cross-section of the adsorbate is known, the surface area of the material can be determined from the slope of the curve using the equation:

$$S = \frac{W_m N A_{cs}}{M} \tag{3.5}$$

where N is Avogadro's number, A_{cs} is the molecular cross-sectional area of the adsorbate molecule, M is the molecular weight of the adsorbate, and S is the surface area of the adsorbent.

The BET specific surface area was calculated for comparison to other sorbent materials. The specific surface areas calculated from this method often over estimate the surface area for materials containing large amounts of mesopores. Specific surface areas were also calculated from the generalized adsorption isotherm, Equation 3.2, which is the basis of the NLDFT method. Specific surface areas calculated by this method are considered the DFT surface area of the material.

3.4.4.4 Heat of Adsorption Calculations

Heat of adsorption values were calculated using two isotherms measured at different temperatures for the same material. The adsorption isotherm data was interpolated so that both curves had pressures at corresponding volumes. Applying the Clausius-Clapeyron equation:

$$Q = \frac{R \ln\left(\frac{P_{T1}}{P_{T2}}\right)}{\frac{1}{T_2} - \frac{1}{T_1}} \tag{3.6}$$

Q is the isosteric heat of adsorption, P_{T1} is the pressure from the isotherm taken at temperature, T_1, P_{T2} is the pressure from the isotherm taken at temperature, T_2, and R is the gas law constant.

3.5 Membrane Synthesis

A thin film carbon membrane supported by a porous ceramic was synthesized using a magnetron sputtering technique [76], see Figure 3.5. The magnetron sputtering unit was designed at the University of Lodz, using four magnetrons produced by Dora Power Systems (Wilczyce, Poland).

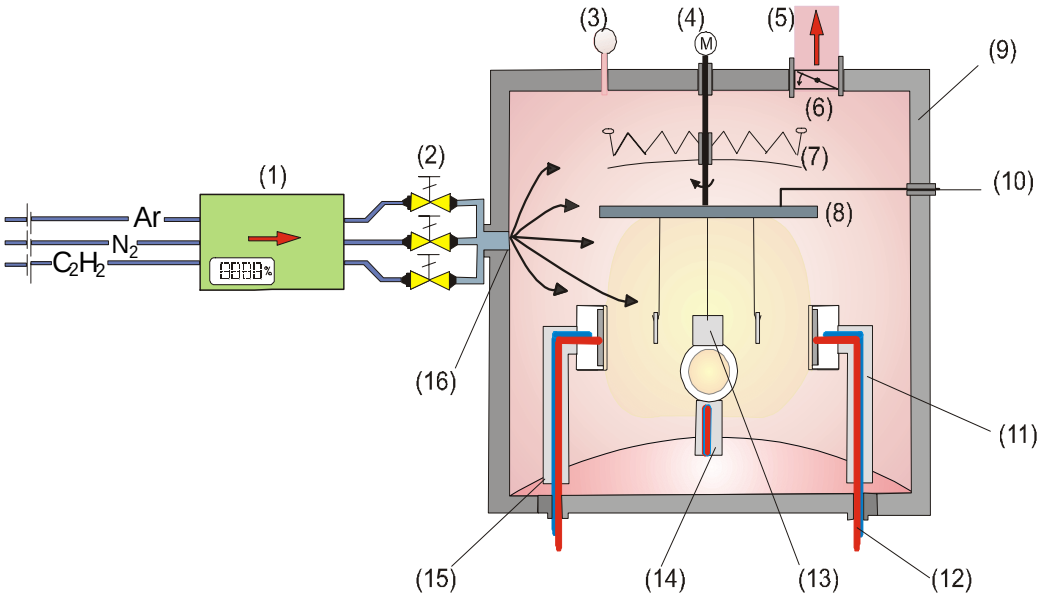

Figure 3.5 Magnetron sputtering setup. Scheme of coatings' deposition equipment: 1– mass flow controller; 2 stop valves; 3– vacuum meter; 4 – motor drive; 5 – connection to vacuum stand; 6 – throttle valve; 7 – IR radiator; 8 – rotary table; 9 – high vacuum chamber; 10 – table bias (negative); 11 – magnetron cooling; 12 – magnetron power feed; 13 – specimen mounted on the table; 14, 15 – four magnetrons with 100 mm diameter 10 mm thick high purity polycrystalline Ti disks; 16 – inert and reactive gas inlet. (Courtesy of Dr Bogdan Wendler)

Two types of porous ceramics were used as membrane supports, see Table 3.5. The support membranes were attached with the use of a thin and tough steel wire under a rotary table. The vacuum chamber is pumped down very slowly using a mechanical rotary pump and a special throttle valve up to the residual pressure 10^{-2} mbar. The diffusion pump is switched on and the chamber is evacuated to a residual pressure 10^{-4} Pa. The motor drive of the rotary table is switched on and the value of the angular speed 0.3 rad/s of the table with suspended specimens fixed. Argon is introduced into the vacuum chamber and the value 0.18 sccm Ar flow is fixed at the pressure $2x10^{-3}$ mbar in the vacuum chamber. The magnetron discharge is then turned on, with the power set to 3.0 kW of for all four magnetrons. Once sputtering is complete, the acetylene is introduced into the chamber until the total pressure in the chamber begins to increase as well.

Table 3.5 Support membrane properties.

Membrane	Manufacturer	Material	Pore Size	Thickness	Diameter
MF 5000	Sterlitech	Alumnina/Titania	50 nm	2 mm	35 mm
Anodisc 25	Whatman	Alumina	50nm/ 200 nm	60 μm	21 mm

Table 3.6 Magnetron sputtering parameters for TiC deposition.

Membrane Type	Power (kW)	Ar Flow (sccm)	C_2H_2 Flow (sccm)	Total Time (minutes)	Total Pressure (mbar)
MF 5000	4 x 3.0	0.16	0.4	12	2.2×10^{-3}
Anodisc 25	4 x 3.0	0.18	0.4	14	2.1×10^{-3}

The total power, total pressure, total time, argon flow, and acetylene flow are given in Table 3.6.

Once sputtering is complete, the magnetron discharge in all the magnetrons is switched off, the flow of Ar and C_2H_2 has been reduced to zero, the pumping system which had been uncoupled and the vacuum chamber is slowly vented. Magnetron sputtering was performed at the Lodz University of Technology in Poland by researchers in the laboratory of Dr Bogdan Wendler.

3.6 Gas Permeation

To determine if molecules could pass through a thin layer of CDC, a gas permeation setup was constructed. Ar, N_2, CH_4, CO_2, and H_2 were passed through the thin-film CDC while monitoring the pressure and flowrate (see Figure 3.6). A pressure gauge was placed after the first electronic flowmeter to provide an accurate pressure measurement. A robust Sterlitech-based membrane was attached to glass fittings by a silicone adhesive and submerged in a water bath to test for leaks within the silicone seal. The outlet gas passed through another electronic flowmeter connected to a mass flow controller. Tubing from the outlet mass flow controller was then placed in the water bath to monitor the outlet bubble rate. Pressures up to 0.17 MPa were applied to the membrane, followed by a shut off of the gas flow. The pressure was monitored as it dropped over time toward zero.

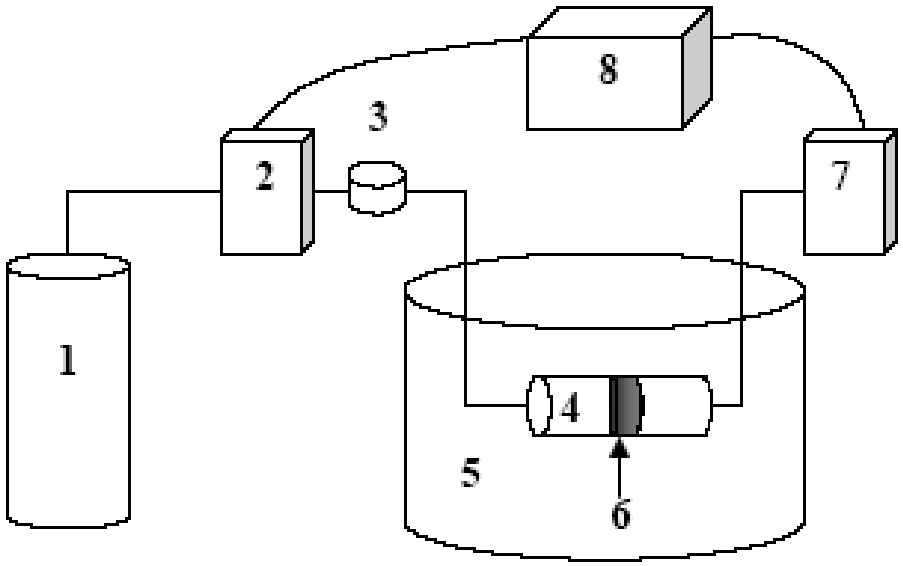

Figure 3.6 Experimental setup for gas permeation. 1) gas cylinder, 2) flowmeter model Tylan FC-280, 3) pressure gauge up to 0.14 MPa, 4) glass fitting, 5) water bath, 6) membrane, 7) flowmeter model Tylan FM 380, 8) mass flow controller Tylan RO-28.

3.7 Protein Adsorption

Enzyme-Linked Immunosorbent Assay (ELISA) tests were used to test the capacity for Ti_3AlC_2-CDC and Ti_2AlC-CDC powders to adsorb proteins tumor necrosis factor (TNF)-α , interleukin (IL)-8, IL-6, and IL-1β from blood plasma [77]. Fresh frozen human plasma (NBS, UK) was defrosted and spiked with the recombinant human cytokines (TNF-α, IL-1β, IL-6, and IL-8; all obtained from BD Biosciences, US) at a concentration of about 1000, 500, 5000, and 500 pg/ml, respectively. These levels are comparable with the concentrations measured in the plasma of patients with sepsis. Carbon adsorbents (0.02 g) were equilibrated in phosphate buffered saline (PBS) (0.5 ml) overnight prior to removal of PBS and addition of 800 µl of spiked human plasma. Controls consisted of spiked plasma with no adsorbent present. Adsorbents were

incubated at 37 °C while shaking (90 rpm). At 5, 30 and 60 min time points, samples were centrifuged (125g) and the supernatant collected and stored at -20 °C prior to ELISA (BD Biosciences) analysis for the presence of cytokines. Samples were diluted 1:4 (TNF-α, IL-8, IL-1β) and 1:10 (IL-6) in assay diluent prior to analysis. ELISA tests were performed at the University of Brighton in the United Kingdom by researchers in the laboratory of Dr. Sergey Mikhalovsky.

4 Discussion and Results

4.1 Factsage Thermodynamic Software

4.1.1 Chlorination of Metal Carbides

The thermodynamic calculations provide information about a closed system in equilibrium. The experimental chlorination setup is an open system, where gaseous reaction products are continuously removed with a gas flow, and the actual product composition may be determined by the kinetics of the process. However, the results obtained provide general guidelines and are an aid for experimental design. For example, they predict that selective removal of metal atoms is possible by using small amounts of Cl_2, as well as suggest that in general a moderate amount of Cl_2 is one key to efficient CDC synthesis. Excess Cl_2 in the experimental procedure favors the formation of carbon, although it may slightly reduce the yield.

4.1.1.1 Ti_3SiC_2 Derived Carbon

The reaction between Ti_3SiC_2 and chlorine at a constant temperature of 800 °C and various mole ratios are given in Figure 4.1a. At 800 °C, the reaction between Ti_3SiC_2 and Cl_2 illustrates that for maximum carbon formation to occur, a mole ratio of Ti_3SiC_2 to carbon must be in excess of 8:1. From the simulations and based on constant mole ratios, it is found that the temperature when the reaction of chlorine with Ti_3SiC_2 occurs (Fig. 4.1b) also determines the amount of carbon that forms. At lower temperatures, the carbon yield is relatively low for small amounts of chlorine, and at higher temperatures, SiC, and TiC, are expected to remain in the system. Limited chlorine may also result in the formation of solid $TiCl_3$, which can be removed only if the processing temperature exceeds ~550°C. Excess Cl_2 lends toward the formation of $TiCl_4$,

which forms either a liquid at low temperatures, or a gas at higher temperatures. Formation of gaseous $SiCl_4$ is expected at all reaction temperatures (Fig. 4.1). A significant amount of carbon is used in the production of CCl_4 at temperatures below ~ 600°C. At higher temperatures, $SiCl_4$ and $TiCl_4$ are more stable as compared to CCl_4, therefore providing an increased carbon yield at higher chlorination temperatures.

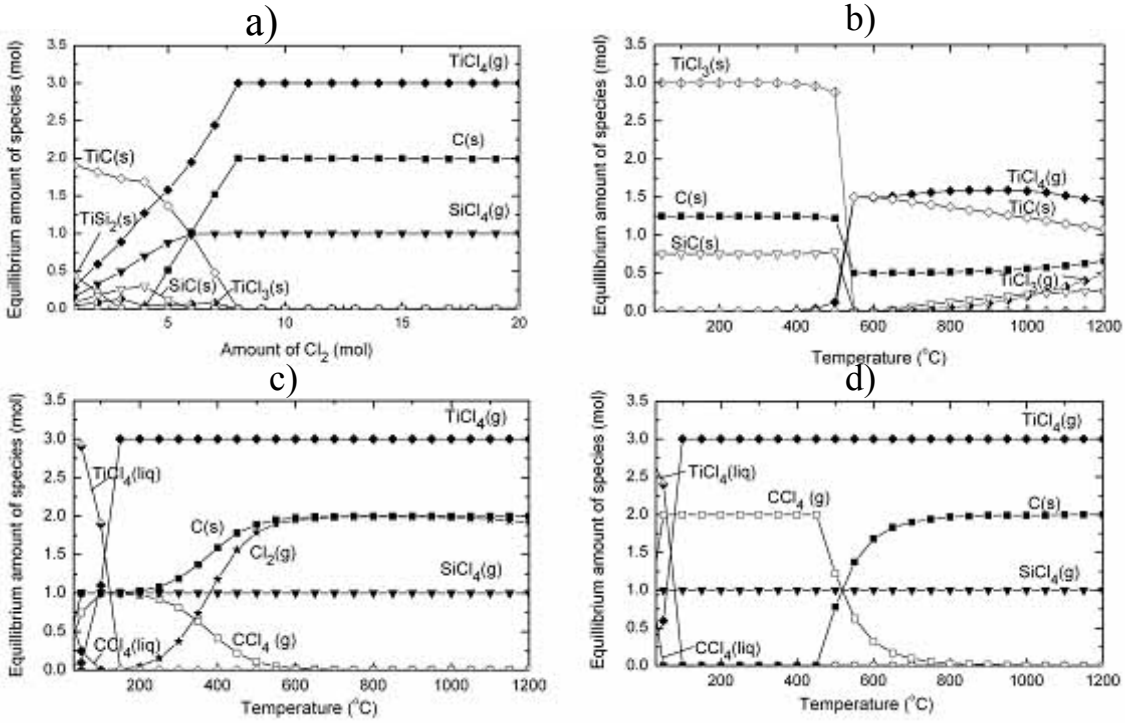

Figure 4.1: Ti_3SiC_2-Cl_2 system thermodynamic simulations at a constant temperature of, a) 800 °C, and constant mole ratios of, b) 5:1, c) 10:1, and, d) 20:1.

Based on the simulation performed with a constant mole ratio of 5:1 (Fig. 4.1b), the following reactions can occur depending on the temperature, T, of the chlorination:

$T < 500$ °C, $\quad Ti_3SiC_2 + 5\ Cl_2 \rightarrow 3\ TiCl_{3(s)} + 1.25\ C_{(s)} + 0.75\ SiC_{(s)} + 0.25\ SiCl_{4(g)}$ (R4.1)

$T > 550$ °C, $\quad Ti_3SiC_2 + 5\ Cl_2 \rightarrow (1.5 + x)\ TiCl_{4\,(g)} + 1.5\ TiC_{(s)} + C_{(s)} + TiCl_{3(s)} + SiC_{(s)}$ (R4.2)

Based on the simulation performed with a constant mole ratio of 10:1 (Fig. 4.1c), the following reactions can occur depending on T of the chlorination:

Note, *(0<x<1)*applies for all reactions listed.

T< 180 °C:

$Ti_3SiC_2 + 10\ Cl_2 \rightarrow (3-x)\ TiCl_{4(liq)} + x TiCl_{4(g)} + (0.5-1/6x) CCl_{4(liq)} + (0.5+1/6x) CCl_{4(g)} + SiCl_{4(g)}$ (R4.3)

T=180-600 °C:

$Ti_3SiC_2 + 10\ Cl_2 \rightarrow 3\ TiCl_{4(g)} + SiCl_{4(g)} + (1+x)\ C_{(s)} + (1-x)\ CCl_{4(g)} + 2x\ Cl_{2(g)}$ (R4.4)

T >600 °C:

$Ti_3SiC_2 + 10\ Cl_2 \rightarrow 3\ TiCl_{4(g)} + SiCl_{4(g)} + C_{(s)} + 2\ Cl_{2(g)}$ (R4.5)

Based on the simulation performed with a constant mole ratio of 20:1 (Fig. 4.1d), the following reactions can occur depending on T of the chlorination:

T < 50 °C:

$Ti_3SiC_2 + 20\ Cl_2 \rightarrow (1.5+x)\ CCl_{4(g)} + (2.75-x)\ CCl_{4(liq)} + SiCl_{4(g)} + 2\ CCl_{4(g)} + 13\ Cl_{2(g)}$ (R4.6)

T = 50-100 °C:

$Ti_3SiC_2 + 20\ Cl_2 \rightarrow (0.5+x)\ TiCl_{4(g)} + (0.5-x)\ TiCl_{4(liq)} + SiCl_{4(g)} + (0.5+2x)\ CCl_{4(g)} + (0.5+2x)\ CCl_{4(liq)} + 13\ Cl_{2(g)}$ (R4.7)

T =100-450 °C:

$Ti_3SiC_2 + 20\ Cl_2 \rightarrow 3\ TiCl_{4(g)} + SiCl_{4(g)} + C_{(s)} + 12\ Cl_{2(g)}$ (R4.8)

T=450-800:

$Ti_3SiC_2 + 20\ Cl_2 \rightarrow 3\ TiCl_{4(g)} + SiCl_{4(g)} + xC_{(s)} + (2-x)\ CCl_{4(g)} + (2x+8)\ Cl_{2(g)}$ (R4.9)

T > 800 °C:

$Ti_3SiC_2 + 20\ Cl_2 \rightarrow 3\ TiCl_{4(g)} + SiCl_{4(g)} + 2C_{(s)} + 12\ Cl_{2(g)}$ (R4.10)

From the simulation results, it is clear that an excess amount of Cl_2 is required to produce C without contamination of other solids such as $TiC_{(s)}$ and $SiC_{(s)}$, even at temperatures as high as 1200 °C as reaction 4.2 illustrates. Enough Cl_2 must be present for complete removal of Ti and Si atoms, otherwise their respective carbides will form. When an increased amount of Cl_2 is present, $TiCl_{4(g)}$ and $SiCl_{4(g)}$ are formed, separating the Ti and Si atoms from the carbon. The temperature at which the maximum carbon formation starts depends on the ratio of Cl_2 to metal carbide. At the moderate ratio of 10:1, maximum carbon yield starts around 600 °C (Fig. 4.1c). At a higher ratio of 20:1, the maximum carbon yield starts around 800 °C (Fig. 4.1d). When more chlorine is present, larger amounts of $CCl_{4(g)}$ form. The maximum carbon yield starts when $CCl_{4(g)}$ is no longer stable. Therefore, since $CCl_{4(g)}$ requires higher temperatures to be depleted in the 20:1 ratio simulation, the result is that the maximum yield of carbon starts at a higher temperature.

As seen in Reaction 4.4, significant amounts of carbon can be produced at temperatures as low as 180 °C with moderate Cl_2:carbide ratios. At the higher Cl_2:carbide ratios of 20:1, however, carbon formation is not possible at temperatures below 400 °C as seen in Reaction 4.8. This is because the carbon available in the system reacts with the excess $Cl_{2(g)}$ to form $CCl_{4(g)}$. (Fig. 4.1d)

Overall, the simulations suggests that an excess of Cl_2 is required for carbon synthesis, and that a Cl_2:carbide ratio of around 10:1 is optimal for maximum carbon yield. Carbon, however, can be produced in a broad temperature range, depending on the

Cl_2:carbide ratio, generally greater than 600 °C. With the proper Cl_2:carbide ratios, carbon formation is possible at temperatures as low as 180 °C.

4.1.1.2 Ti_3AlC_2 Derived Carbon

Ti_3AlC_2 has the same structure as Ti_3SiC_2, except that Al is substituted for Si, the A-group element site in a MAX-phase carbide. The reaction between Ti_3AlC_2 and Cl_2 produces $C_{(s)}$, $TiCl_4$, $AlCl_3$, CCl_4, and Al_2Cl_6. Similar to Ti_3SiC_2, the maximum yield of carbon is two moles for every one mole of carbide converted during the chlorination process, see Figure 4.2.

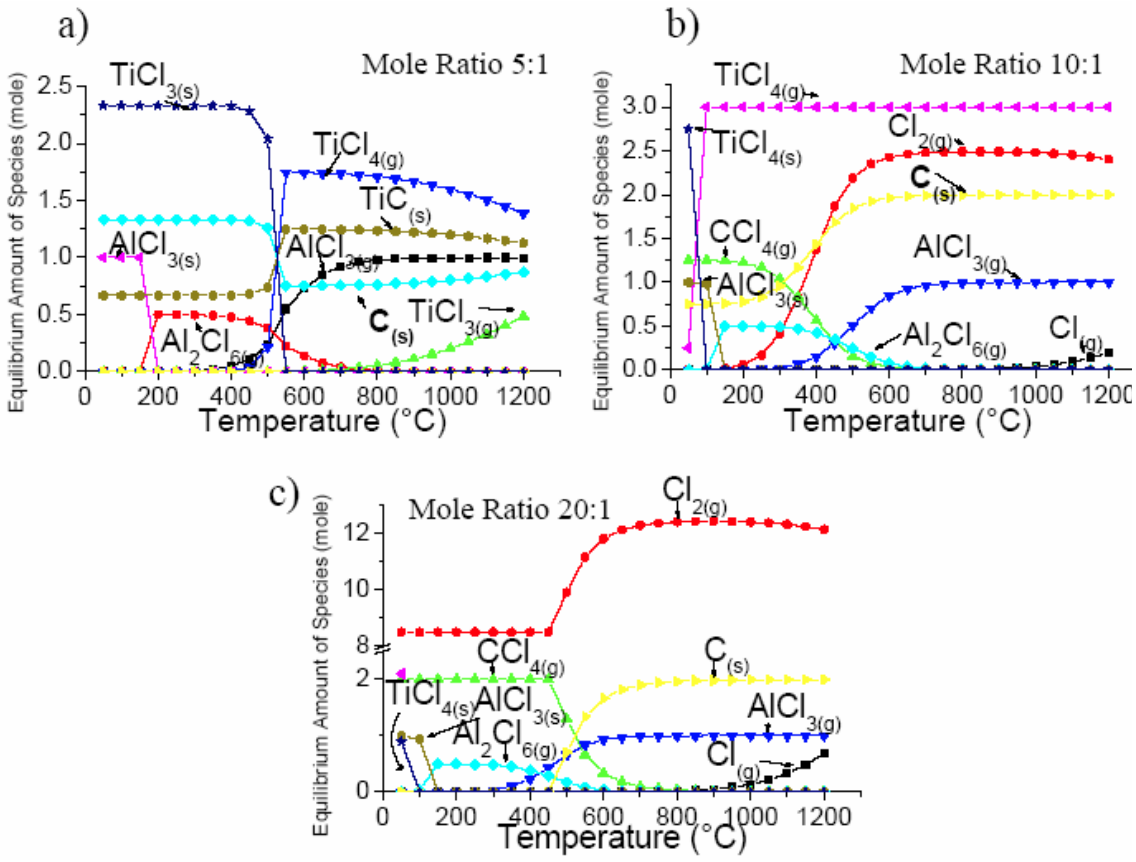

Figure 4.2: Ti_3AlC_2-Cl_2 system thermodynamic simulations at constant mole ratios of, a) 5:1, b) 10:1, and c) 20:1.

Based on the simulation performed with a constant mole ratio of 5:1 (Fig. 4.2a), the following reactions can occur depending on the temperature, T, of the chlorination:

T < 150 °C, $Ti_3AlC_2 + 5\ Cl_2 \rightarrow 2\ 1/3\ TiCl_{3(s)} + 1\ 1/3\ C_{(s)} + AlCl_{3(g)} + 2/3\ TiC_{(s)}$ (R4.11)

T 150-350 °C, $Ti_3AlC_2 + 5\ Cl_2 \rightarrow 2\ 1/3\ TiCl_{3(s)} + 1\ 1/3\ C_{(s)} + 0.5\ Al_2Cl_{6(g)} + 2/3\ TiC_{(s)}$ (R4.12)

T, 350-550 °C, $Ti_3AlC_2 + 5\ Cl_2 \rightarrow (2\ 1/3 - 2\ 1/3\ x)\ TiCl_{3(s)} + 3/4\ C_{(s)} + (\frac{1}{2} - \frac{1}{4}\ x)Al_2Cl_{6(g)} + (2/3 + (1\ \frac{1}{4} - 2/3)x)\ TiC_{(s)} + (0.5x)AlCl_{3(g)} + 1\ \frac{3}{4}\ x\ TiCl_{4(g)}$ (R4.13)

T, 550 - 750 °C,

$Ti_3AlC_2 + 5\ Cl_2 \rightarrow 1\ \frac{3}{4}\ TiCl_{4(g)} + \frac{3}{4}\ C_{(s)} + (\frac{1}{2} + \frac{1}{2}\ x)\ AlCl_{3(g)} + TiCl_{4(g)} + 1\ \frac{1}{4}\ TiC_{(s)} + (\frac{1}{4} - \frac{1}{4}\ x)Al_2Cl_{6(g)}$ (R4.14)

T > 750 °C,

$Ti_3AlC_2 + 5\ Cl_2 \rightarrow (1\ \frac{3}{4} - 0.37x)\ TiCl_{4(g)} + (\frac{3}{4} + 0.12x)\ C_{(s)} + AlCl_{3(g)} + (0.48x)\ TiCl_{3(g)} + (1\ \frac{1}{4} - 0.12x)\ TiC_{(s)} + (\frac{1}{4} - \frac{1}{4}\ x)Al_2Cl_{6(g)}$ (R4.15)

Based on the simulation performed with a constant mole ratio of 10:1 (Fig. 4.2b), the following reactions can occur depending on the temperature, T, of the chlorination:

T < 100 °C, $Ti_3AlC_2 + 10\ Cl_2 \rightarrow (2.75\text{-}2.5x)\ TiCl_{4(s)} + 0.75\ C_{(s)} + AlCl_{3(s)} + (0.25+2.5x)\ TiCl_{4(g)} + 1.25\ CCl_{4(g)}$ (R4.16)

T, 100 - 600 °C

$$Ti_3AlC_2 + 10\ Cl_2 \rightarrow 3\ TiCl_{4(g)} + (0.75 + 1.25x)\ C_{(s)} + 2.5x\ Cl_{2(g)} + x\ AlCl_{3(g)} + (0.5 - 0.5x)\ Al_2Cl_{6(g)} \quad \text{(R4.17)}$$

T > 600 °C, $Ti_3AlC_2 + 10\ Cl_2 \rightarrow 3\ TiCl_{4(g)} + (2.5\text{-}0.1x)\ Cl_{2(g)} + 2\ C_{(s)} + AlCl_{3(g)} + 0.2x\ Cl_{(g)}$ (R4.18)

Based on the simulation performed with a constant mole ratio of 20:1 (Fig. 4.2c), the following reactions can occur depending on the temperature, T, of the chlorination:

T < 100 °C, $Ti_3AlC_2 + 20\ Cl_2 \rightarrow 8.5\ Cl_{2(g)} + (1 - x)\ TiCl_{4(s)} + AlCl_{3(s)} + (2+x)\ TiCl_{4(g)} + 2\ CCl_{4(g)}$ (R4.19)

T, 100 - 200 °C

$$Ti_3AlC_2 + 20\ Cl_2 \rightarrow 8.5\ Cl_{2(g)} + 2\ CCl_{4(g)} + 3\ TiCl_{4(g)} + (1-x)\ AlCl_{3(g)} + (0.5x)Al_2Cl_{6(g)} \quad \text{(R4.20)}$$

T, 200 - 450 °C

$$Ti_3AlC_2 + 20\ Cl_2 \rightarrow 8.5\ Cl_{2(g)} + 2\ CCl_{4(g)} + 3\ TiCl_{4(g)} + (0.5x)\ AlCl_{3(g)} + (0.5\text{-}0.25x)\ Al_2Cl_{6(g)} \quad \text{(R4.21)}$$

T, 450 - 700 °C

$$Ti_3AlC_2 + 20\ Cl_2 \rightarrow (8.5+4x)\ Cl_{2(g)} + (2\text{-}2x)\ CCl_{4(g)} + 2x\ C_{(s)} + 3\ TiCl_{4(g)} + (0.5+0.5x)\ AlCl_{3(g)} + (0.5\text{-}0.25x)\ Al_2Cl_{6(g)} \quad \text{(R4.22)}$$

T, > 700 °C

$$Ti_3AlC_2 + 20\ Cl_2 \rightarrow (12.5\text{-}1/3\ x)\ Cl_{2(g)} + 2\ C_{(s)} + 3\ TiCl_{4(g)} + AlCl_{3(g)} + 2/3x\ Cl_{(g)} \quad \text{(R4.23)}$$

In the chlorine lean conditions of 5:1 mole ratio, the carbon yield is higher at low temperatures compared to at high temperatures due to the formation of solid TiC at temperatures above 600 °C. In addition to carbon, other solids form, such as $TiCl_3$ at temperatures below 600 °C, $AlCl_3$ at temperatures below 200 °C, and TiC at temperatures above 600 °C (Fig. 4.2a). Therefore, due to additional solids contamination, the mole ratio of 5:1 is unfavorable at any chlorination temperature.

At the higher levels of chlorine of 10:1 mole ratio, carbon reaches the maximum theoretical limit of 2 moles of carbon for 1 mole of carbide transformed without the formation of additional solid compounds. The maximum occurs around 600 °C due to the reduction of $CCl_{4(g)}$ formation, thereby releasing $C_{(s)}$ and forming $Cl_{2(g)}$ (Fig. 4.2b). Results obtained for mole ratio of 20:1 (Fig. 4.2c) are similar to results obtained for the 10:1 ratio.

4.1.1.3 Ti_2AlC Derived Carbon

Similar to Ti_3SiC_2-CDC, a maximum carbon yield occurs at the moderate molar ratio of chlorine to Ti_2AlC of 6:1 or higher during the synthesis of Ti_2AlC-CDC at 800 °C, see Figure 4.3. Therefore, maximum carbon formation occurs at slightly lower chlorine amounts for Ti_2AlC-CDC than for Ti_3SiC_2-CDC. At very high molar ratios > 15:1, the carbon formation drops slightly due to the formation of $CCl_{4(g)}$ (Fig. 4.3a).

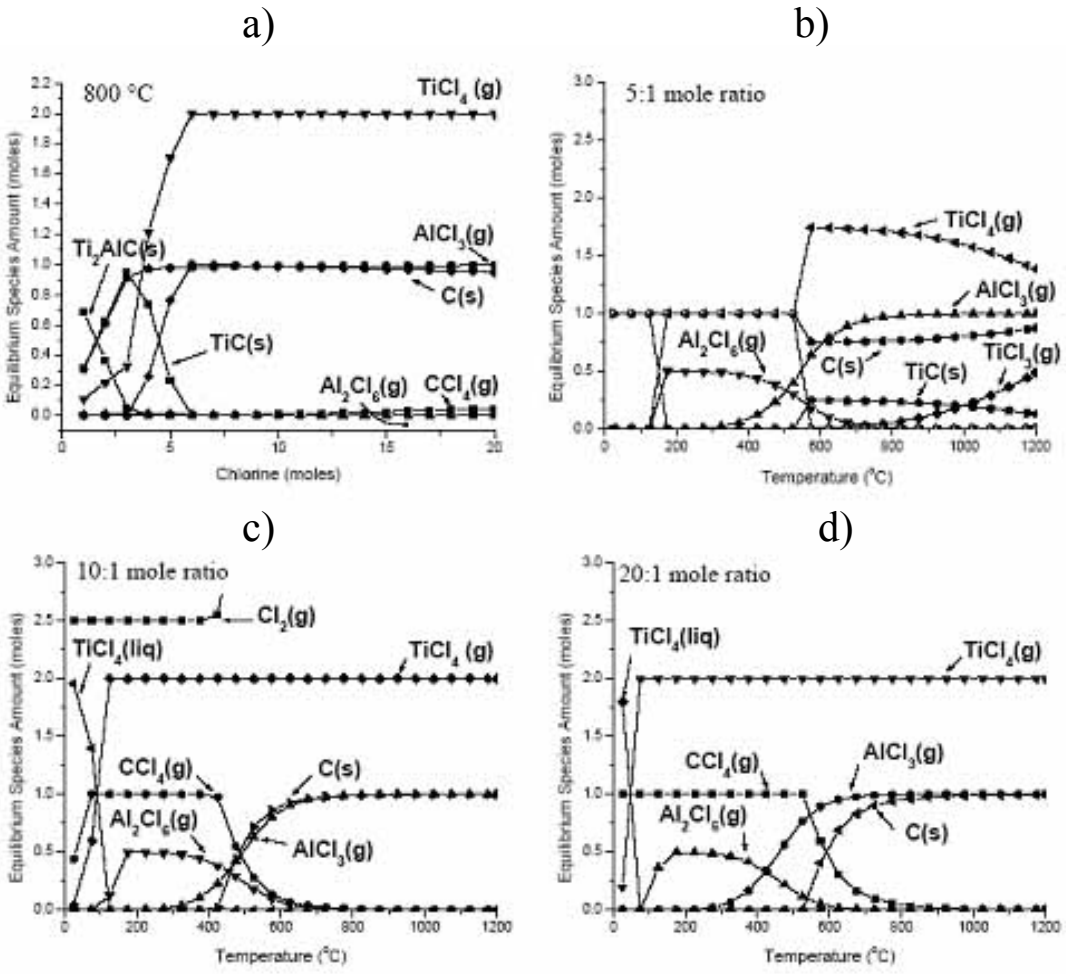

Figure 4.3: Ti_2AlC-Cl_2 system thermodynamic simulations at a constant temperature of, a) 800 °C, and constant mole ratios of, b) 5:1, c) 10:1, and, d) 20:1.

In the simulation with a constant molar ratio of 5:1, at temperatures greater than 550 °C, carbon formation drops due to an increase in $TiC_{(s)}$ formation (Fig. 4.3b). At higher mole ratios of 10:1, the carbon formation increases with decreasing CCl_4 as the temperature increases above 450 °C (Fig. 4.3c). At even higher mole ratios of 20:1, the carbon formation increases as CCl_4 decreases at temperatures about 550 °C (Fig. 4.3d). Therefore, extremely high volumes of Cl_2 can reduce the temperature window for maximum yield of carbon during a chlorination reaction.

A major difference between Ti_3AlC_2 and Ti_2AlC-CDC is that for Ti_3AlC_2, two moles of carbon are the maximum yield compared to one for Ti_2AlC-CDC for every mole of carbide reacted.

4.1.1.4 Ta_2AlC Derived Carbon

The reaction of Ta_2AlC with Cl_2 produces $C_{(s)}$, CCl_4, $TaCl_5$ Al_2Cl_6, and $AlCl_3$ for all more ratios from 5:1 to 20:1 Cl_2 to carbide, see Figure 4.4. The reaction is very similar to the reaction between Ti_2AlC and Cl_2, except that tantalum chlorides are produced instead of $TiCl_4$ (Fig. 4.4). $TaCl_5$ is the primary chloride that forms from the reaction, however, $TaCl_4$ can also form when the mole ratio of Cl_2:carbide is low.

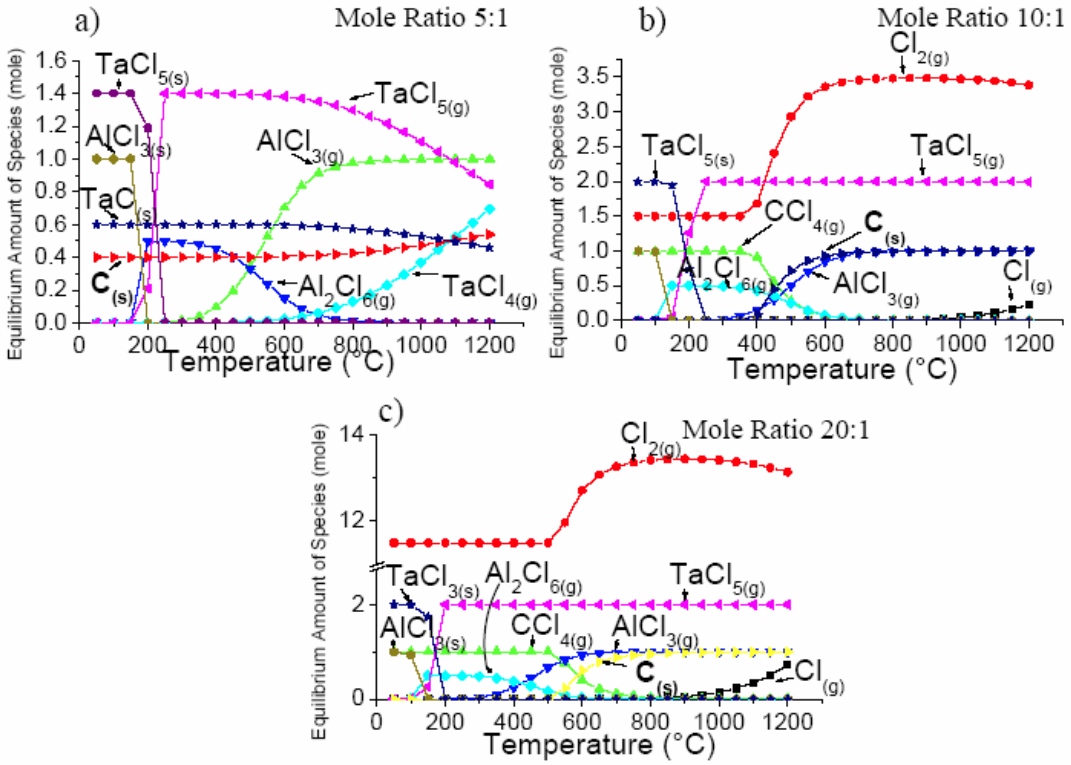

Figure 4.4: Ta_2AlC-Cl_2 system thermodynamic simulations at constant mole ratios of, a) 5:1, b) 10:1, and, c) 20:1.

4.1.2 Chlorination of Carbo-Nitride

$Ti_2AlC_{0.5}N_{0.5}$ follows a similar reaction as Ti_2AlC. In addition to the removal of Ti and Al, the nitrogen is removed by chlorine with the formation of nitrogen (III) chloride, NCl_3. With a boiling point of 73 °C, NCl_3 is easily removed during the chlorination process. With proper chlorine to carbide ratios and chlorination temperature, porous carbon is formed by the reaction:

$$Ti_2AlC_{0.5}N_{0.5} + 7\ Cl_{2(g)} \rightarrow \tfrac{1}{2}\ C_{(s)} + \tfrac{1}{2}\ NCl_{3(g)} + TiCl_{4(g)} + AlCl_{3(g)} \qquad \text{(R4.22)}$$

4.1.3 H_2 Annealing Simulations

During the H_2 annealing process, a significant amount of $HCl_{(g)}$ is predicted, see Figure 4.5. When the molecular composition includes $C_{(s)}$, $Cl_{2(g)}$, $TiCl_{4(g)}$, $H_{2(g)}$, $H_2O_{(g)}$ and $O_{2(g)}$, the amount of $HCl_{(g)}$ drops slightly at 100 °C due to the increased formation of $TiCl_{4(g)}$ and $CH_{4(g)}$, and then further drops around 800 °C due to the increase of $H_{2(g)}$ and $TiCl_{3(g)}$ formation. The carbon yield decreases around 800 °C also due to the increased formation of $CO_{(g)}$. Therefore, when maximum carbon yields are desired, H_2 annealing should be at temperatures of 800 °C or less. When the molecular composition does not include metal chlorides, the reaction products are shown in Figure 4.6. $HCl_{(g)}$ is still produced by the reaction between H_2 and $Cl_{2(g)}$. Two moles of $HCl_{(g)}$ are formed for every one mole of $H_{2(g)}$ and $Cl_{2(g)}$ reacted. When $O_{2(g)}$ is present, it will bond with C to form $CO_{2(g)}$. $O_{2(g)}$ and $H_2O_{(g)}$ were included in the simulation as adsorbed species.

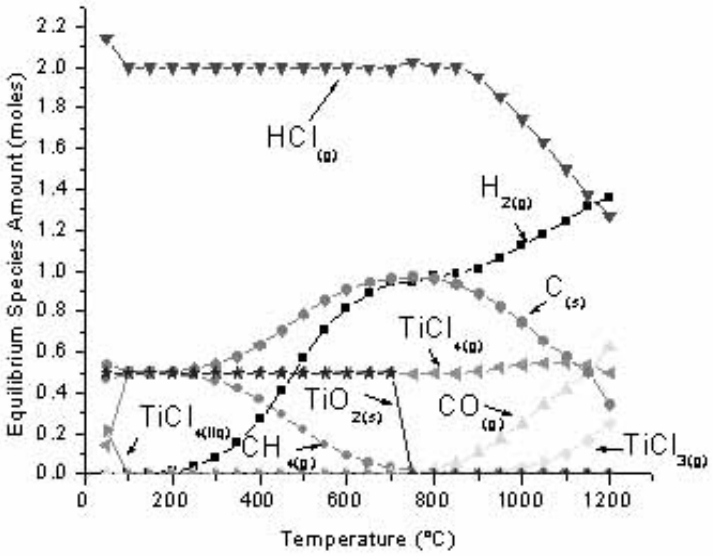

Figure 4.5: Thermodynamic simulation of potential reaction products produced during H_2 annealing in CDC that is produced from a Ti containing carbide: $H_{2(g)} + C_{(s)} + Cl_{2(g)} + O_{2(g)} + TiCl_{4(g)}$ were introduced in the following mole ratio: 1:1:1:1:1.

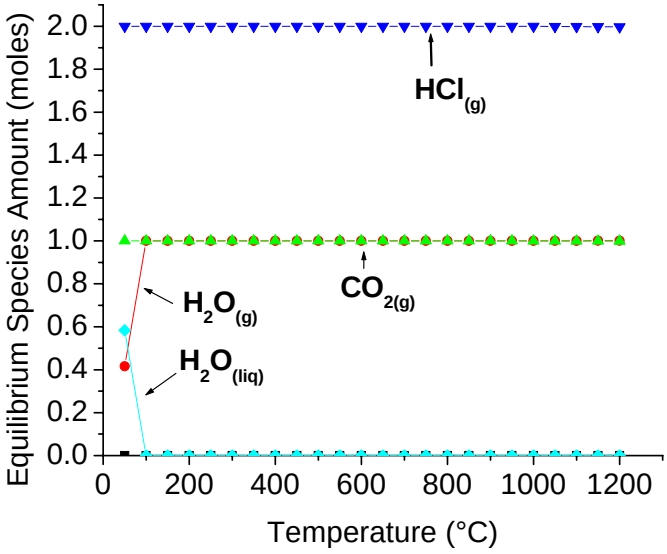

Figure 4.6: Thermodynamic simulation of potential reaction products produced during H_2 annealing in CDC: $H_{2(g)} + C_{(s)} + Cl_{2(g)} + O_{2(g)} + H_2O_{(g)}$ were introduced in the following mole ratio: 1:1:1:1:1.

4.2 Characterization

4.2.1 Powder X-ray diffraction

X-ray diffraction patterns of carbon powders obtained in the 200-1200 °C temperature range are shown in Figure 4.7. Chlorination, using a moderate Cl_2:carbide ratio of ~10:1 for 3 h at 200 °C, was not complete as evidenced by the remaining peaks of Ti_3SiC_2. However, at treatment temperatures as low as 400 °C all Ti_3SiC_2 peaks vanish, signifying no crystalline material remained within the carbon (see Figure 4.7). For Ti_2AlC-CDC, amorphous carbon formation occurred at temperatures as low as 400 °C, see Figure 4.8.

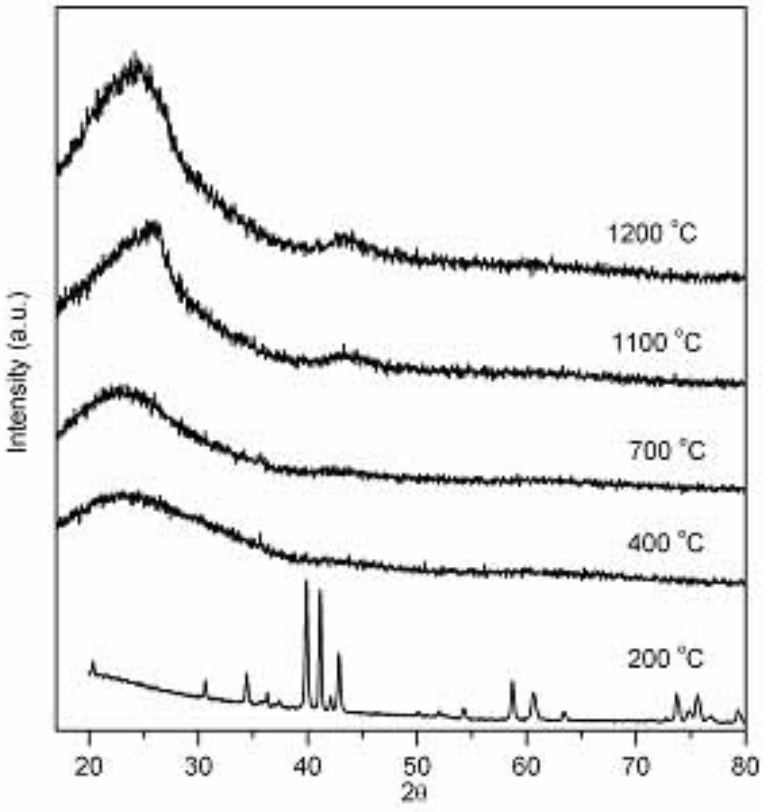

Figure 4.7 X-ray diffraction patterns of Ti_3SiC_2-CDC produced at temperatures from 200-1200 °C. Chlorination time was 3 h.

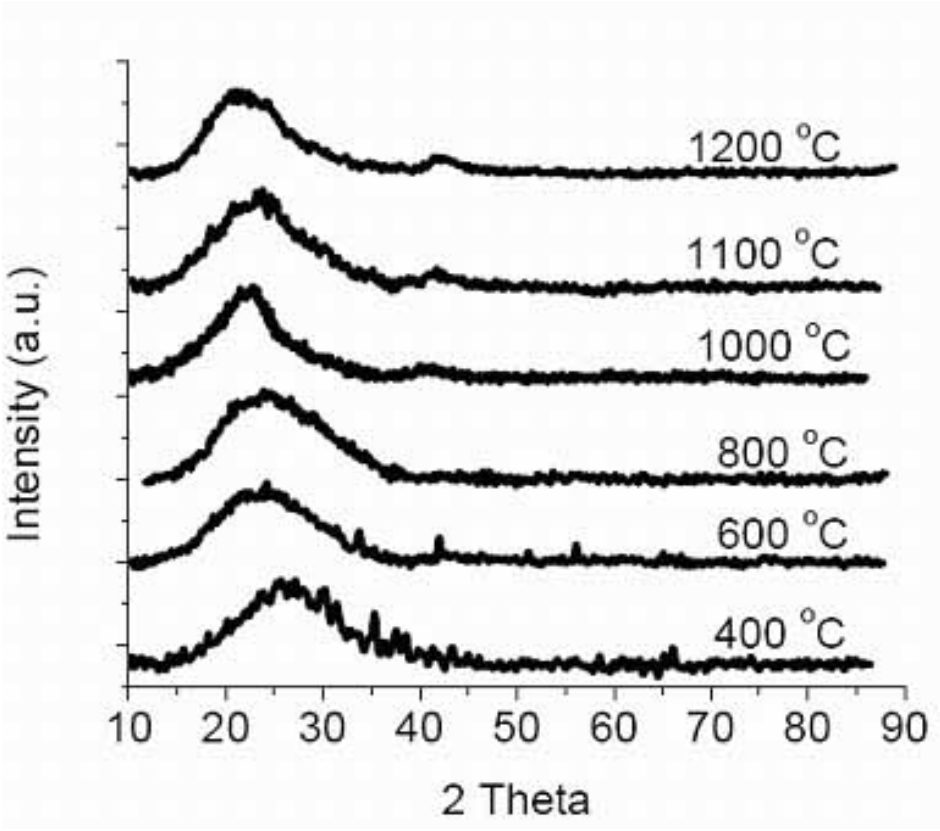

Figure 4.8 X-ray diffraction patterns of Ti_2AlC-CDC produced at temperatures from 400-1200 °C. Chlorination time was 3 h.

Similar results were obtained for Ti_3AlC_2-CDC and Ta_2AlC-CDC (not shown). Differences between thermodynamic simulations and actual experimental X-ray diffraction results are due to the software assumption of a closed system, while the actual chlorination process is an open system with the gas flow driving the chlorination reaction towards the right, following Le Chatelier's principle. Kinetics of the reaction are also a factor. The carbides were chlorinated for 3 h, and the reaction at lower temperatures may require longer periods of time for complete metal removal to occur.

4.2.2 Raman Spectroscopy

The carbon ordering within the CDC was determined using Raman spectroscopy. Defect-free graphite results in only one Raman active mode, the G-band, located at 1582 cm^{-1}. This peak corresponds to graphite in-plane vibrations with E_{2g} symmetry [78, 79]. Graphite containing defects and disordered carbons will show an additional band at ~1350 cm^{-1} (D-band) when using an excitation wavelength of 514 nm. Depending on the structure of the disordered carbon and the excitation wavelength used, the position of these bands may vary [80-82]. The D-peak is associated with breathing vibrations of sp^2 rings, which is inhibited in perfect graphite [81, 83].

In addition to the D-band, the D'-band, located at 1620 cm^{-1} is also a sign of disorder [84]. Located in close proximity to the G-band, the D'-band is observed as a shoulder of the G-band when the material becomes more ordered due to the narrowing of the G-band.

4.2.2.1 Ti_3SiC_2 Derived Carbon

Raman spectra of Ti_3SiC_2-CDC indicate the formation of carbon at temperatures as low as 200 °C, as predicted by the thermodynamic calculations to occur at low or moderate carbide/Cl_2 ratios, see Figure 4.1. The spectra from samples prepared in the 200 °C to 1200 °C temperature range exhibited strong peaks for both D- and G-bands, confirming the conversion to carbon for Ti_3SiC_2–CDC (Figure 4.9). The peak shift was observed for both bands as a function of synthesis temperature (Figure 4.9b). The peak shift for the D-band suggests a change in the vibrations caused by a change in the disorder in the formed carbon. The peak around 1580 cm^{-1} is a combination of the G- and D'-bands. As the D'-band becomes narrower and more pronounced due to a change in the disorder of the carbon structure, the G-band will appear to shift to the left with the

formation of an asymmetric peak due to the D' contribution at 1620 cm^{-1}. The actual G-band does not shift. The change in full width at half maximum (FWHM) of the D- and G-bands with chlorination temperature occur with a drop from 240 cm^{-1} to 60 cm^{-1} for the D-band, and a drop from 120 to 50 cm^{-1} for the G-band over the temperature range of 200-1200 °C (see Fig. 4.9c).

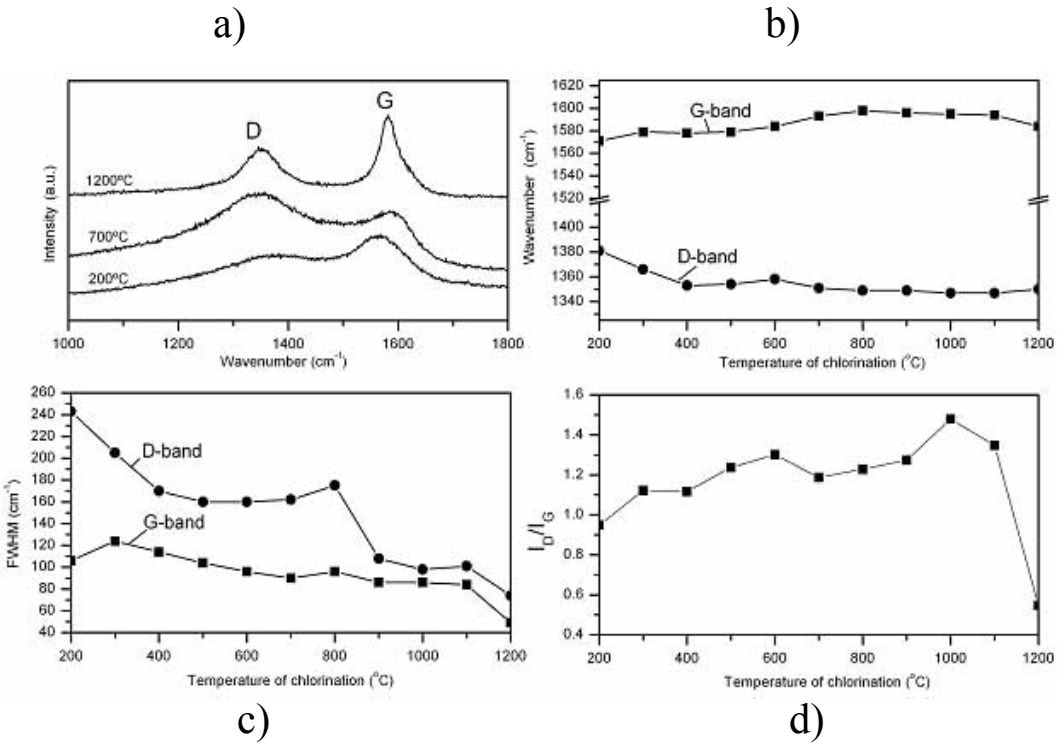

Figure 4.9 Raman spectra of carbon produced by chlorination of Ti_3SiC_2 for 3 hours in the 200°C-1200°C temperature range (a), positions of D- and G-bands as a function of temperature (b), FWHM of the D- and G-bands as a function of temperature (c), and the integrated intensity ratio of the D and G bands (d).

This result confirms the formation of disordered carbon upon chlorination of Ti_3SiC_2-CDC. The minimal change in FWHM as a function of chlorination temperature (Fig. 4.9c) suggests minimal ordering occurs within the disordered carbon in this temperature range.

4.2.2.2 Ti_3AlC_2 Derived Carbon

Strong D- and G-peaks were also observed for Ti_3AlC_2-CDC (Figure 4.10). A decrease from 110-70 cm^{-1} occurred in the full width at half maximum (FWHM) of the G-band, however, a larger decrease in the D-band occurred from 250 to 120 cm^{-1} with increasing chlorination temperature, see Figure 4.10a. As the chlorination temperature increases from 400 to 1200 °C, the D-band narrows significantly. The ratio of integrated intensities of the D-and G-bands (I_D/I_G) followed a general trend of decreasing with increasing chlorination temperatures up to 1200 °C, see Figure 4.11b.

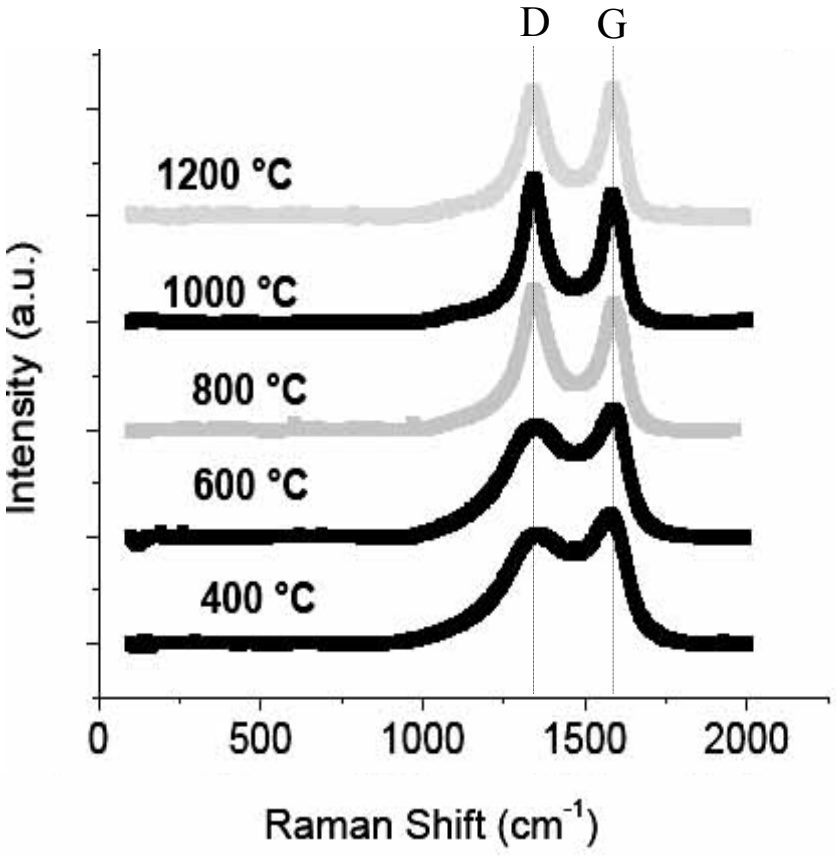

Figure 4.10 Raman spectra of Ti_3AlC_2-CDC produced over the temperature range of 400 -1200 °C. The D-band is shown at 1320 cm^{-1}, G-band at 1580 cm^{-1}.

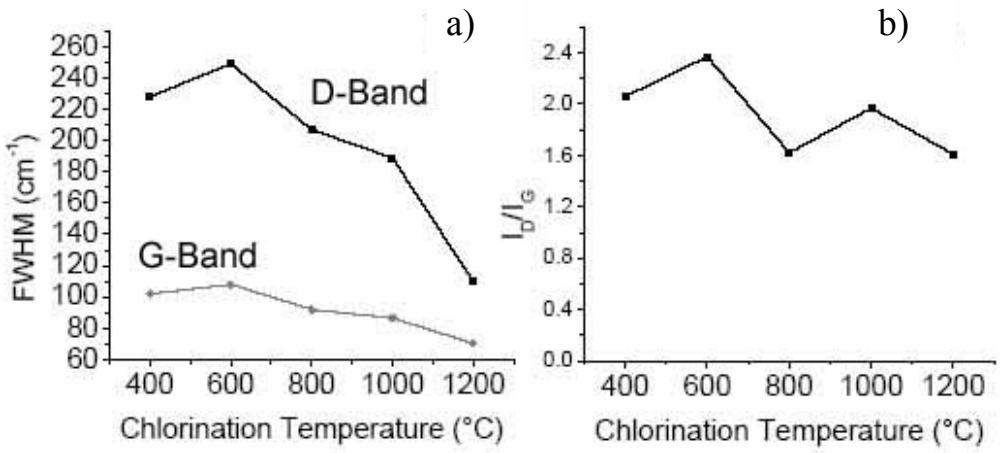

Figure 4.11 Chlorination temperature influence on FWHM (a), and I_D/I_G ratio (b) from Raman spectra of Ti_3AlC_2-CDC produced over the temperature range of 400 -1200 °C.

Also, a peak shift occurs as the chlorination temperature increases with the D-band shifting from 1325 to 1318 cm^{-1}. The peak comprised of a combination of G- and D'-bands also shifts slightly from 1582 to 1591 cm^{-1} at chlorination temperature of 600 °C, followed by a shift towards lower Raman shift values of 1578 cm^{-1} at a chlorination temperature of 1200 °C. The change in peak locations suggest a change in the bonding of disordered carbon, as noted by the shift in the D-band and the increase in the intensity of the D'-band.

4.2.2.3 Ti_2AlC Derived Carbon

Raman spectra of the Ti_2AlC-CDC indicate the formation of carbon at chlorination temperatures as low as 400 °C, as predicted by thermodynamic calculations to occur at low or moderate Ti_3AlC_2/Cl_2 ratios, see Figure 4.12. Higher chlorination temperatures result in the narrowing of the carbon bands, particularly the D-band, indicating an increase in order, see Figure 4.12. The D-band narrows from 280 to 120 cm^{-1} from 400 to 1000 °C. After 1000 °C, only minimal ordering occurs, similar to the

Ti_3AlC_2-CDC results. The temperature dependence of the ratio of integrated intensities of disorder-induced D band and the graphitic G-band (I_D/I_G) is shown in Figure 4.12c. The I_D/I_G ratio drops from 400 °C to 1000 °C, followed by a slight increase from 1000 °C to 1200 °C.

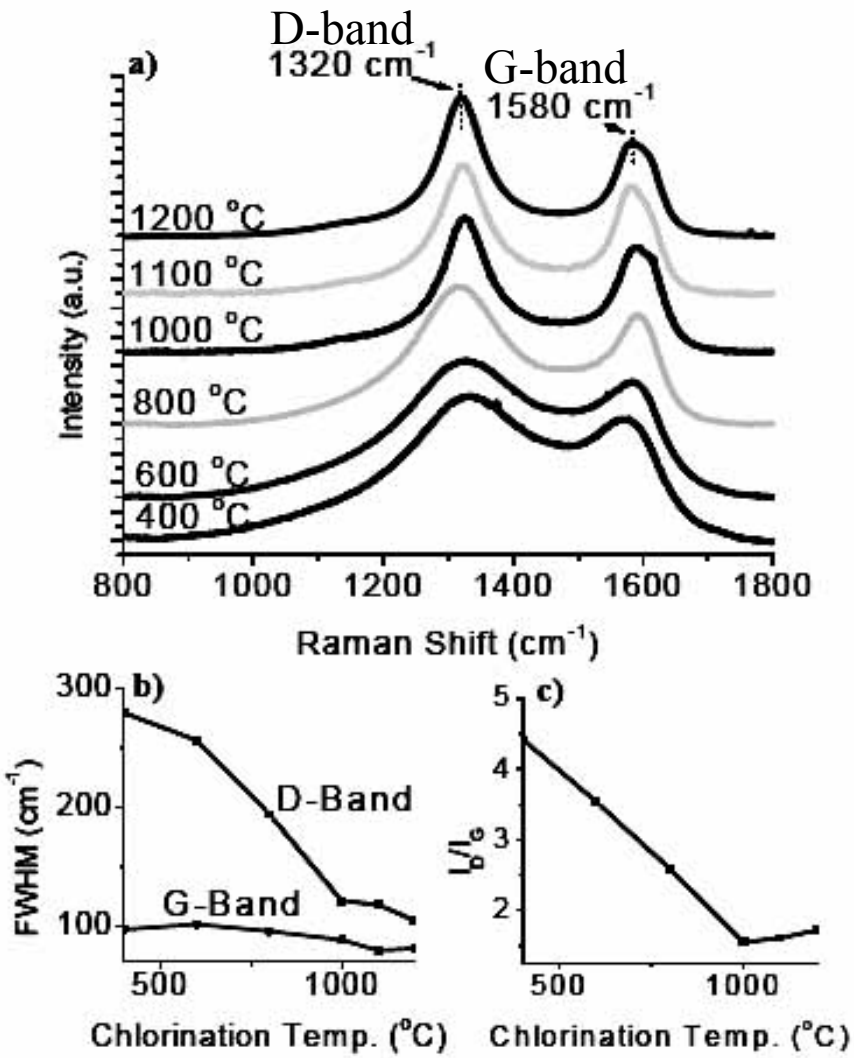

Figure 4.12 Raman spectra of Ti_2AlC-CDC produced over the temperature range of 400 -1200 °C (a), the change in FWHM with chlorination temperature (b), and the ratio of D- and G-band intensities (c). The D-band is shown at 1320 cm^{-1}, G-band at 1580 cm^{-1}.

At higher chlorination temperatures of 1000 °C and above, a clear shoulder develops on the right of the G-band at 1620 cm^{-1}, which illustrates the rise of the D'-band. This D'-band is evidence that disorder remains in the carbon, and is pronounced due to the narrowing of the peaks as the disordered carbon becomes increasingly graphitic.

The peaks of the D- and G-bands slightly shift with chlorination temperature. As the chlorination temperature increases from 400 to 600 °C, the combination of the G- and D-bands shifts to a higher wavenumber of 1590 cm^{-1}, then starts to decrease to 1578 cm^{-1} as the chlorination temperature continues to increase. The D-band shifts from 1331 to 1318 cm^{-1} as the chlorination temperature increases from 400-800 °C. At higher chlorination temperatures of 1000-1200 °C, the D-band jumps to 1322 cm^{-1}, and approximately remains at that wavenumber throughout the chlorination temperatures. The shifting of the D-band toward the standard location of 1320 cm^{-1} signifies the disorder within the material is becoming more like the ideal disorder generally associated with the D-band. At low chlorination temperatures, the disorder is mainly attributed to amorphous carbon. As the chlorination temperature increases, larger volumes of ordered graphitic ribbons form, which also have a degree of disorder associated with them. The shift in the D-band illustrates the change in origin of the disorder.

The results suggest that CDC produced from Ti_2AlC is disordered and that with increasing chlorination temperature, the degree of disorder decreases up to 1000 °C. Above 1000 °C, the degree of order within the carbon structure is similar.

4.2.2.4 Ta_2AlC Derived Carbon

The results for Ta_2AlC-CDC suggest the amount of ordered carbon increases with increasing chlorination temperature, Figure 4.13. The FWHM of the D-band slightly increases from 400-600 °C, followed by a steady decline until 1200 °C, see Figure 4.14a. Unlike Ti_2AlC-CDC and Ti_3AlC_2-CDC, the amount of disorder within the carbon decreases significantly as indicated by FWHM decrease between 1000-1200 °C from 200-110 cm^{-1} (Fig. 4.14a). The I_D/I_G ratio suggests a trend of increasing order within the carbon structure with increasing chlorination temperature. (Fig. 4.14b)

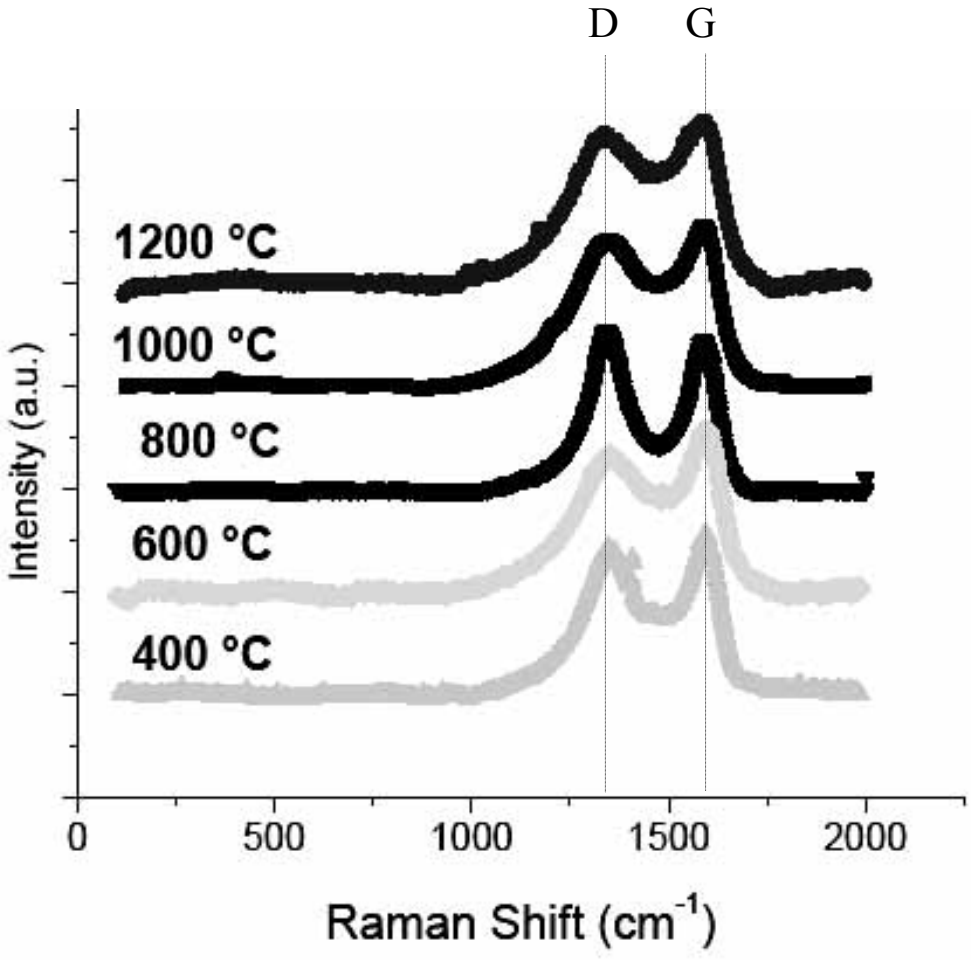

Figure 4.13 Raman spectra of Ta_2AlC-CDC produced over the temperature range of 400-1200 °C. The D-band is shown at 1320 cm^{-1}, G-band at 1580 cm^{-1}.

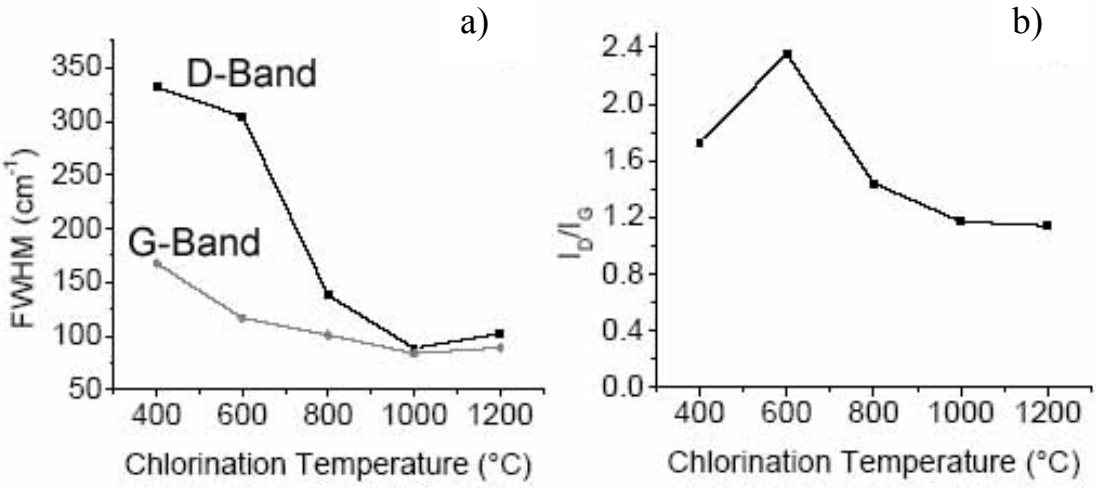

Figure 4.14 Chlorination temperature influence on FWHM (a), and I_D/I_G ratio (b), from Raman spectra of Ta_2AlC-CDC produced over the temperature range of 400 -1200 °C.

A slight shift in the location of the D-band and combination of G- and D'-bands is observed in the Raman spectra as the chlorination temperature increases. From 400 to 600 °C, the location of the D-band decreases from 1328 to 1321 cm^{-1}, while the G band remains constant at 1586 cm^{-1} in the temperature range. (Fig. 4.13) At higher chlorination temperatures, the G-band drops to 1578 cm^{-1} and stays constant throughout the temperature range of 1000 °C to 1200 °C, while the D-band continues to decrease from 1320 to 1315 cm^{-1}.

Common among all the MAX-phase derived carbons is an increase in ordering of the graphitic structure with increasing chlorination temperature. The disorder becomes more defined, as evidence by the narrowing of the D-band and the increasing presence of the D'-band. The D-band shifts location depending on the chlorination temperature, suggesting that bonding within the disordered carbon is changing, as well as the surface termination is changing as the chlorination temperature increases. The shift in the D-

band is evidence to suggest that at low chlorination temperatures surface impurities such as Cl_2 and metal chlorides are present in CDC.

4.2.3 Transmission electron microscopy

TEM studies of CDCs formed at various temperatures revealed their microstructure at the atomic scale.

4.2.3.1 Ti_3SiC_2 Derived Carbon

Samples chlorinated at 300, 700, and 1200 °C were imaged using TEM, see Figure 4.15. At low chlorination temperatures, amorphous carbon was formed (Fig. 4.15a). Ordering of carbon, and the formation of graphitic structures on the surface of carbon particles starts at ~ 700°C (Fig. 4.15b). The TEM micrograph of a sample processed at 1200 °C shows a network of well-ordered graphite sheets, see Figure 4.15c. They are relatively thin; most ribbons are comprised of less than 10 graphene sheets with the average ribbon thickness comprised of 3 graphene sheets. The thicknesses of the ribbons are too small to produce sharp (002) graphite peaks in the XRD spectra. Since the G-band in the Raman spectra comes from in-plane vibrations, the thin graphite ribbons can more efficiently be detected by Raman spectroscopy. Therefore, the agreement between the Raman spectroscopy results and TEM images is logical, despite the lack of evidence from X-ray diffraction on the increased order in the carbon structure.

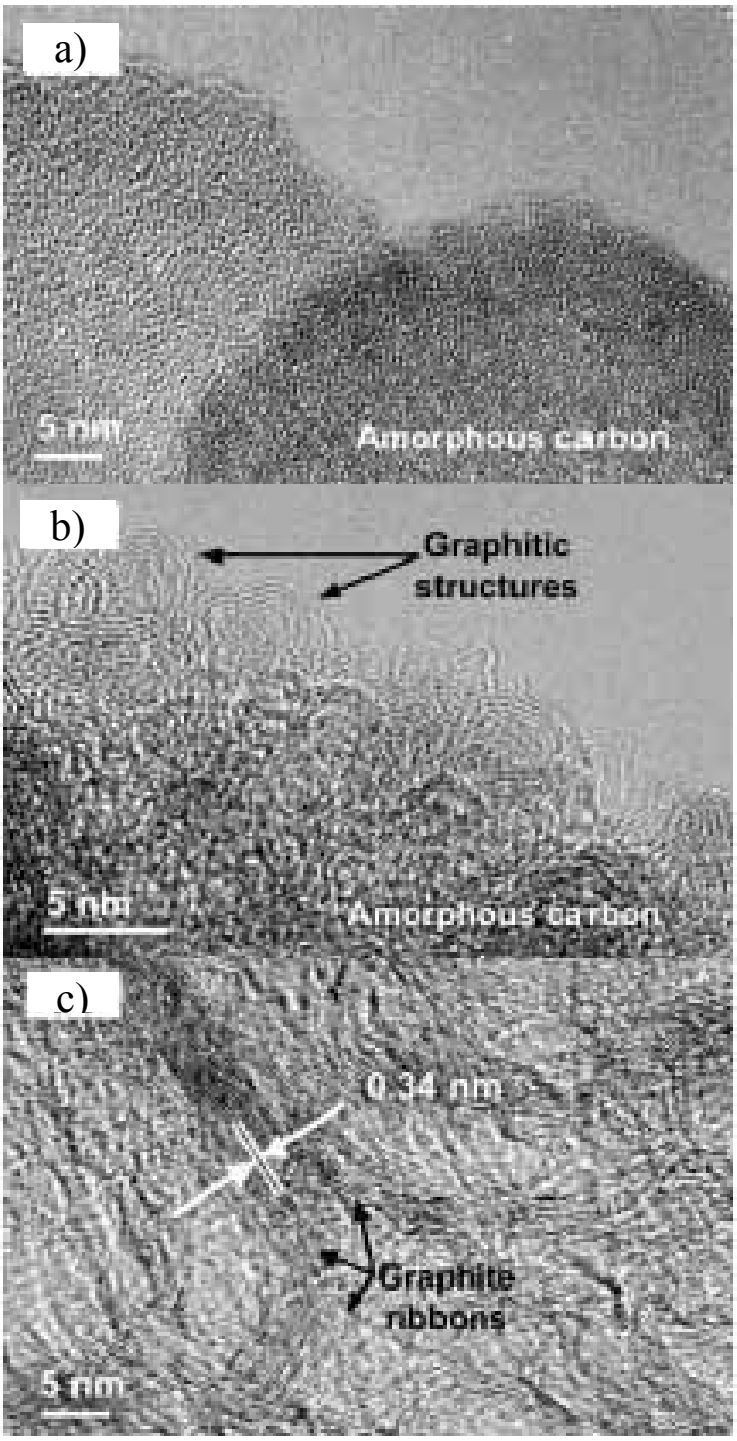

Figure 4.15 TEM images of Ti_3SiC_2-CDC produced at, (a) 300 °C, (b) 700 °C, and, (c) 1200 °C. CDC produced at low temperature is completely amorphous. At higher temperatures, graphite fringes start to appear, demonstrating the beginning of the structure ordering. Pronounced graphitization is observed at 1200 °C. All scale bars are 5 nm.

4.2.3.2 Ti_3AlC_2 Derived Carbon

TEM images were captured from samples produced using chlorination temperatures of 400, 600, 800, and 1200 °C, see Figure 4.16. The 400 °C sample is primarily amorphous carbon, similar to the Ti_3SiC_2-CDC sample (Fig. 4.16a). As the chlorination temperature is increased to 800 °C, the carbon structure becomes more ordered on the surfaces of the carbon particles (Fig. 4.16b). At chlorination temperatures of 1000 °C (Fig. 4.16c), the carbon structures organize further into structures reminiscent of such found in Ti_3SiC_2-CDC material chlorinated at 700 °C (Fig. 4.15b). At process temperatures of 1200 °C, graphitic ribbons are noticeable throughout the carbon particles. (Fig. 4.16d)

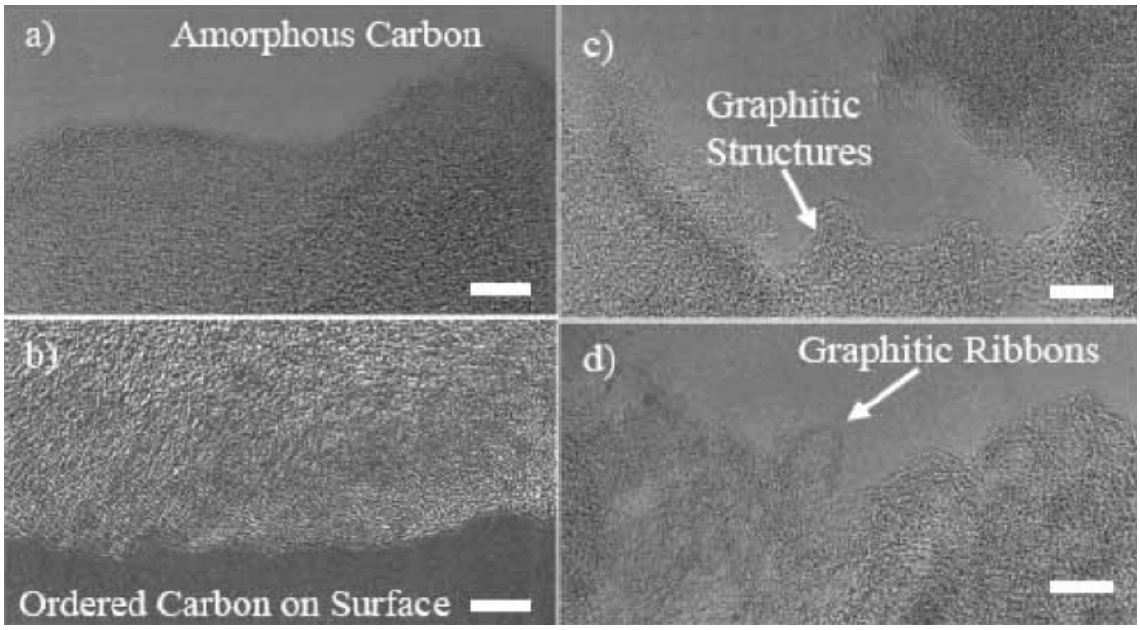

Figure 4.16 TEM micrographs of Ti_3AlC_2-CDC produced at, a) 400 °C, b) 800 °C, c) 1000 °C, d) 1200 °C. All scale bars are 5 nm in length.

4.2.3.3 Ti_2AlC Derived Carbon

TEM images of powder Ti_2AlC-CDC revealed similar results as Ti_3SiC_2-CDC and Ti_3AlC_2-CDC. Ti_2AlC-CDC powders chlorinated at 400 °C were comprised mainly of amorphous carbon, see Figure 4.17a. Increasing the processing temperature to 800°C

resulted in the formation of various graphitic structures located on the surface of the particles, which were often sharply twisted at the edges of most particles with characteristics similar to multi-walled nanotubes (Figure 4.17b). Similar curved graphitic structures were also observed in CDC produced at 700 °C from Ti_3SiC_2–CDC and 800 °C for Ti_3AlC_2-CDC (Fig. 4.15b and 4.16b). A considerable amount of amorphous and turbostratic carbon was also present in this sample. A significant increase in the ordering of the carbon structure was observed in samples chlorinated above 1000 °C (Figs. 4.17c and d). These CDCs consisted of graphite ribbon networks and amorphous carbon. No curved graphitic structures were found in these samples. CDCs produced at 1000 °C (Fig. 4.17c) and 1200 °C (Fig. 4.17d) exhibited similar morphologies, which was suggested based on the Raman spectroscopy results.

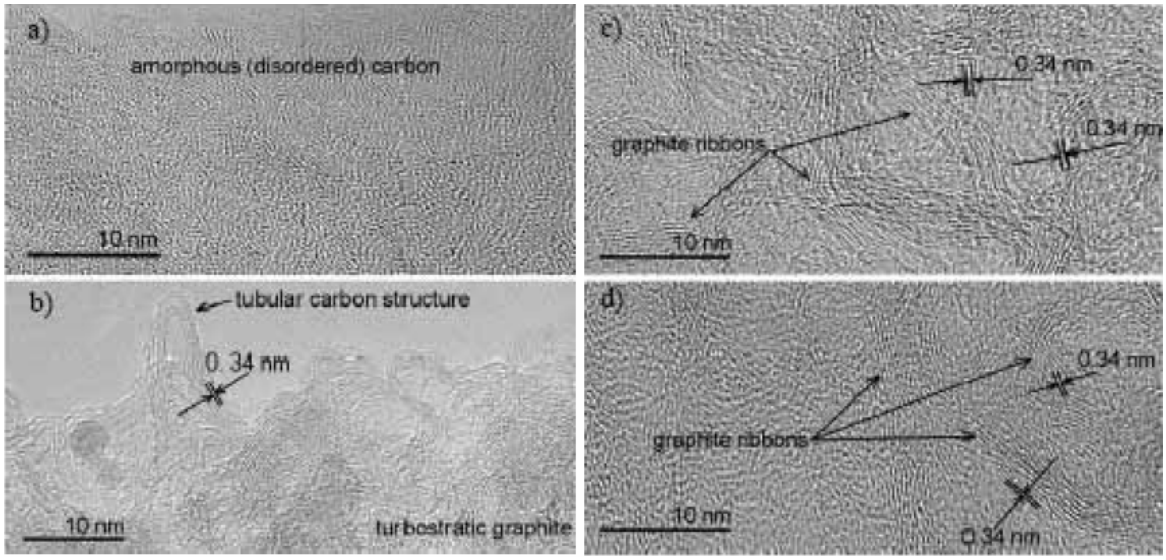

Figure 4.17 TEM micrographs of Ti_2AlC-CDC produced at, a) 400 °C, b) 800 °C, c) 1000 °C, d) 1200 °C.

Overall, the TEM results confirm the Raman spectroscopy results, suggesting increased graphitization of the CDC structure at elevated temperatures, with small

changes in degree of graphitization occurring in the CDCs prepared in the 1000-1200°C temperature range.

4.2.3.4 Ta_2AlC Derived Carbon

TEM images were obtained for Ta_2AlC samples chlorinated at 400, 800, and 1200 °C, see Figure 4.18. The 400 °C sample was completely amorphous with no signs of the development of an ordered carbon structure (Fig. 4.18a). The samples chlorinated at 800 °C showed signs of an ordered carbon structure development, with graphitic-like areas organizing on the surface of the carbon particles (Fig. 4.18b). The 1200 °C sample showed a clear ordering throughout the carbon particles (Fig. 4.18c). Long graphitic ribbons were abundant throughout this material. Here again, the TEM results confirm the Raman microspectroscopy results with an increase in ordering of the carbon structure with chlorination temperature.

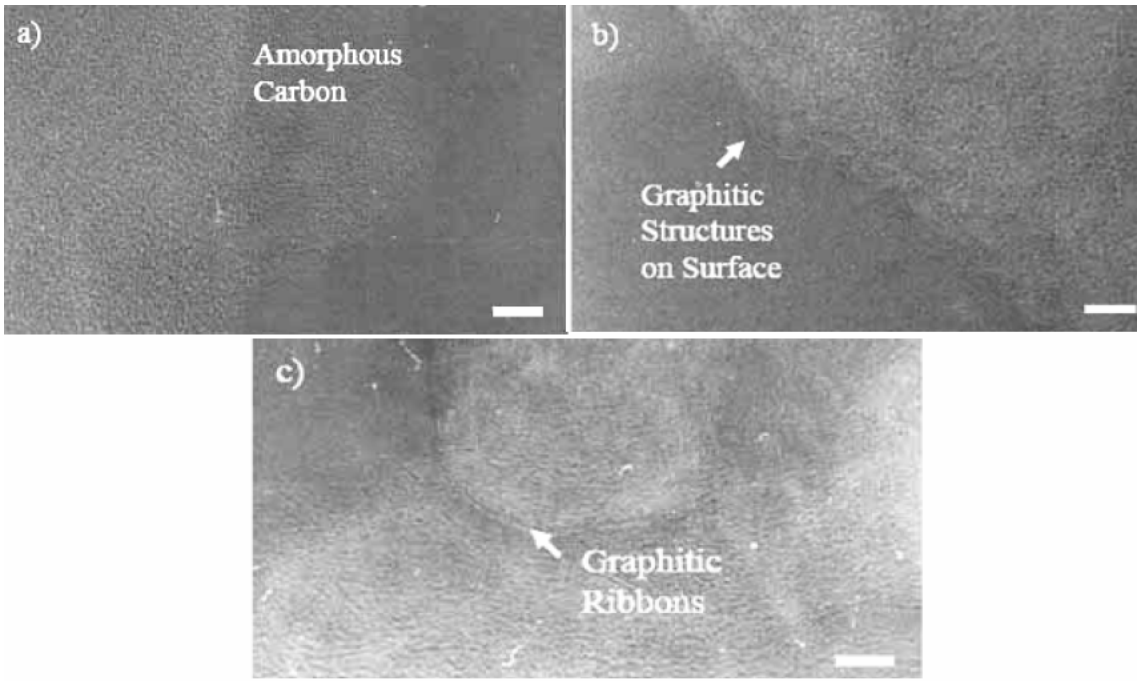

Figure 4.18 TEM micrographs of Ta_2AlC-CDC produced at, a) 400 °C, b) 800 °C, c) 1200 °C. All scale bars are 5 nm in length.

4.2.4 Scanning electron microscopy and energy-dispersive X-ray spectroscopy

4.2.4.1 Lamellar Structure

The lamellar structure within the ternary carbide grains is clearly seen in the SEM micrograph of a fractured surface, see Figure 4.19b. The chlorination process is conformal even on a microscale, with no change in shape occurring in the lamellar Ti_3SiC_2 grains, as evidenced by the SEM micrograph of a CDC fractured surface (Fig. 4.19b).

It was also found that the chlorination process resulted in a formation of intergranular and intragranular cracks within the CDC material. Cracks have been observed in Ti_3SiC_2, Ti_3AlC_2, Ti_2AlC, Ta_2AlC, and $Ti_2AlC_{0.5}N_{0.5}$. These cracks are believed to be caused by contraction of the CDC material within a grain in the direction normal to basal planes of the carbide. This is best seen in Figure 4.19b, where a crack formed between two grains of Ti_3SiC_2–CDC which were oriented perpendicular to each other before chlorination. Thermal stresses generated during cool down of partially chlorinated samples (i.e. at the CDC/Ti_3SiC_2 interface (Fig. 4.19c) do not cause additional cracking or fracture in CDC. For example, a considerably smaller degree of cracking and no intergranular cracking was observed in case of chlorination of SiC [85]. The difference in tendency for MAX-phase carbides to form cracks over isotropic binary carbides, such as SiC, results from differences in the atomic structure of the two carbides and the final densities of the obtained CDCs. In the case of SiC, carbon is uniformly distributed within a stoichiometric diamond lattice, while carbon atoms presumably form layers in the anisotropic Ti_3SiC_2 structure.

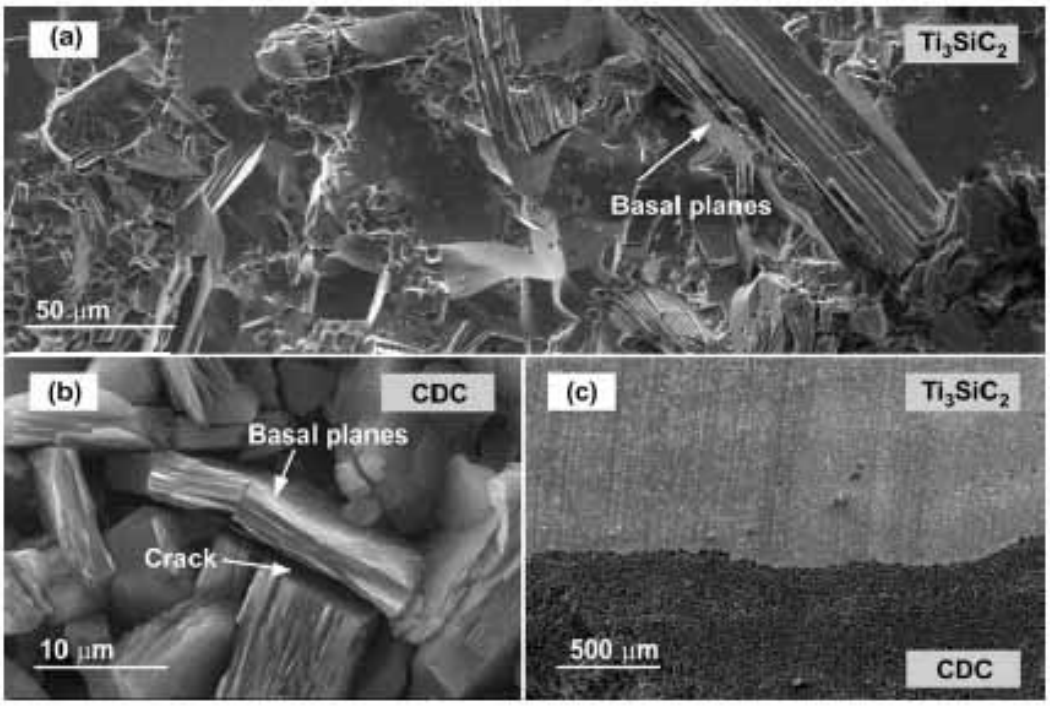

Figure 4.19 SEM micrographs of the samples. (a) Fracture surface of an as-received Ti_3SiC_2 sample, (b) a CDC sample, chlorinated for 3 hours at 600°C, and (c) cross-section of the interface between Ti_3SiC_2 and CDC, formed by 3 hours chlorination at 900 °C of a bulk 3mm x 15mm x 15mm Ti_3SiC_2 sample.

Figure 4.20 shows the atomic structure of Ti_3SiC_2 [86, 87]. Carbon atoms in this image are shown as small black dots, silicon and titanium atoms as filled and open circles, respectively. The distribution of carbon atoms in Ti_3SiC_2 is non-uniform and layered; the highest planar density of carbon exists in the close-packed (basal) planes. In the CDC process, metal is extracted layer-by-layer from the rigid metal carbide lattice [64]. The carbon atoms, relocated from their original positions, create a carbon network structure. It is reasonable to assume that the uneven distribution of carbon atoms in MAX-phase carbides leads to a shrinkage during the chlorination process in the direction of the lowest linear density of carbon. In the MAX-phase carbide unit cell, this direction is the c-direction, see Figure 4.20b. A model of crack formation in the CDC produced from the polycrystalline carbide resulting from the anisotropy of shrinkage of Ti_3SiC_2 is

shown in Figure 4.20c. These microcracks may be useful in some applications of CDC, when adsorbing large molecules or when fast access to nanopores is required. However, they are not desirable in applications of CDC as molecular sieves of small molecules such as gases.

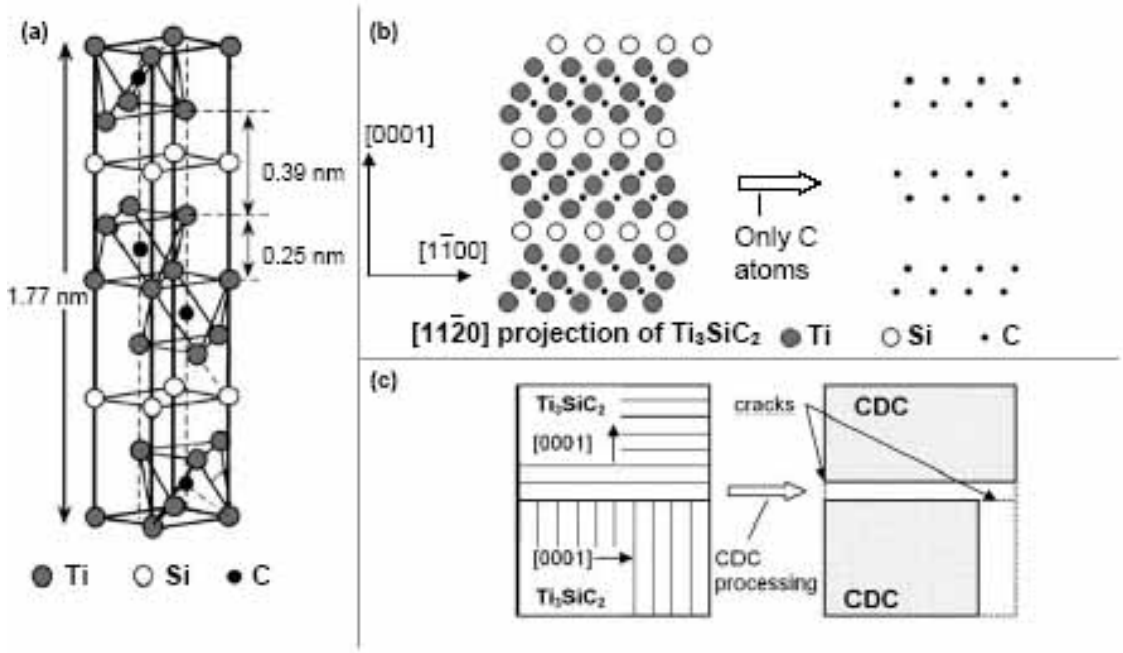

Figure 4.20 (a) Unit cell of Ti_3SiC_2. (b) Schematic of the lattice structure of Ti_3SiC_2 with and without Ti and Si atoms shown. (c) The proposed model of the observed after CDC processing generation of cracks between the grains. Contraction of CDC along [0001] direction of the former Ti_3SiC_2 is suggested.

This cracking phenomenon is even more apparent in $Ti_2AlC_{0.5}N_{0.5}$-CDC, see Figure 4.21a. After chlorination at 800 °C, significant cracks are present and are visible without the aid of a microscope. The cracking in the carbo-nitride material is a result of the extremely high theoretical pore volume. In addition to Ti and Al, nitrogen is also removed during the chlorination process leaving only carbon to support a lattice structure containing 7 void spaces which formally contained metals and nitrogen for every one carbon atom. The carbon atoms can no longer support the carbide structure, therefore the structure collapses, forming large cracks in the process.

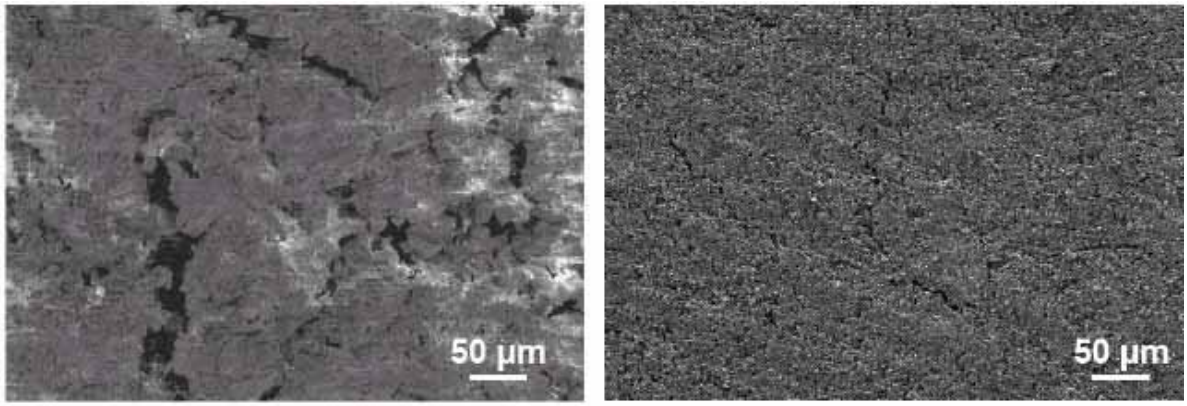

Figure 4.21 Crack formation in $Ti_2AlC_{0.5}N_{0.5}$-CDC (a), and Ti_3SiC_2-CDC (b), chlorinated at 800 °C for 3h.

4.2.4.2 EDS chemical analysis

The EDS study of Ti_3SiC_2-CDC, see Figure 4.22, suggests that chlorination temperatures above 400°C resulted in an almost complete removal of the metal atoms. For Ti_3SiC_2-CDC, at 300 °C, up to 11 at.% of Si, but no Ti was detected. This indicates preferential etching of Ti at the lower temperatures as predicted by thermodynamic modeling (see Figure 4.1). The CDC formed at low temperatures (300-400 °C) traps from 20 to 45 wt.% of Cl_2, even if cooling is done in Ar; when cooled in Cl_2, up to 65 wt.% of Cl_2 can be contained within the pores. Oxygen was found in considerable amount in the CDCs, particularly in samples chlorinated at low temperatures. This is believed to be mainly adsorbed from air as H_2O and CO_2 after the samples are removed from the furnace. Presumably, the amount of trapped gases decreases at higher temperatures due to increasing pore size [64]. For the samples produced during 1200 °C chlorination, less than 5 at. % of Cl_2 could be detected in the CDCs. The amount of Cl_2 in the CDC also decreases over time when samples are stored, presumably due to substitution of chlorine with CO_2, H_2O and other species from air.

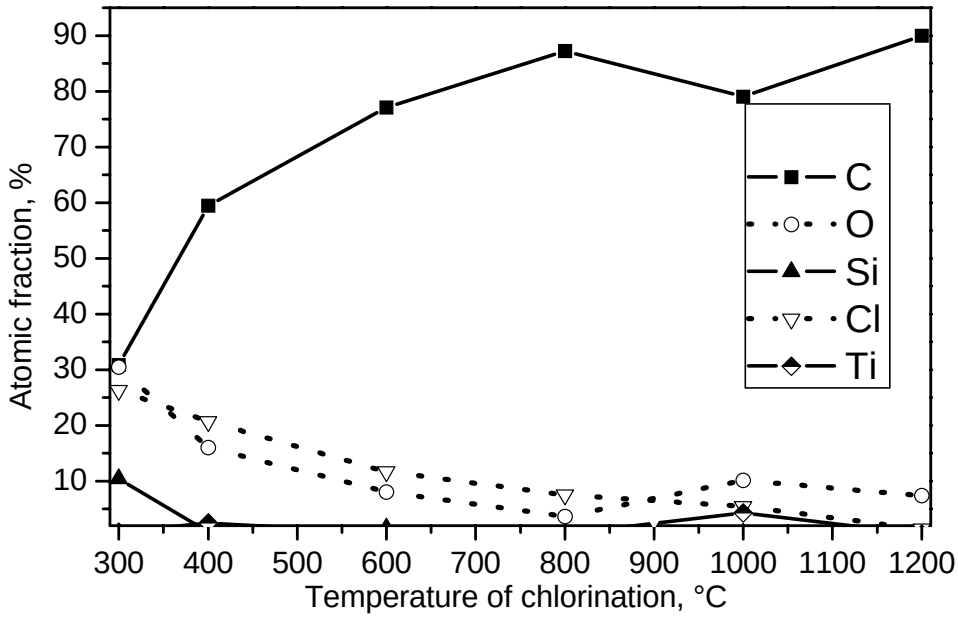

Figure 4.22 EDS analyses of CDC samples synthesized at different temperatures. Low temperature CDCs are capable of adsorbing considerable amount of gases. The presence of processing Cl_2 and atmospheric oxygen is evident.

4.3 Gas Sorption Analysis

4.3.1 Argon Sorption

4.3.1.1 Ti_3SiC_2 Derived Carbon

Argon sorption measurements were performed on Ti_3SiC_2-CDC chlorinated at 400, 600, 800, 1000, and 1200 °C for 3 h. The isotherms for the measurements are shown in Figure 4.23a. Material chlorinated at 400 and 600 °C displays a Type I isotherm, characteristic of a material lacking mesoporosity. Isotherms from samples chlorinated at 800, 1000, and 1200 °C exhibit a Type IV isotherm, suggesting the presence of larger pores due to the hysteresis. The isotherm with the largest hysteresis is from the 1000 °C chlorinated material. From the NLDFT analysis, a pore size

distribution was determined from the isotherms, see Figure 4.23b. With increasing chlorination temperature, the pore size tends to broaden with increasing amounts of pores above 2 nm. Figure 4.23c shows that Ti_3SiC_2-CDC chlorinated at 1000 °C contains the largest specific surface area based on both multipoint BET, 1460 m^2/g, and NLDFT, 1380 m^2/g, analyses. The pore volume increased with increasing chlorination temperature from ≈ 0.5 cc/g in material chlorinated at 400 °C, up to ≈1 cc/g in material chlorinated at 1000 °C; the pore volume then falls to 0.7 cc/g at 1200 °C, see Figure 4.23d.

4.3.1.2 Ti_3AlC_2 Derived Carbon

Argon adsorption analysis was performed on Ti_3AlC_2-CDC chlorinated at 600, 800, and 1200 °C. At chlorination temperatures of 600 °C a Type I isotherm is observed (Figure 4.24a), and the resulting DFT pore size distribution illustrates the presence of micropores, with little occurrence of mesopores, see Figure 4.24b. At chlorination temperatures of 800 °C, Ti_3AlC_2-CDC shows a slight hysteresis and is reminiscent of a Type IV isotherm. The DFT pore size distribution starts to broaden and large pores develop. In material chlorinated at 1200 °C, the isotherm hysteresis is larger than the one measured at 800 °C (middle panel in Fig. 4.24b). The NLDFT pore size distribution illustrates a large volume of mesopores, as well as the presence of micropores. The BET specific surface area increases with increasing chlorination temperature from 950 m^2/g at a chlorination temperature of 600 °C to 1600 m^2/g at 1200 °C, see Figure 4.24c. From 600 to 800 °C, the DFT specific surface area decreases somewhat from 1020 m^2/g to 920 m^2/g. From 800 to 1200 °C, the specific surface area increases from 920 to 1230 m^2/g. (Fig. 4.24c) Both BET and DFT specific surface area analysis agree that the material chlorinated at 1200 °C possesses the largest surface area. The difference in results

between BET and DFT analysis for the 600 and 800 °C chlorination materials is not very high, and therefore, it can be concluded that the specific surface area for the 600 and 800 °C samples are about the same. The pore volume of the Ti_3AlC_2-CDC samples increases with increasing chlorination temperature from 0.49 to 0.57 to 0.99 cc/g (Fig. 4.24d).

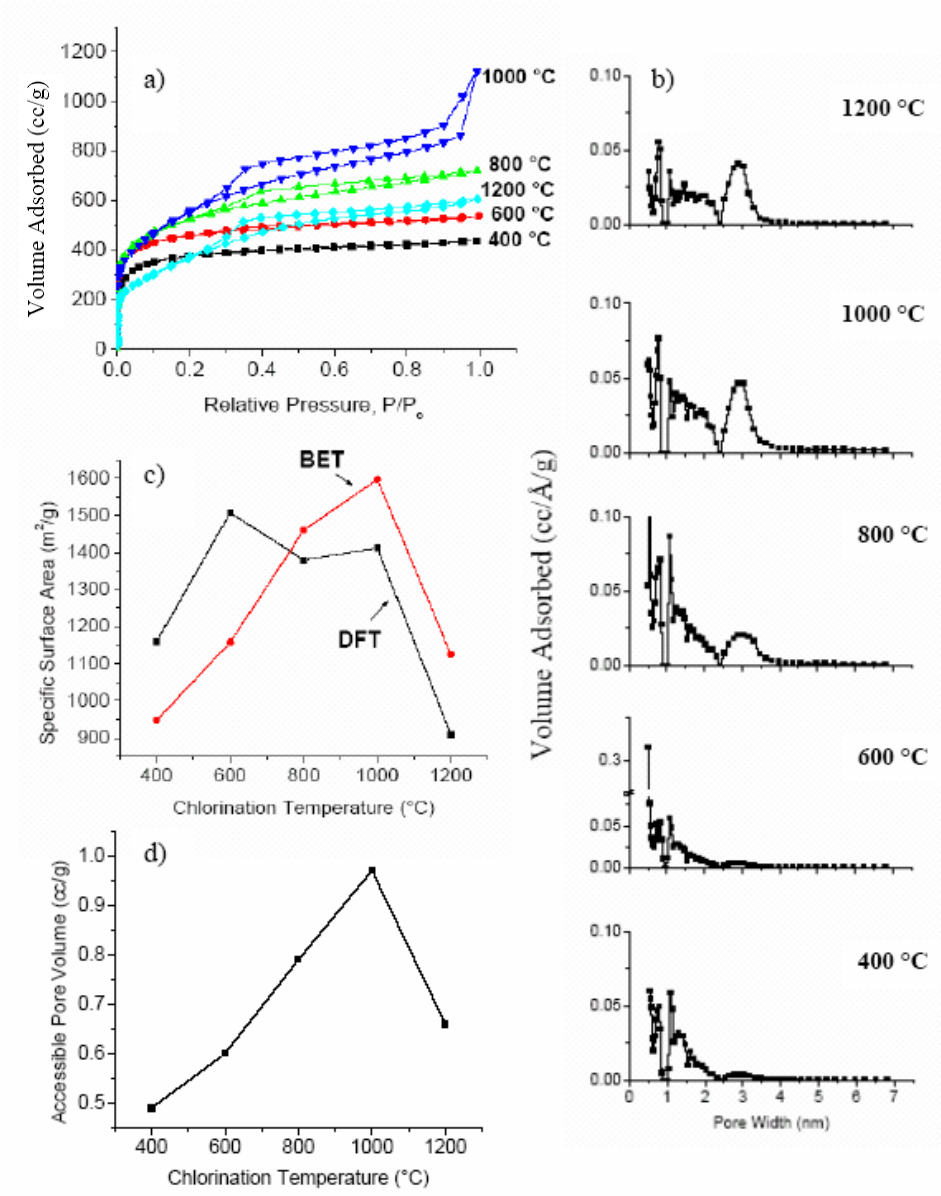

Figure 4.23 Ti_3SiC_2-CDC Ar sorption analysis a) isotherms of Ti_3SiC_2-CDC chlorinated at 400, 600, 800, 1000, and 1200 °C b) DFT pore size distribution with a confidence level of +/- 5% c) DFT and BET specific surface areas d) measured pore volume with a confidence level of +/- 5%.

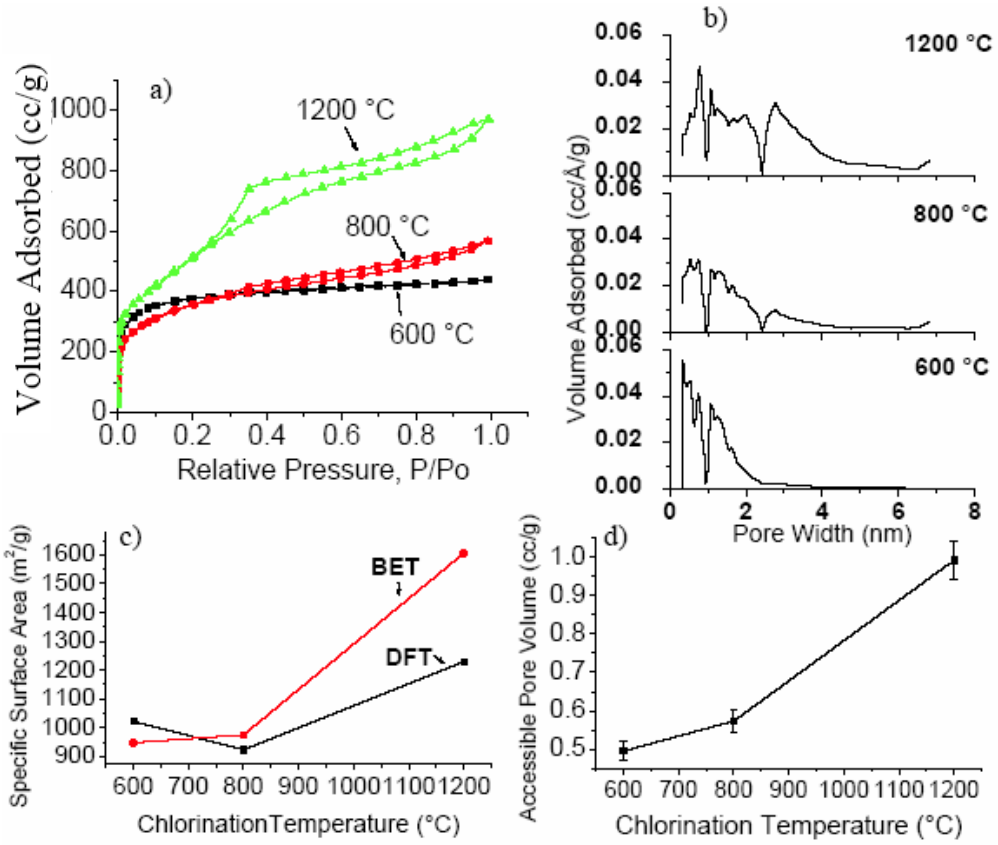

Figure 4.24 Ti_3AlC_2-CDC Ar sorption analysis, a) isotherms of Ti_3AlC_2-CDC chlorinated at 600, 800, and 1200 °C, b) DFT pore size distribution with a confidence level of +/- 5%, c) DFT and BET specific surface areas, d) measured pore volume with a confidence level of +/- 5%.

4.3.1.3 Ti_2AlC Derived Carbon

Argon sorption measurements were performed using Ti_2AlC-CDC chlorinated at 400, 600, 800, 1000, 1100 and 1200 °C. Similar to Ti_3AlC_2-CDC and Ti_3SiC_2-CDC, the material produced at lower chlorination temperatures (400 and 600 °C) exhibit a Type I isotherm, see Figure 4.25a. As the chlorination temperature is increased to 800, a small hysteresis forms within the isotherm and the maxminum volume of Ar adsorbed increases to 650 cc/g. The hystersis increases in size in the material chlorinated at 1000 °C, then further increases in material chlorinated at 1100 °C. The isotherms of Ti_2AlC-CDC produced at 1100 and 1200 °C are very similar in terms of the hysteresis size and the

maximum volume of Ar adsorbed (Fig. 4.25a). As the shape of the isotherms suggest, the DFT analysis shows a broadening of the pore size distributions with increasing chlorination temperature due to the development of pores greater than 2 nm (Fig. 4.25b).

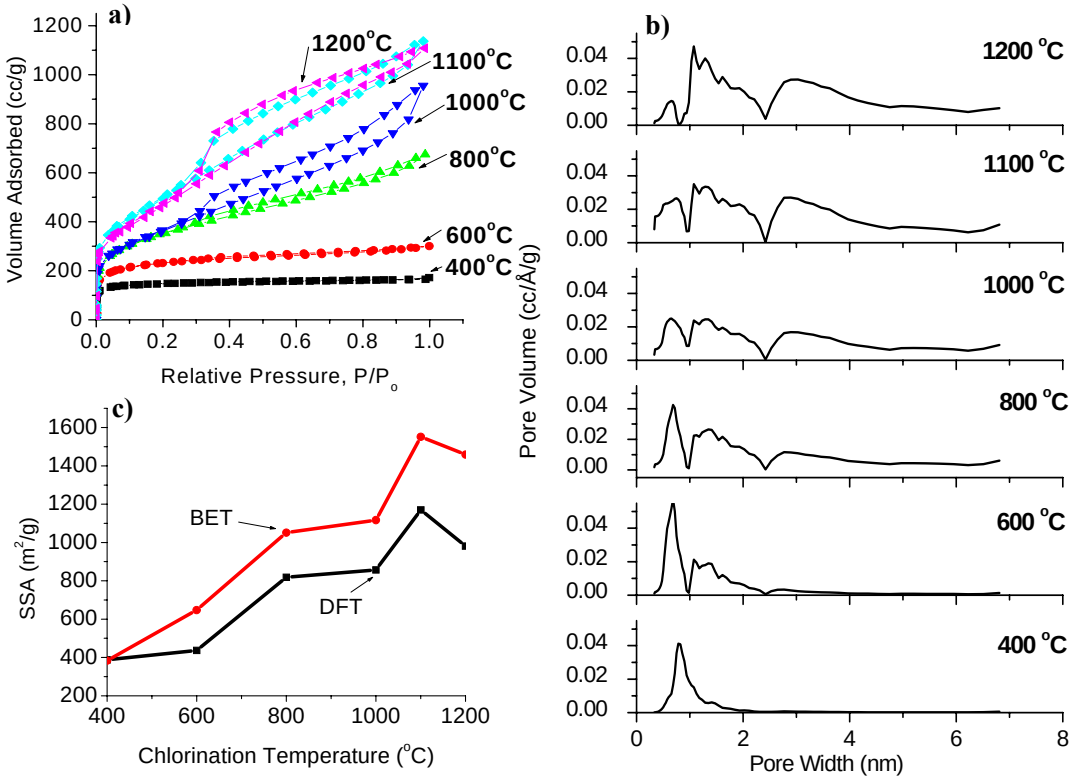

Figure 4.25 Ti_2AlC-CDC Ar sorption analysis, a) isotherms of Ti_2AlC-CDC chlorinated at 400, 600, 800, 1000, 1100 and 1200 °C, b) DFT pore size distribution, c) DFT and BET specific surface areas.

The BET and DFT specific surface areas increase with increasing chlorination temperature up to 1100 °C with values of 1575 and 1100 m^2/g, respectively, then fall to 1420 and 900 m^2/g at the 1200 °C chlorination temperatures (Fig. 4.25c). The pore volumes for Ti_2AlC-CDC increases steadily with chlorination temperature from 0.18 cc/g at 400 °C to 1.15 cc/g at 1200 °C.

4.3.1.4 Ta_2AlC Derived Carbon

Argon sorption analysis was performed on Ta_2AlC-CDC chlorinated at 800 and 1200 °C. The isotherms show a hysteresis characteristic of Type IV isotherms, see Figure 4.26a.

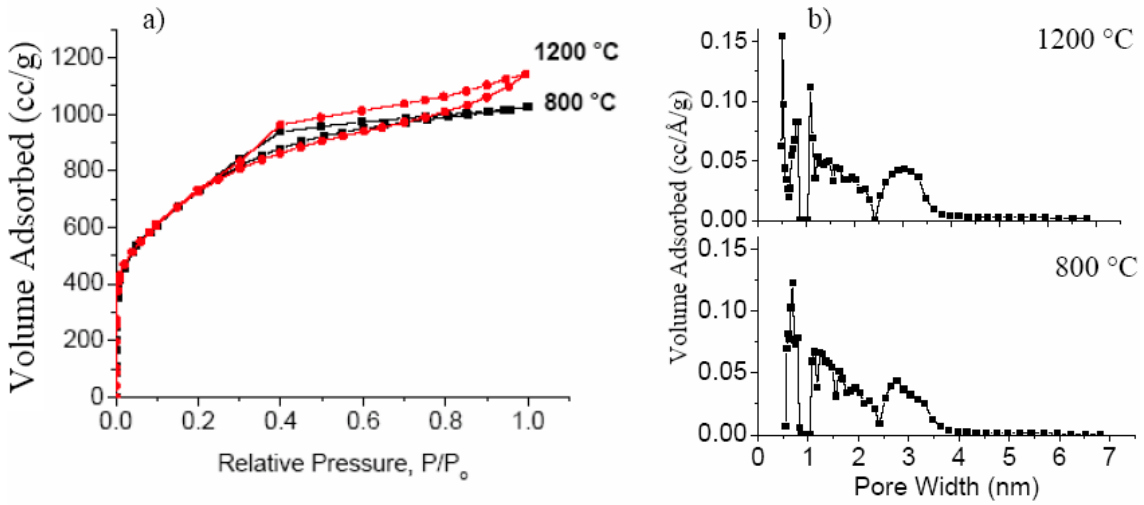

Figure 4.26 Ta_2AlC-CDC Ar sorption analysis, a) isotherms of Ta_2AlC-CDC chlorinated at 800 and 1200 °C, b) DFT pore size distribution.

The sorption isotherms further show that Ta_2AlC-CDC has a large capacity to adsorb, with maximum volumes of Ar adsorbed at ~1000 m^2/g for 800 °C and 1100 m^2/g for 1200 °C. The DFT pore size distribution confirms the presence of micro and mesopores. The BET specific surface area analysis (not shown) suggests surface areas for the 800 and 1200 °C samples to be ~2150 m^2/g. The DFT specific surface area analysis suggests surface areas for the 800 and 1200 °C samples to be 1600 and 1740 m^2/g, respectively. Although the magnitudes for the two different methods vary, both methods agree that Ta_2AlC-CDC possesses a higher specific surface area than Ti_2AlC-CDC, Ti_3AlC_2-CDC, or Ti_3SiC_2-CDC produced at any temperature. The pore volume for the Ta_2AlC-CDC chlorinated at 800 and 1200 °C is 1.14 and 1.22 cc/g, respectively. The difference in pore volume is minimal, and therefore it can be concluded that the pore

volume is not heavily influenced by chlorination temperature in the temperature range examined.

4.3.1.5 Ta_2C Derived Carbon

Argon sorption analysis was performed on Ta_2C-CDC chlorinated at 800 °C, forming an isotherm similar to a Type IV see Figure 4.27a. The DFT specific surface area suggests a surface area of 1950 m^2/g; the BET method suggests 2673 m^2/g. Both methods suggest a specific surface area having a magnitude larger than any MAX-phase carbide derived carbon produced thus far. The pore volume associated with this material is 1.27 cc/g.

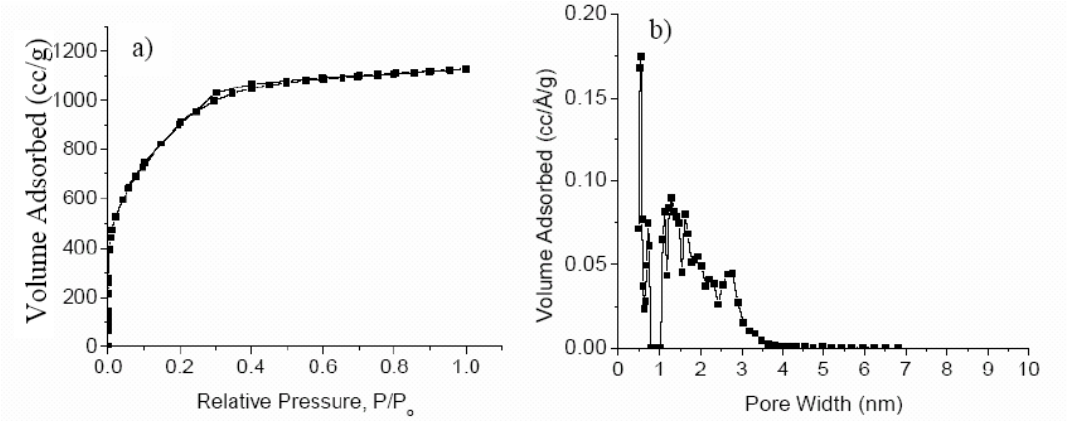

Figure 4.27 Ta_2C-CDC Ar sorption analysis, a) isotherms of Ta_2C-CDC chlorinated at 800 °C, b) DFT pore size distribution.

4.3.1.6 TaC Derived Carbon

Argon sorption analysis was performed on TaC-CDC chlorinated at 800 and 1200 °C. Both BET and DFT specific surface area analysis shows the specific surface area of around 2000 m^2/g. The pore volume increased with increasing chlorination temperature from 0.88 cc/g at 800 °C, to 1.04 cc/g at 1200 °C.

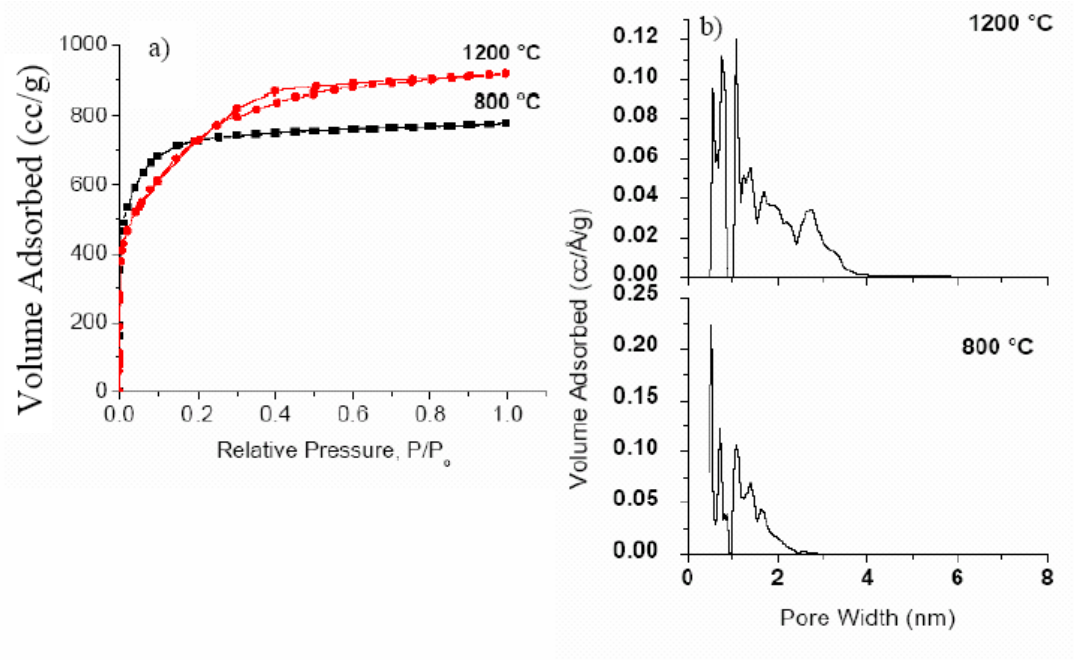

Figure 4.28 TaC-CDC Ar sorption analysis,a) isotherms of TaC-CDC chlorinated at 800 °C, and 1200 °C b) DFT pore size distribution.

4.3.1.7 $Ti_2AlC_{0.5}N_{0.5}$ Derived Carbon

Argon sorption analysis was performed on $Ti_2AlC_{0.5}N_{0.5}$–CDC chlorinated at 600 °C. A hysteresis was measured in the isotherm, however, relatively little Ar was absorbed compared to the Ti_2AlC-CDC and Ti_3AlC_2-CDC, see Figure 4.29a. The pore size distribution shows a small amount of mesopores with the majority of the pore volume resulting from micropores less than 2 nm (Fig. 4.29b). The BET analysis suggests a specific surface area of 435 m^2/g. The DFT analysis measured a specific surface area of 390 m^2/g and a pore volume of 0.25 cc/g. This pore volume is extremely low compared to pore volumes measured from other MAX-phase carbides, as well as the Ta-based binary carbides.

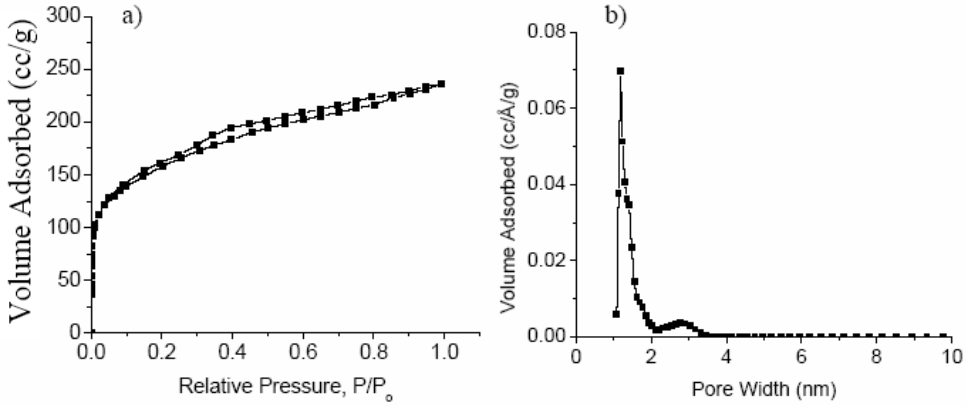

Figure 4.29 $Ti_2AlC_{0.5}N_{0.5}$-CDC Ar sorption analysis,a) isotherms of $Ti_2AlC_{0.5}N_{0.5}$-CDC chlorinated at 600 °C, b) DFT pore size distribution.

4.3.2 Deviation from Theoretical Pore Volume

The $Ti_2AlC_{0.5}N_{0.5}$-CDC is an extreme example of a deviation in measured pore volume compared to theoretical pore volume. As noted above, the $Ti_2AlC_{0.5}N_{0.5}$-CDC pore volume, as measured by NLDFT is 0.25 cc/g, the theoretical pore volume is 5.11 cc/g, see Table 3.4 assuming the transformation from carbide to carbon is conformal. Other CDCs also have a difference between theoretical pore volume and measured pore volume. Ti_2AlC-CDC, for example, has a theoretical pore volume of 2.33 cc/g, while the highest measured pore volume was 1.16 cc/g. Ti_3AlC_2-CDC had a theoretical pore volume of 1.47 cc/g, while the highest measured pore volume was 0.99 cc/g.

A difference in measured versus theoretical pore volume can be attributed to many factors, including closed porosity, blocked pores, pores too small for adsorbate to access, and pores too large for the Ar sorption analysis to measure. In the case of CDC, the only closed porosity that may exist should be a result of original porosity in the carbide, and is taken into account in the theoretical porosity if present. Blocked pores will exist in CDC mainly due to trapped metal chlorides formed during the chlorination

process. These metal chlorides cannot account for the difference in theoretical and measured pore volume for $Ti_2AlC_{0.5}N_{0.5}$-CDC. At chlorination temperatures of 1200 °C, less than 5 at% chlorine is present. This amount of chlorine is not sufficient to form enough metal chlorides to block almost 95% of the porosity in the case of $Ti_2AlC_{0.5}N_{0.5}$-CDC. The possibility that the difference stems from pores too small for the adsorbate also does not fit well with the results. If the difference was from pores too small for the adsorbate to access, then CDC produced from carbides with isotropic structures, like TaC, should have an increased difference between the theoretical and measured pore volume. This is not the case, however. The measured pore volume of TaC was actually higher than the theoretical pore volume. This difference in theoretical and experimental pore volume can be attributed to the loss of carbon atoms during the chlorination process through the formation of $CCl_{4(g)}$, $CO_{2(g)}$, and/or CO(g). It is reasonable to assume that the difference in theoretical and measured porosity in the case of $Ti_2AlC_{0.5}N_{0.5}$-CDC, and other CDCs produced from carbides with high theoretical porosities, results from pores too large for the Ar adsorption technique to measure. In the case of $Ti_2AlC_{0.5}N_{0.5}$-CDC significant cracking occurred, as shown previously in the SEM images, Figure 4.21. In addition to the large theoretical porosity, the layered structure of MAX-phase carbides, which is preserved in the resulting CDC is an ideal structure for promoting a collapse between the lamellar sheets of carbon, eventually forming large macro-cracks that can be seen without the aid of a microscope.

4.3.3 Effect of Carbide Chemistry on CDC Porosity

As described above, the accessible pore volumes of several carbides were measured using argon sorption technique. The initial carbide density was found to

influence the resulting CDC's pore volume. The carbide density relates to the average metallic atomic radius within the initial carbide. When removed by chlorination, larger metallic elements will form larger pores. The pore volumes of MAX-phase CDC and Ta-based binary carbides, along with additional binary carbide (SiC, TiC, and ZrC) pore volumes [88], can be seen in Figure 4.30a. Had the carbon structure of $Ti_2AlC_{0.5}N_{0.5}$-CDC not collapsed, it would probably have better fit the trend. Therefore, with the exceptions of CDC with extremely high theoretical porosity leading to a collapse in structure and CDC produced from carbides with unusually open structures, the trend of increasing initial carbide density and increasing micropore volume measured via Ar sorption is applicable.

DFT specific surface area was plotted as a function of carbide density as well, see Figure 4.30b. CDC produced from Ta containing carbides were found to have large specific surface areas. However, B_4C-CDC recorded the highest surface area based on Ar sorption measurements most likely due to its unique unit cell structure. CDC produced from Ti_2AlC and Ti_3AlC_2 yielded the smallest DFT surface areas based on Ar sorption measurements. When comparing CDC produced from carbides of similar structure, a conclusion from the DFT specific surface area results based on Ar sorption analysis can be made: increasing initial carbide density results in an increase in the specific surface area of the resulting CDC.

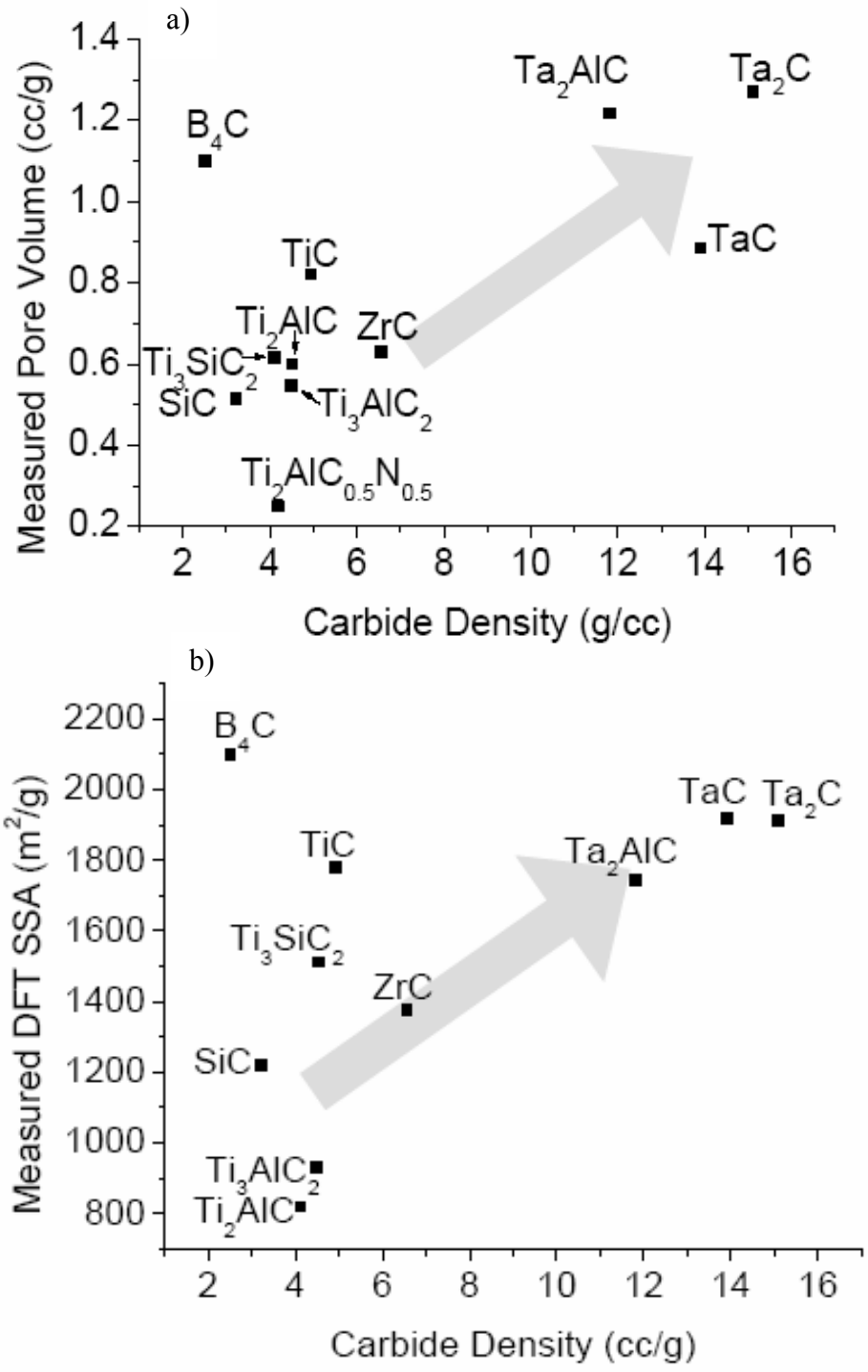

Figure 4.30 Porosity comparison of CDC produced from binary and ternary carbides, a) accessible pore volume, and, b) measured DFT specific surface area as a function of initial carbide density. Values for B_4C, SiC, ZrC, and TiC taken from reference [88].

4.3.4 Nitrogen Sorption

4.3.4.1 Ti_3AlC_2 Derived Carbon

N_2 sorption analysis was performed on Ti_3AlC_2-CDC chlorinated at 600, 800, and 1200 °C. The N_2 isotherms are given in Figure 4.31. The material chlorinated at 800 °C absorbed the most N_2, while also forming the largest hysteresis loop. Although the material chlorinated at 1200 °C formed a hysteresis loop, it was not as large as the one produced from the 800 °C material, nor did the material absorb as much N_2. The material produced at 600 °C followed the form of a Type I, rather than a Type IV, isotherm, with minimal hysteresis with the maximum amount of N_2 absorbed being under 600 cc/g. (Fig. 4.31) Using DFT analysis, the pore size distributions were determined, see Figure 4.32. The pore size distributions for Ti_3AlC_2-CDC chlorinated at 600 °C shows a narrow distribution with pores primarily below 5 nm (Figure 4.32a). The pore size distribution for Ti_3AlC_2-CDC chlorinated at 800 °C is broader, with significant pore volume of 0.5 cc/nm/g or greater up to 15 nm (Figure 4.32b). Measurable pore volume exists up to 35 nm, the limit of the N_2 sorption analysis kernel. The pore size distribution for Ti_3AlC_2-CDC chlorinated at 1200 °C shows a similar shape as the material chlorinated at 600 °C containing primarily pores less than 5 nm in width, (Figure 4.32c). However, the material chlorinated at 1200 °C has a significantly larger volume of pores under 5 nm compared to the material chlorinated at 600 °C.

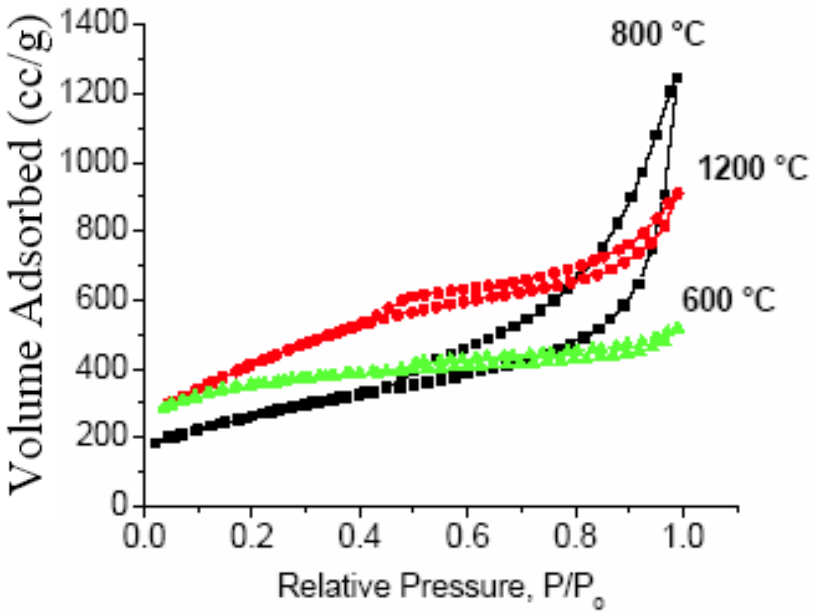

Figure 4.31 N_2 sorption isotherms for Ti_3AlC_2-CDC chlorinated at 600, 800, and 1200 °C.

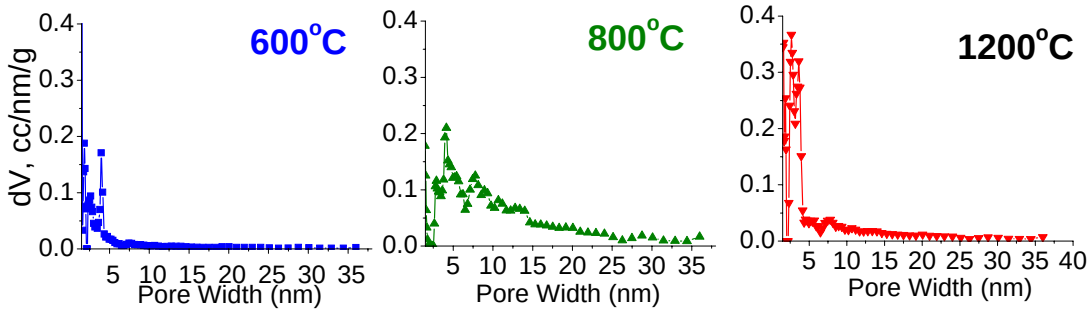

Figure 4.32 N_2 sorption DFT pore size distributions of Ti_3AlC_2-CDC chlorinated at a) 600 °C b) 800 °C c) 1200 °C

Based on the sorption results, Ti_3AlC_2-CDC chlorinated at 800 °C contains the largest amount of mesopores of the three temperatures, with a NLDFT pore volume of 1.70 cc/g. In comparison, the Ti_3AlC_2-CDC chlorinated at 600 °C contains a smaller pore volume of 0.70 cc/g. CDC chlorinated at 1200 °C results in a pore volume of 1.24, mainly attributed to large amounts of microporosity.

The large mesopore volume in Ti_3AlC_2-CDC chlorinated at 800 °C can be attributed to the structure of the carbon formed at this chlorination temperature. At 600 °C, the carbon structure is primarily amorphous, as was shown by the TEM and Raman spectroscopy, see Figures 4.11 and 4.16. At a chlorination temperature of 800 °C, the carbon structure starts to become more graphitic, with graphitic structures forming on the surface of the carbon particles. These thin graphitic ribbon structures are often bent or looping, creating pockets between adjacent graphitic structures and loops. These inter-graphitic structure spaces can also be considered pores. At a chlorination temperature of 1200 °C, carbon forms thick graphitic ribbons which are able to pack close together. In the space between the graphitic ribbon formations, amorphous carbon is present. Since the graphitic ribbons in the 1200 °C structure are thicker, they are less likely to form loops and sharp bends which presumably provide the additional mesopores. Therefore, the microporosity attributed to the material chlorinated at 1200 °C is primarily formed within the gently curved graphitic ribbons and patches of surrounding amorphous carbon.

4.3.4.2 Ti_2AlC Derived Carbon

N_2 sorption analysis was performed on Ti_2AlC-CDC chlorinated at 600, 800, and 1200 °C. The N_2 isotherms are given in Figure 4.33. Here again, the material chlorinated at 800 °C formed the largest hysteresis, similar to the results of Ti_3AlC_2-CDC. Both 800 °C and 1200 °C materials absorbed ~1700 cc/g for a maximum N_2 uptake. Ti_2AlC-CDC chlorinated at 600 °C resulted in an isotherm suggestive of a Type I isotherm with a small hysteresis and the lowest amount of N_2 uptake ~550 cc/g. DFT analysis was performed on the isotherms, see Figure 4.34. The results obtained paralleled that found for Ti_3AlC_2-CDC. The pore size distributions for Ti_2AlC-CDC chlorinated at

600 °C shows a narrow distribution with pores primarily below 5 nm, see Figure 4.34a. The pore size distribution for Ti_2AlC-CDC chlorinated at 800 °C depicts a broader distribution with significant pore volume of 0.5 cc/nm/g or greater up to 15 nm, see Figure 4.34b. Measurable pore volume exists up to 35 nm, the limit of the N_2 sorption analysis kernel. The pore size distribution for Ti_2AlC-CDC chlorinated at 1200 °C shows a similar shape as the material chlorinated at 600 °C containing primarily pores less than 5 nm in width, see Figure 4.34c. However, the material chlorinated at 1200 °C has significantly larger volume of pores less than 5 nm compared to the material chlorinated at 600 °C. The difference in pore volume between CDC chlorinated at 600 and 1200 °C occurs because of a difference in pore structure, recall as well as, presumably an increased number of blocked pores in the 600 °C material. CDC chlorinated at low temperatures have larger amounts of Cl impurities, which are capable of blocking pores and decreasing the measured pore volume.

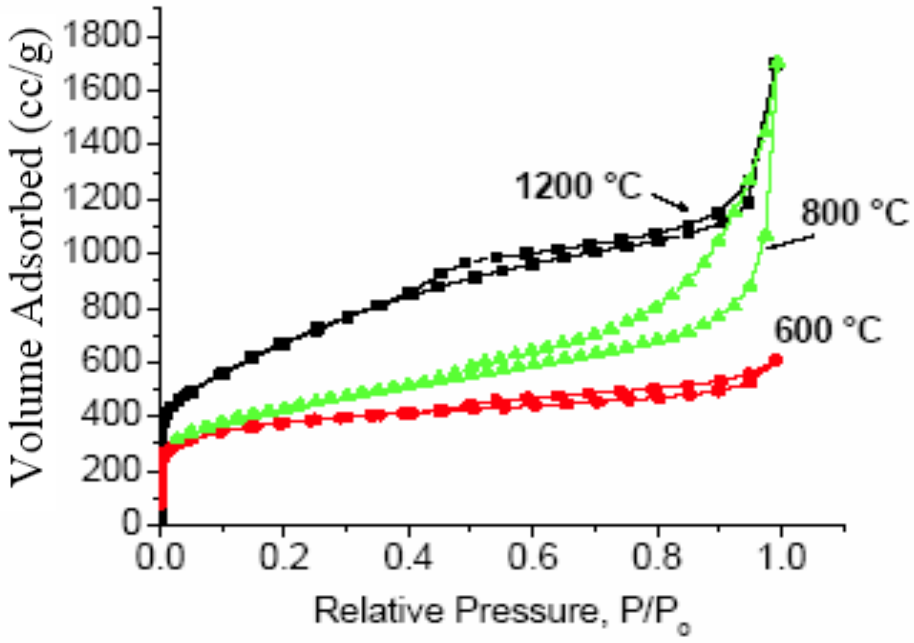

Figure 4.33 N_2 sorption isotherms for Ti_2AlC-CDC chlorinated at 600, 800, and 1200 °C.

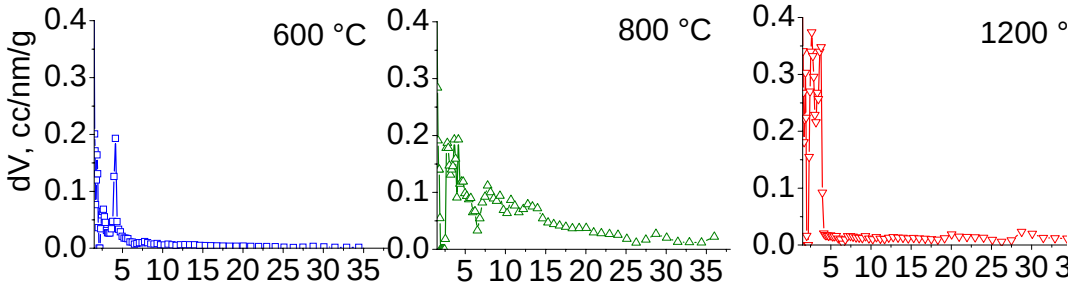

Figure 4.34 N_2 sorption DFT pore size distributions of Ti_2AlC-CDC chlorinated at, a) 600 °C, b) 800 °C, c) 1200 °C.

4.3.4.3 Comparison of CDC Chlorinated at 800 °C

Ti_3AlC_2-CDC and Ti_2AlC-CDC chlorinated at 800 °C resulted in large volumes of mesoporosity. N_2 sorption analysis was performed on Ti_3SiC_2-CDC, Ta_2AlC-CDC, Ta_2C-CDC, and TaC-CDC to compare the mesoporosity of various CDCs produced at 800 °C. The isotherms from the N_2 sorption are shown in Figure 4.35. Ti_2AlC-CDC and Ti_3AlC_2-CDC have the highest uptake of N_2 with over 1750 and 1250 cc/g, respectively. Both CDCs have a large hysteresis with a Type IV behavior. Ta_2AlC-CDC resulted in a hysteresis with a maximum N_2 uptake of ~750 cc/g. Ti_3SiC_2-CDC also resulted in a hysteresis with a maximum N_2 absorption ~550 cc/g. TaC-CDC and Ta_2C-CDC resulted in a Type I isotherm behavior, with a maximum N_2 absorption of 400 and 800 cc/g, respectively. The pore size distributions were determined using DFT analysis.

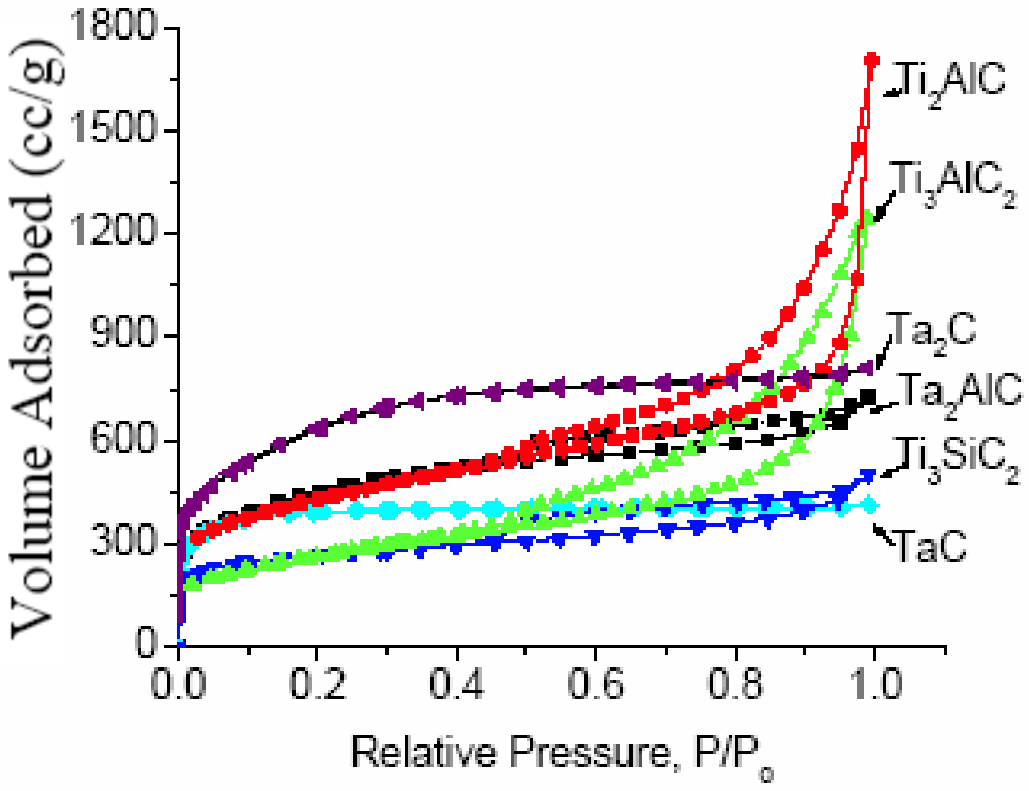

Figure 4.35 N_2 isotherms of CDC produced at 800 °C.

The pore size distribution for Ti_3SiC_2-CDC shows primarily micropores with a small amount of mesopores, see Figure 4.36a. The Ti_3AlC_2-CDC and Ti_2AlC-CDC produced pore size distributions with large quantities of mesopores, see Figure 4.36b and 4.36c. Ta_2AlC-CDC produced primarily micropores, with a small amount of mesopores up to 15 nm, see Figure 4.36d. Ta_2C-CDC and TaC resulted in pore size distributions of mostly micropores, see Figure 4.36e and f.

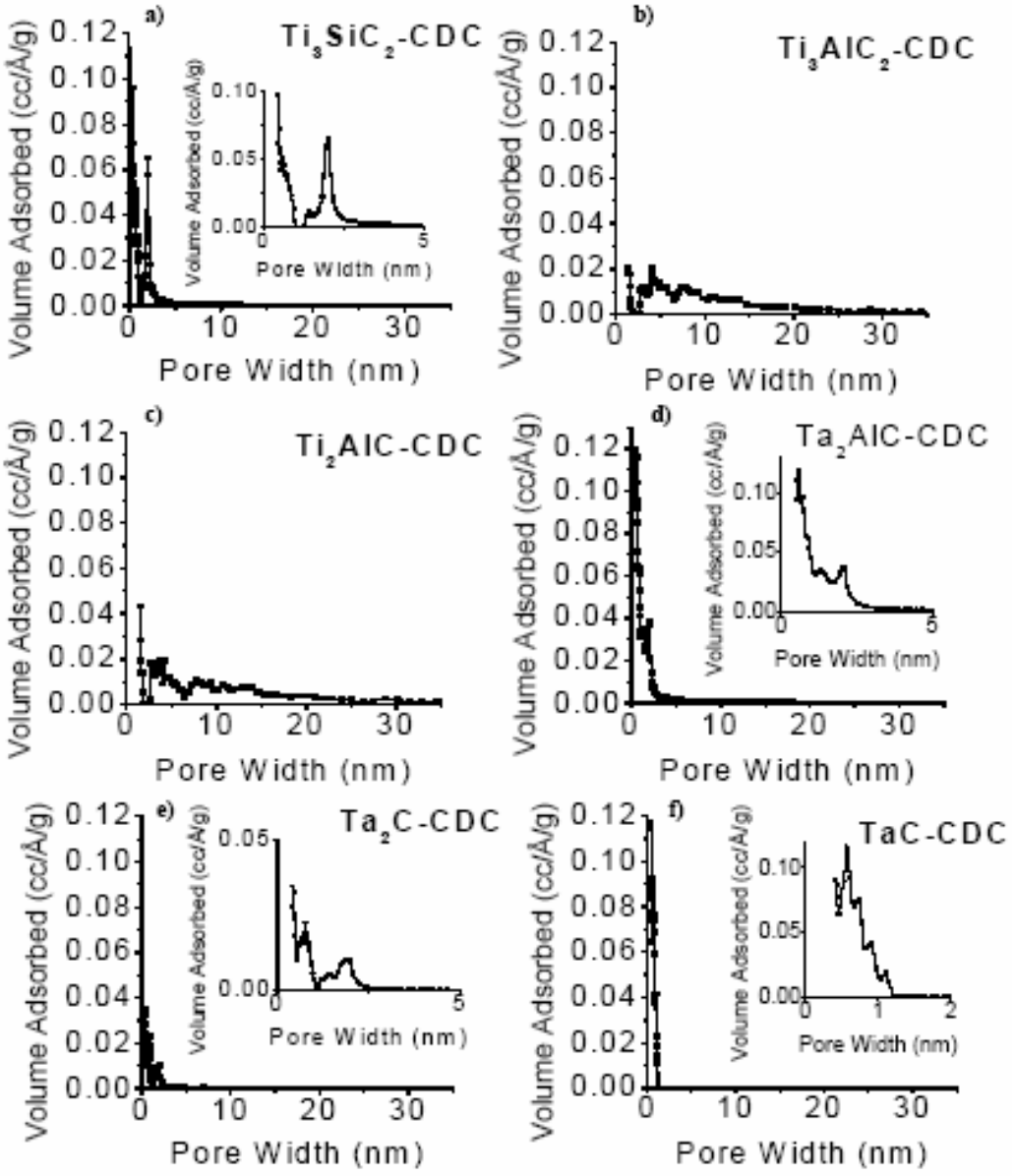

Figure 4.36 N_2 sorption DFT pore size distributions of CDC chlorinated at 800 °C, a) Ti_3SiC_2-CDC, b) Ti_3AlC_2-CDC, c) Ti_2AlC-CDC, d) Ta_2AlC-CDC, e) Ta_2C-CDC, f) TaC-CDC.

The difference in micropore volume, as described previously, is related to the precursor carbide density and chemistry. The Ar adsorption, when focusing on the pores less than 2 nm, follows the trend of increasing carbide density, increasing micropore volume. However, the mesopore volume does not follow the same relationship.

The layered MAX-phase derived carbides exhibited isotherms with an apparent hysteresis compared to the binary Ta-based carbides, and therefore suggest the presence of larger mesopore volumes. The difference is not due to only the chemistry of the carbides. Clearly, the structure of the initial carbides, is also important in addition to chemistry. TaC is an isotropic structure with carbon atoms evenly distributed throughout the unit cell. TaC-CDC resulted in primarily microporous carbon with relatively low N_2 adsorption. Ta_2C-CDC, also was primarily microporous with a Type I isotherm, however, it absorbed a larger quantity of N_2. The structure of Ta_2C, although not isotropic, is not layered like the MAX-phases having distinct carbon layers. Every MAX-phase carbide derived carbon tested formed varying levels of hysteresis. It is possible that the layered structure of MAX-phase carbides promote increased mesoporosity due to the ability to form contorting graphitic ribbons.

4.3.4.4 Comparison of Micro- and Meso-porosity

Comparing Ar and N_2 sorption aids in understanding the overall porosity of the material, having measured both micro and meso-porosity on a variety of CDC produced at 800 °C, and 600, 800, and 1200 °C chlorination temperatures for Ti_2AlC-CDC and Ti_3AlC_2-CDC. The pore volumes calculated from Ar and N_2 sorption are plotted in Figure 4.37 for Ti_3AlC_2-CDC and Ti_2AlC-CDC chlorinated at 600, 800, and 1200 °C. In both CDCs the amount of microporosity was around 0.5 cc/g for all chlorination temperatures, with material chlorinated at 800 °C having the lowest amount of microporosity in both cases. Both CDCs produced at 600 °C also had a similar volume of mesoporosity. However, both CDCs produced at 800 and 1200 °C had considerably more mesoporosity than microporosity, thereby significantly increasing the total pore

volume. The 800 °C chlorinated carbons have the largest amount of mesoporosity among all the chlorination temperatures.

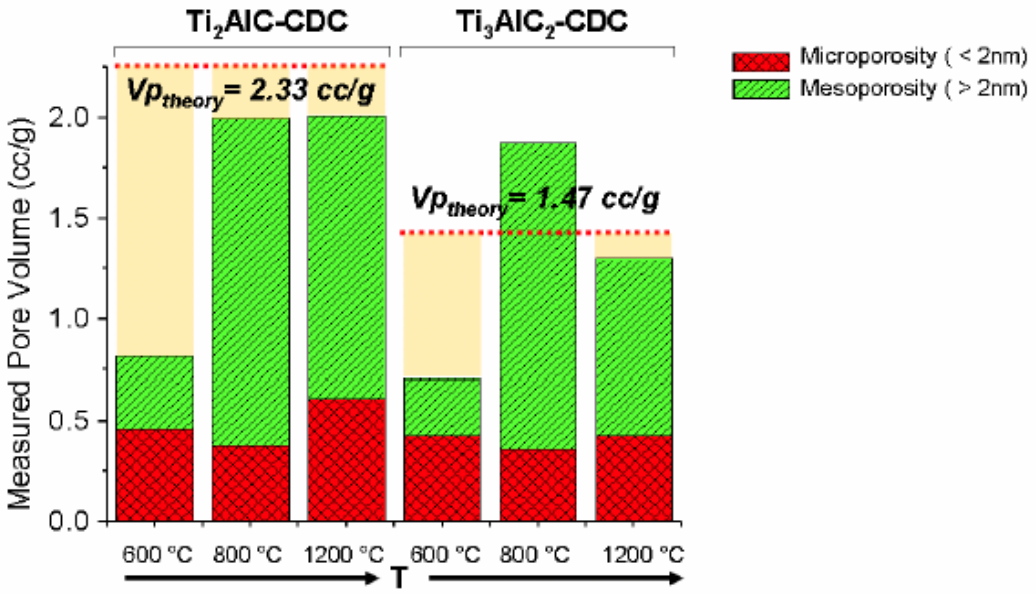

Figure 4.37 Comparison of micro-and mesoporosity of CDC produced from Ti_3AlC_2 and Ti_2AlC chlorinated at 600, 800, and 1200 °C. Also shown is the theoretical pore volume for each CDC based on a conformal transformation and that CDC has the density of graphite.

Figure 4.38 compares the micro- and mesoporosity to the total theoretical porosity of Ti_3AlC_2-CDC and Ti_2AlC-CDC to other CDC produced at 800 °C. It is obvious from the figure that the CDC, produced from Ti_3AlC_2 and Ti_2AlC have significantly larger mesopore volumes as compared to the others. The Ta-based CDCs, which include Ta_2AlC, Ta_2C and TaC, resulted in a larger amount of microporosity compared to the Ti-based carbides. This result is expected based on the relation between microporosity and initial carbide density (Fig. 30). TaC, with its isotropic carbide structure formed CDC with extremely small amounts of mesoporosity. This supports the concept that the initial carbide structure influences the amount of mesoporosity produced by the material.

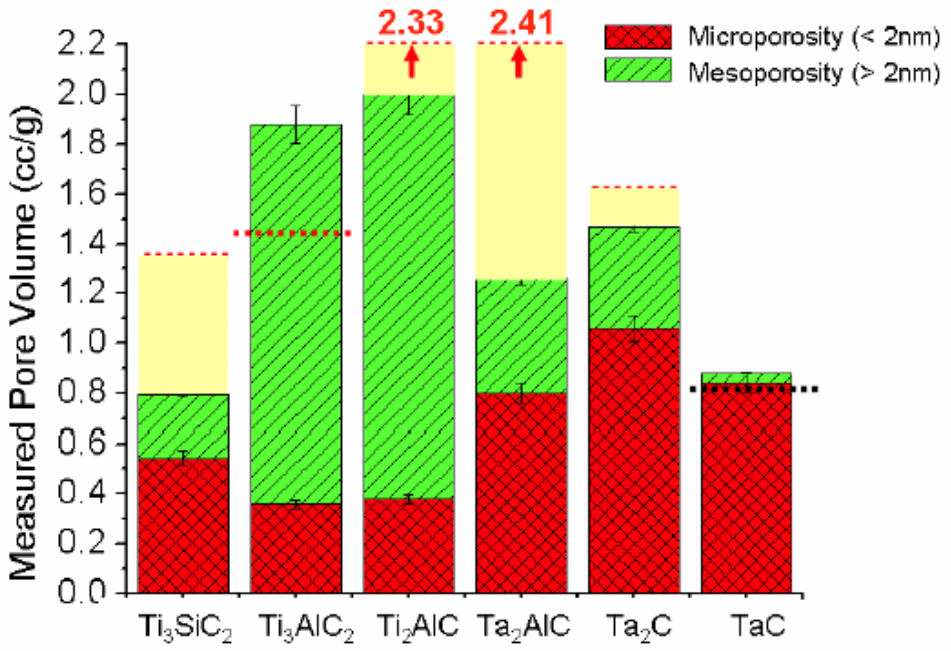

Figure 4.38 Comparison of micro- and mesoporosity for CDCs produced at 800 °C from different precursors.

The micro- and mesoporosity of $Ti_2AlC_{0.5}N_{0.5}$-CDC chlorinated at 600 °C was also compared to those of Ti_3AlC_2-CDC and Ti_2AlC-CDC, see Figure 4.39. The sample contained 0.16 cc/g of microporosity, while surprisingly, only 0.08 cc/g of mesoporosity. Clearly the collapse of the structure in this case does not favor the formation of mesopores in the 2-35 nm range of detectable by N_2 adsorption. The pore widths of the collapsed regions must, therefore, be larger than 35 nm.

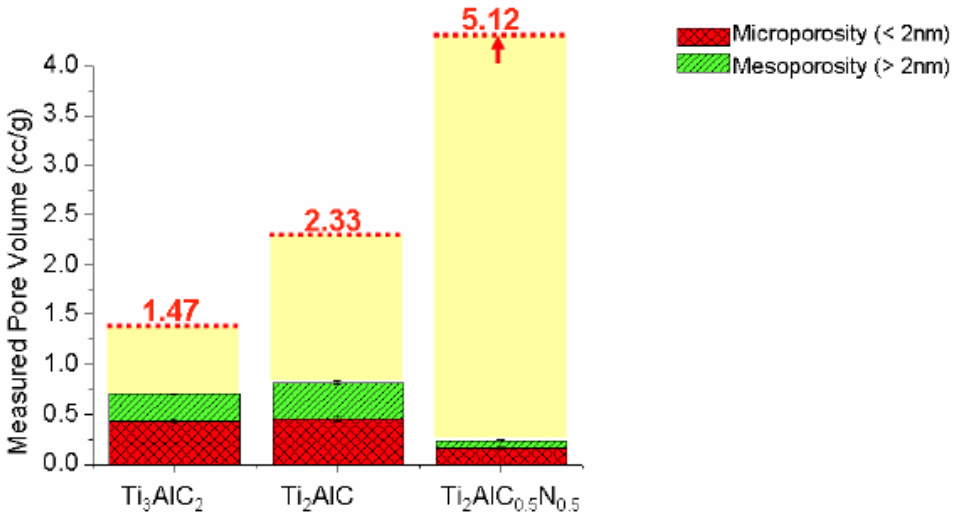

Figure 4.39 Comparison of micro- and mesoporosity of Ti_3AlC_2-CDC, Ti_2AlC-CDC, and $Ti_2AlC_{0.5}N_{0.5}$-CDC produced at 600 °C.

Note, the error bars present in Figures 4.37, 4.38, and 4.39 represent the error associated with the isotherm measurement and do not include the error associated with the assumptions made in the NLDFT model or variations between powder chlorination batches. For example, the NLDFT model assumes that the carbon is homogeneous and contains slit pores. In reality, CDC most likely contains slit, cylindrical, and spherical shaped pores. In particular, the CDC produced at low chlorination temperatures of 600 °C will have more cylindrical and spherical shaped pores compared to CDC chlorinated at 1200 °C. Therefore, the error from the NLDFT assumption on the shape of the pores will vary with temperature with the largest errors in the analysis of CDC occurring in material with highest volumes of micropores due to the deviation of the actual pore shape from slit pores. The potential of interaction between the adsorbate gas and the carbon surface will be the highest for spherical pores and the lowest for slit shaped pores due to the interaction distance between the adsorbate gas and the carbon surface. It should be realized that when using the slit shaped pore model, the NLDFT analysis will result in

smaller pores compared to the cylindrical pore model. Therefore, the NLDFT pore size distribution of material produced at low chlorination temperatures may suggest a larger number of smaller pores than what really exists within the material. Mesopores, which are not as influenced by the potential of interaction of the adsorbate and carbon surface compared to micropores, will not depend as much on pore shape assumptions.

To illustrate the influence of pore shape assumptions in the NLDFT model, Ti_2AlC-CDC chlorinated at 600, 800, and 1200 °C were analyzed using the NLDFT kernel based on slit shaped and cylindrical pores. Table 4.1 indicates that the heavily mesoporous material chlorinated at 800 °C does vary as much as the microporous 600 and 1200 °C materials when the pore shape assumption is changed. The specific surface area for all three materials varied more than the pore volume, which is a result of the surface area calculations relying on the pore shape assumptions more so than the pore volume calculations.

Table 4.1 Comparison of NLDFT pore volume and specific surface area in Ti_2AlC-CDC chlorinated at 600, 800, and 1200 °C based on assumptions of pore shape.

Chlorination Temperature	**600 °C Slit/Cylindrical**	**800 °C Slit/Cylindrical**	**1200 °C Slit/Cylindrical**
NLDFT Pore Volume (cc/g)	0.70/0.74	2.0/2.0	2.0/2.0
NLDFT Specific Surface Area (m^2/g)	930/1450	1170/1500	1850/2410

In addition to errors from pore shape assumptions, errors in measured pore volume and specific surface area occur due to the reliance of the calculations based on model pores in the NLDFT model. Dips in the NLDFT pore size distribution occur, which are not real but are artifacts of the NLDFT model, for an example see Figure 4.23b. Since NLDFT pore volume and specific surface area are calculated through the

same models used to determine the pore size distribution, errors in pore volume and specific surface area will occur resulting in calculated values that are less than the true values due to the dips in the pore size distribution resulting from artifacts in the NLDFT model.

4.3.4.5 Total Measured Pore Volume versus Theoretical Pore Volume

Most of the total measured pore volumes reported in Figures 4.37, 4.38 and 4.39 do not match the theoretical pore volume. In the case of Ti_3AlC_2-CDC and Ti_2AlC-CDC chlorinated at 600 °C (Fig. 4.37) the measured total pore volumes of 0.75 cc/g and 0.80 cc/g, are significantly lower than the theoretical pore volumes of 1.47 and 2.33 cc/g, respectively. This difference in pore volume is most likely due to pores blocked by residual metal chlorides which remained in the CDC after chlorination. The presence of residual Ti and Cl confirmed by EDS supports this notion. Ti_2AlC-CDC chlorinated at 800 and 1200 °C, Figure 4.37, resulted in the measured total pore volumes slightly lower than the theoretical pore volumes. This again may be in part, a result of metal chloride blocked pores. Also, pores may exist that are either too small or too large for the adsorption technique to measure. At the chlorination temperature of 1200 °C, Ti_3AlC_2-CDC resulted in a measured total pore volume about equal to the theoretical pore volume. In the case of Ti_3AlC_2-CDC chlorinated at 800 °C, the measured total pore volume of 1.8 cc/g, is higher than the theoretical pore volume of 1.47 cc/g. The presence of a larger pore volume may stem from the formation of $CCl_{4(g)}$, $CO_{(g)}$, or $CO_{2(g)}$. However, the formation of these gases is not believed to be considerable according to thermodynamic simulations, see Figure 4.2. Therefore, in addition to carbon containing gas formation, another factor most likely is involved in the increased pore volume. At the temperature

of 800 °C, Ti_3AlC_2-CDC forms the graphitic ribbons, which often form loops which can be considered mesoporosity. The loops can contribute to mesoporosity due to their large size compared to the microporosity formed within other CDCs. The result of graphitic ribbon loops could increase the pore volume due to the carbon particles bulging in a sense can be applied to any CDC that forms graphitic ribbons that are sharply bent or contorted.

Ti_3SiC_2-CDC, Ti_2AlC-CDC, and Ta_2AlC-CDC, all have shown graphitic ribbons in TEM images at chlorination temperatures of 800 °C, see Figures 4.16b, 4.17b, and 4.18b. These materials, however, had measured total pore volumes that were lower than theoretical, see Figure 4.38. Several factors influence the measured total pore volume, such as blocked pores, pores too small to measure, pore too large to measure, formation of carbon containing compounds during chlorination, and the bulging effect described above. It is the sum of these factors that lead to the measured pore volume. The Ti_3SiC_2-CDC, Ti_2AlC-CDC, and Ta_2AlC-CDC samples were influenced to a greater extent by factors that lower the total pore volume, as compared to Ti_3AlC_2-CDC.

4.4 H_2 Annealing

To increase the pore volume in CDC containing pores blocked by chlorine, H_2 annealing was performed.

Energy Dispersive Spectroscopy

Ti_3SiC_2-CDC chlorinated at 600 °C was split into a series of samples that were H_2 annealed for 5 h at 200, 400, 600, 800, and 1200 °C. The amount of chlorine and residual metals was measured by EDS, see Table 4.2. Minimal amounts of Ti and Si were measured using EDS. This suggests that the primary source of Cl is from Cl_2 or Cl

physisorbed to the surface of the carbon, rather than in the form of a metal chloride. The amount of oxygen slightly increased with increasing H_2 annealing temperature. This trend is probably due to the susceptibility for carbon to react with oxygen at elevated temperatures during chlorination. The amount of Cl present in the CDC decreased dramatically, even at H_2 annealing temperatures as low as 200 °C. Complete removal of chlorine occurred at a H_2 annealing temperature of 800 °C over 5 h. Interestingly, the amount of residual Si was not affected by H_2 annealing.

Table 4.2 EDS data of Ti_3SiC_2-CDC chlorinated at 600 °C and H_2 annealed at temperature ranging from 200-1200 °C for 5 h.

Annealing Temperature	Cl (at%)	Ti (at%)	Si (at%)	C(at%)	O (at%)
None	10.6	< 0.1	0.2	87.2	2.0
200 °C	2.9	< 0.1	0.2	89.3	7.5
400 °C	0.5	< 0.1	0.2	89.2	10.0
600 °C	0.3	< 0.1	0.3	88.6	10.8
800 °C	<0.1	< 0.1	0.3	91.4	8.4
1200 °C	0.0	< 0.1	0.2	89.3	10.5

In a separate study, the influence of the H_2 annealing temperature relative to the synthesis temperature was determined by H_2 annealing Ti_3SiC_2-CDC chlorinated at 400 and 800 °C at annealing temperatures of 400 and 1000 °C for 5 h. The amount of chlorine and residual metals was measured by EDS, see Table 4.3.

Table 4.3 EDS of Ti_3SiC_2-CDC chlorinated at 400 and 800 °C and H_2 annealed at 400 and 1000 °C for 5 h.

Synthesis Temperature	Annealing Temperature	Cl (at%)	Ti (at%)	Si (at%)	C(at%)	O(at%)
400 °C	None	2.9	0.1	0.2	88.9	7.8
400 °C	400 °C	1.7	< 0.1	0.2	88.4	9.5
400 °C	1000 °C	0.0	< 0.1	0.2	89.5	10.3
800 °C	None	1.8	< 0.1	0.3	90.0	7.9
800 °C	400 °C	<0.1	< 0.1	0.2	91.4	8.2
800 °C	1000 °C	0.0	< 0.1	0.2	89.8	10.0

Prior to H_2 annealing, the amount of chlorine in the 400 °C sample was more than the 800 °C material. This confirms the results from EDS of Ti_3SiC_2-CDC, Figure 4.22, in which materials produced at low chlorination temperatures result in larger amounts of residual chlorine. After H_2 annealing at 400 °C, the chlorine amount drops, while the amount of residual Si remains the same. A minimal amount of Ti existed within the as produced sample, so it is difficult to determine whether H_2 annealing would have an influence on Ti concentration. Most likely, Ti would respond similar to Si during the H_2 annealing process. At H_2 annealing temperatures of 1000 °C, an increase in oxygen content occurs, as well as a further reduction in Cl concentration.

To determine the time required to purify CDC through H_2 annealing, Ti_3SiC_2-CDC was chlorinated at a moderate temperature of 600 °C and H_2 annealed at the same temperature to prevent complications due to carbon structure changes from annealing at a different temperature, see Figure 4.40. It was determined that at 600 °C a chlorination time of ~15 h was sufficient to completely remove Cl from Ti_3SiC_2-CDC.

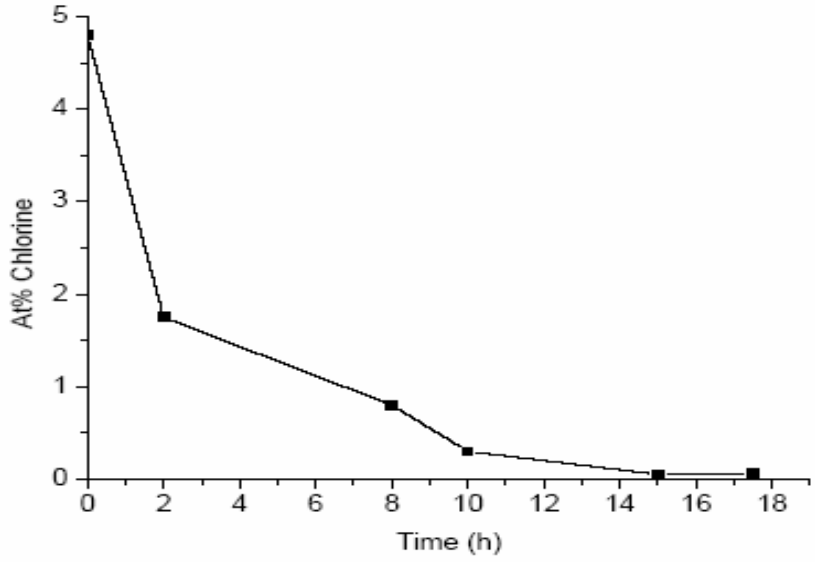

Figure 4.40 Atomic percentage of Cl in Ti_3SiC_2-CDC chlorinated at 600 °C and H_2 annealed at 600 °C at varying times as determined by EDS.

When revisiting the initial Ti_3SiC_2-CDC chlorinated at 600 °C with no H_2 annealing, it was found that the Cl level dropped to 1.25 at% over a period of 8 months. Therefore, the Cl_2 is most likely emitted from the CDC over time and replaced with moisture and/or $CO_{2(g)}$ from the atmosphere. The influence of time on the amount of Cl present in CDC also explains the variations in Cl content from one experimental set to the next. While Cl can be partially removed over time in ambient conditions, the H_2 annealing accelerates the process.

Raman Microspectroscopy

To determine if a change in structure occurs within CDC after H_2 annealing is performed at temperatures greater than the chlorination temperature, Ti_3SiC_2-CDC chlorinated at 400 °C was H_2 annealed at 400 and 1000 °C for 5 h. Raman spectra were compared between the non-H_2 annealed, 400, and 1000 °C samples, see Figure 4.41. The FWHM of the D- and G-bands were found to be 212 and 108 cm^{-1} prior to H_2 annealing. After annealing at 400 °C, the D-band decreased slightly to 200 cm^{-1}, followed by a further decrease to 187 cm^{-1} at a H_2 annealing temperature of 1000 °C. The G-band remained around 110 cm^{-1} after both annealing processes. The Raman results suggest that the carbon structure underwent graphitization during the H_2 annealing treatment, even at the low annealing temperatures of 400 °C. The increased graphitization at a low temperature of 400 °C results from the increased time at elevated temperatures with the H_2 annealing time of 5 h, compared to the chlorination time of 3 h. Further graphitization occurred at the 1000 °C H_2 annealing temperature.

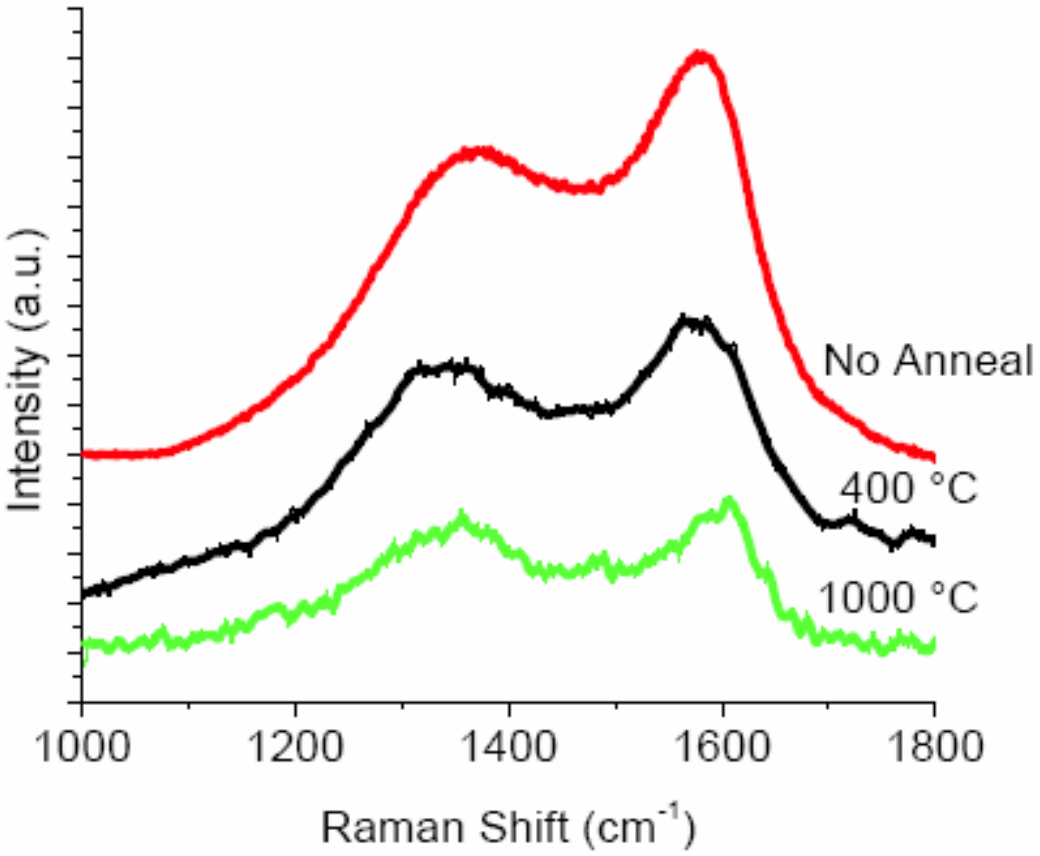

Figure 4.41 Raman spectroscopy of Ti_3SiC_2-CDC chlorinated at 400 °C as prepared, H_2 annealed at 400 °C, and H_2 annealed at 1000 °C.

Ar Sorption Analysis

Ar sorption analysis was performed on both Ti_3SiC_2-CDC chlorinated at 600 °C and H_2 annealed at 200, 400, 600, 800, and 1200 °C, as well as Ti_3SiC_2-CDC chlorinated at 400 and 800 °C, and H_2 annealed at 400 and 1000 °C. From DFT analysis, an increase in pore volume occurred with H_2 annealing, see Table 4.4. The pore volume increase is attributed to the removal of $Cl_{2(g)}$ during H_2 annealing, particularly at temperatures greater than 800 °C.

Table 4.4 Pore Volume and Specific Surface Area of Ti_3SiC_2-CDC chlorinated at 600 °C and H_2 annealed at various temperatures for 5 h.

	Pore Volume (cc/g)	BET SSA (m^2/g)
No H_2 Anneal	0.60	1380
H_2 Anneal 200 °C	0.73	1830
H_2 Anneal 400 °C	0.73	1700
H_2 Anneal 600 °C	0.73	1750
H_2 Anneal 800 °C	0.84	1910
H_2 Anneal 1200 °C	1.00	2150

Despite the increase in pore volume from 0.6 to 1.00 cc/g, the total theoretical pore volume of 1.47 cc/g was not achieved. Therefore, the difference between theoretical and measured Ar sorption porosity cannot be solely due to Cl containing impurities, but other factors must play a role. Reasons for the measured Ar sorption porosity to be lower than the theoretical porosity include the presence of pores or cracks greater than 7 nm in diameter, pores that are too small for Ar to enter, pores that evolved into close pores once the metal chlorides left the carbon, deviations from assumptions in NLDFT method including pore shape variations, and the assumption of the sample after chlorination having the density of graphitic carbon, which CDC may not have when heavy metals are present in the carbon material resulting in a measured pore volume being less than the actual pore volume. In the case of Ti_3SiC_2-CDC, Si is not completely removed despite H_2 annealing. The presence of Si, even of ~0.2 at% can increase the density of the CDC, causing an error in the measured pore volume of the CDC, resulting in a measured pore volume that is less than the actual pore volume.

H_2 annealing does not increase the measured pore volume of materials chlorinated at temperatures associated with the presence of minimal Cl impurities. The pore volumes of Ti_3SiC_2-CDC chlorinated at 400 and 800 °C and H_2 annealed at 400 and 1000 °C were

measured using Ar sorption analysis. The EDS analysis for the materials is given in Table 4.2. The H_2 annealing treatment provided a significant increase in pore volume and surface area for the CDC chlorinated at 400 °C then H_2 annealed at 1000 °C, see Figure 4.42. The pore volume increased from 0.42 cc/g, for the material chlorinated at 400 °C with no H_2 treatment, to 0.64 cc/g after 5 h of H_2 annealing at 1000 °C. The NLDFT specific surface area also increased from 1120 to 1590 cc/g upon H_2 annealing. However, the material chlorinated at 800 °C with no H_2 treatment did not increase in measured pore volume after the H_2 annealing treatment at 1000 °C. The pore volume changed from 0.76 to 0.79 cc/g upon H_2 annealing. This difference is a small change, and is within the error of the sorption measurement and NLDFT method.

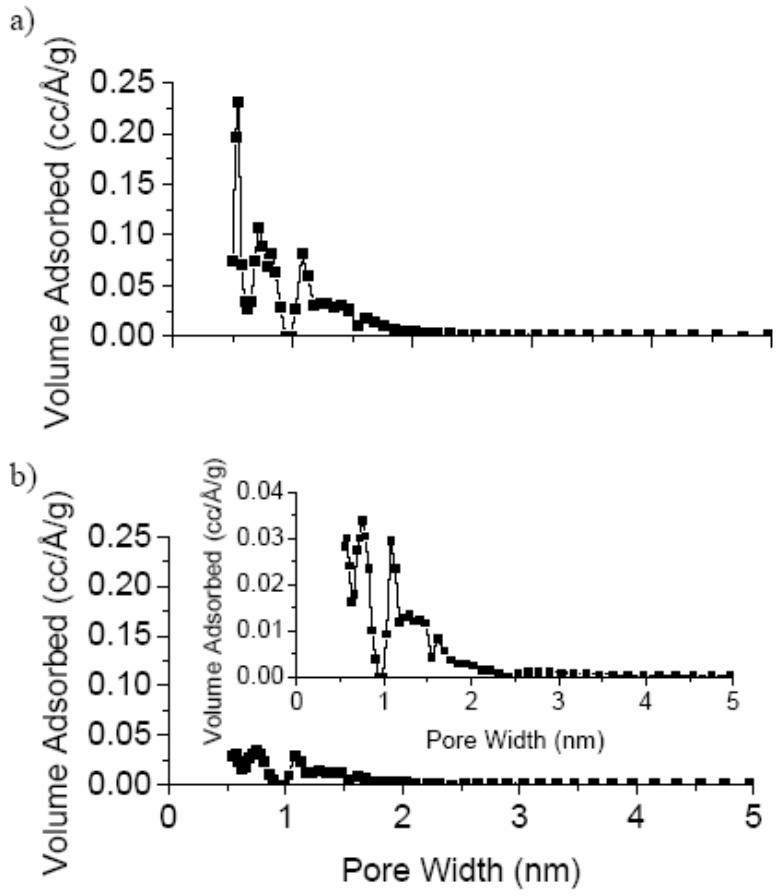

Figure 4.42 Pore size distribution from Ar sorption results of Ti_3SiC_2-CDC chlorinated at 400 °C, a) H_2 annealed at 1000 °C for 5 h, b) no H_2 anneal.

4.5 Membrane Synthesis

To broaden the potential applications for CDC to be used beyond powders, whiskers, and thin films on dense carbides, a CDC membrane was developed. The tunable specific surface area and pore volume associated with CDCs would be beneficial if they could be used in membrane form. Due to the microporosity of CDC, the membrane needs to be thin to prevent the need of excessive pressure to push a mixture through the membrane, and potentially breaking the membrane in the process. Several attempts at membrane development were made, see Appendix A. Formation of a multiplayer membrane with a thin CDC active layer deposited on a porous substrate via magnetron sputtering was successful. The three stages of CDC membrane synthesis are shown in Figure 4.43. Upon chlorination, the sputtered membrane undergoes a visual change from metallic grey to black.

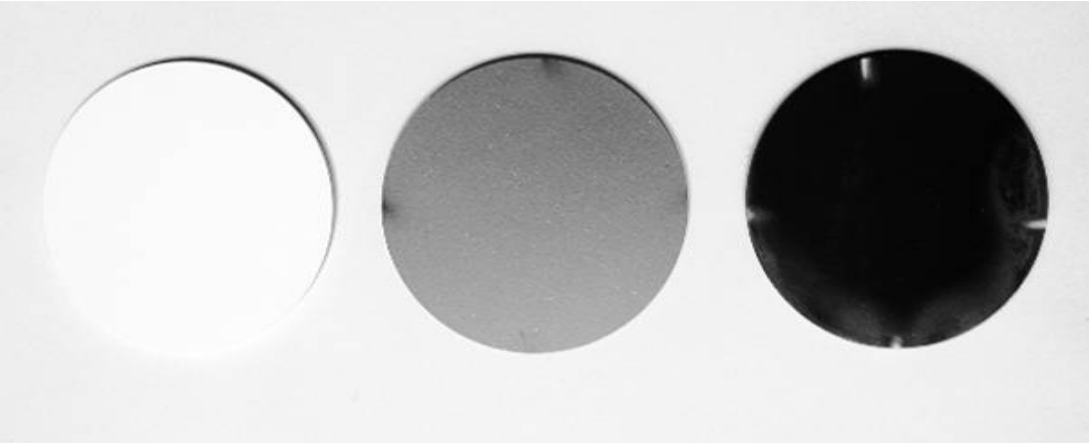

Figure 4.43 Stages of membrane synthesis, 1) Ceramic support, 2) Carbide sputtered layer, 3) Chlorinated CDC membrane. In this case, the ceramic support was 47M014 by Sterlitech Corporation and the TiC was the carbide.

The 47M014 and Anodisc 25 substrates used were observed in a scanning electron microscope to determine the average pore size on the surface of the substrate. The pore size was slightly different from one side compared to the flip side for both

supports. Observing a fractured cross-sectional surface of a 47M014 ceramic membrane using a scanning electron microscope, porous bilayers can be seen, see Figure 4.44. 47M014 is composed of alumina with a thin layer of finely porous titania. SEM determined the porosity of the Anodisc 25 to be 50 nm on the shiny side, compared to 200 nm on the matte side, see Figure 4.45. EDS determined the Anodisc 25 substrate primarily is composed of alumina with <2 at% phosphorous impurity, see Table 4.5

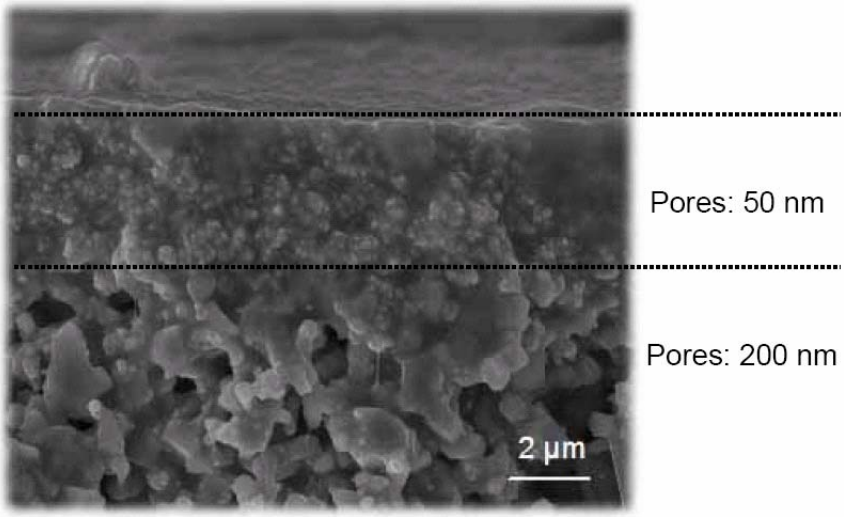

Figure 4.44 Cross section of Sterlitech membrane showing varying porosity.

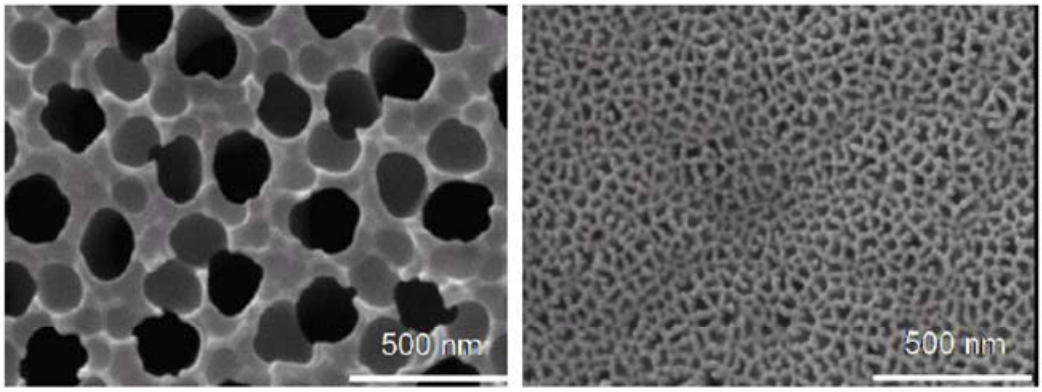

Figure 4.45 Porosity of Anodisc 2 membrane by Whatman on matt (left) and shiny (right) side.

Table 4.5 EDS analysis of during three stages of carbon membrane synthesis.

Element	Anodisc (At%)	TiC (At%)	TiC-CDC (At%)
C	4	50	40
Al	33	26	29
O	60	12	28
Ti	0	12	<1
Cl	0	0	2
P	2	1	1

The sputtered TiC thin film formed a rough, yet continuous, layer over the porous Anodisc 25 with occasional TiC spheres on the surface, see Figure 4.46. The thickness of the TiC layer was 500 nm as determined by electron microscopy, Figure 4.46. The non-stoichiometric ratio of Ti to carbon is due to sputtering effects. The high carbon content in the TiC coating is a result of one or a combination of occurances during the sputtering process. The carbon content can be off stoichiometry due to the simultaneous magnetron discharge in the four magnetrons, which are never precisely the same under the same Ar and C_2H_2 partial pressures. Furthermore, part of the ethylene might have decomposed due to the plasma discharge in the atmosphere containing more than 50 vol. % of C_2H_2 into hydrogen and carbon atoms, with the carbon atoms condensing in the form of the soot on the surface of the disks. A small amount of carbon condensation would have a strong affect on the overall carbon content of the coatings. This effect is most likely what happened during the sputtering process.

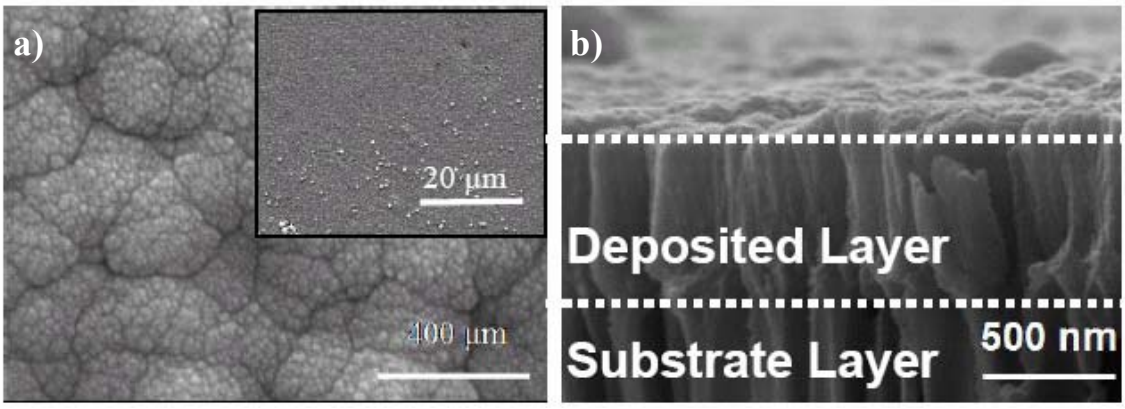

Figure 4.46 TiC sputtered coating, a) top view of coating show, inset, spheres of TiC speckle the surface, b) cross-sectional view showing a rough, yet continuous ~500 nm thick coating.

After chlorination, the discs visibly changed color from a metallic gray to black. As determined by EDS, see Table 4.4, the majority of Ti was etched away, with <1 at% Ti remaining, while SEM images shows the layer remains continuous without apparent cracks or voids, Figure 4.47. The TiC-CDC cross-section appears to be crack-free and void of delamination, Figure 4.47. Furthermore, the cross-section does not appear to have changed in thickness due to chlorination, see Figure 4.47.

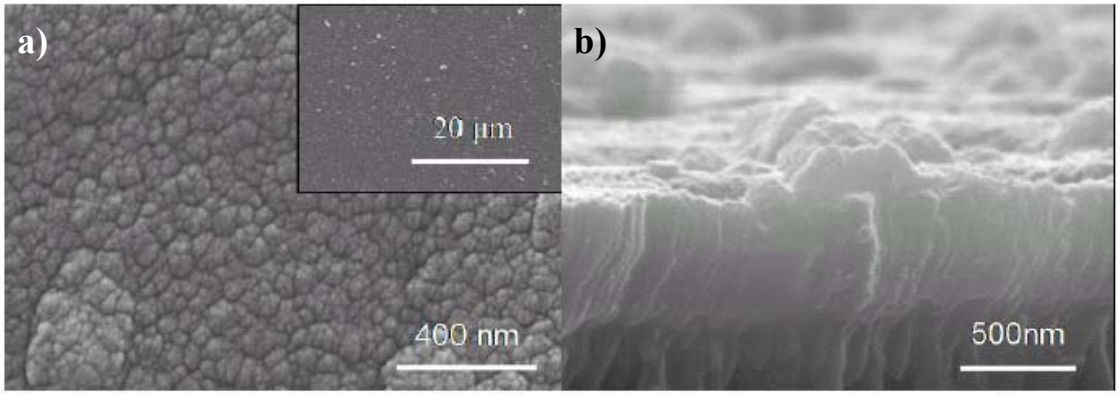

Figure 4.47 TiC-CDC active layer, a) top view of coating, insert, spheres of carbon speckle the surface, b) cross-sectional view showing rough, yet continuous, surface remains after chlorination.

Raman spectroscopy performed on the TiC coated Anodisc 25 prior to chlorination showed weak D- and G-band peaks, located at 1360 and 1580 cm^{-1},

respectively. After chlorination, strong D- and G-band peaks were present, Figure 4.48. The strong presence of D and G-band peaks confirm the visual color change, confirming the transformation from carbide to carbon had occurred. To compare the structure found by TEM of the TiC sputtered layer versus TiC powder, TiC powder was chlorinated at 350 °C. The structure of CDC produced as a powder and as a membrane from TiC at 350 °C were similar.

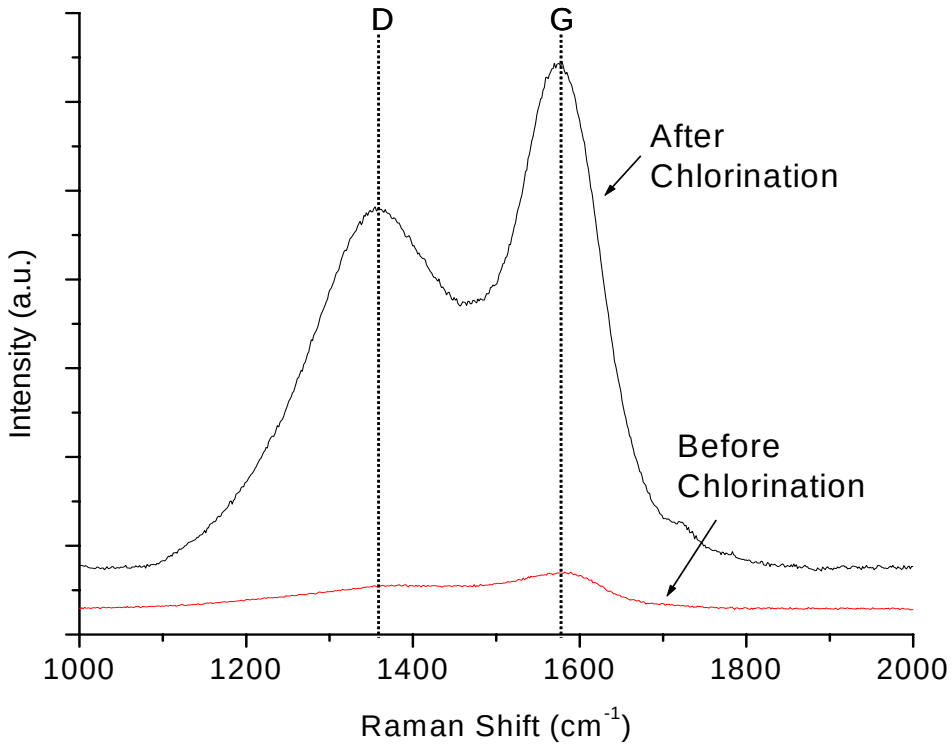

Figure 4.48 Raman microspectroscopy of TiC sputtered layer before chlorination and carbon membrane layer after chlorination.

The Raman results (Fig. 4.48) are from the case of TiC coated on Anodisc 25 membrane. A parallel study to monitor the stages of membrane development was done for the 47M014 membrane. The results obtained were similar.

To determine if the multi-layer membrane with CDC as the active layer is truly a membrane capable of allowing molecules to permeate, a gas permeation experiment was performed. Since the 47M014 supported membrane was more robust than the Anodisc 25 membrane, and pressures were needed to drive gases through the membrane, the 47M014 supported membrane was selected as the system to use.

A difference in gas permeation exists between a 47M014 membrane as received (Figure 4.49) and a 47M014 membrane chlorinated at 400 °C with no carbide or carbon coating (Figure 4.50). Compared to an as received 47M014 membrane, the gas pressure dropped much quicker over time through the chlorinated 47M014 membrane for argon, helium, and nitrogen. The difference in time required for the gases to permeate is most probably due to an etching effect of the titania and alumina within the membrane during chlorination.

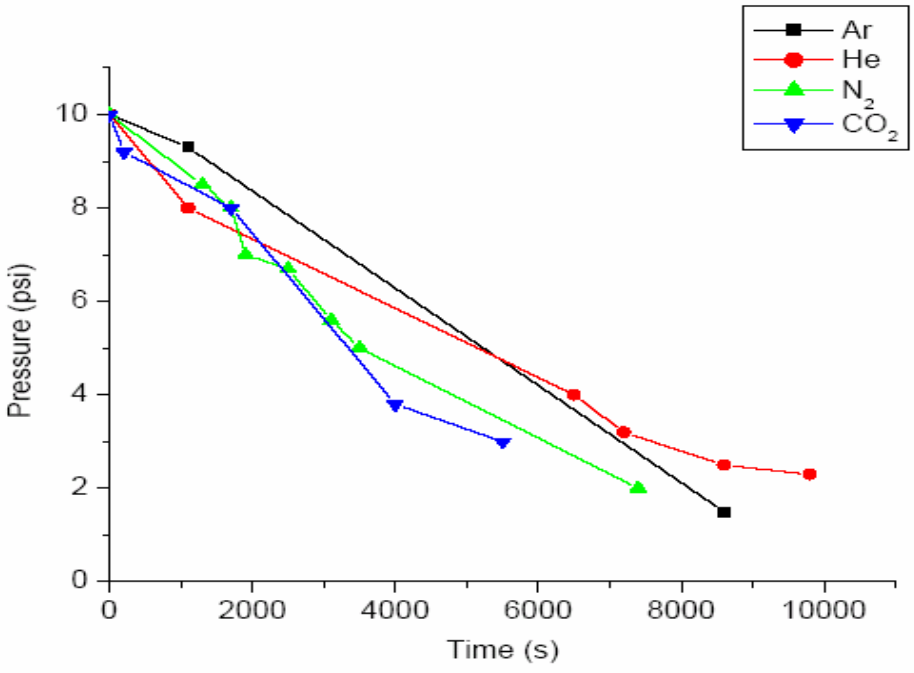

Figure 4.49 Pressure drop versus time for a constant volume of gas through an as-received ceramic membrane.

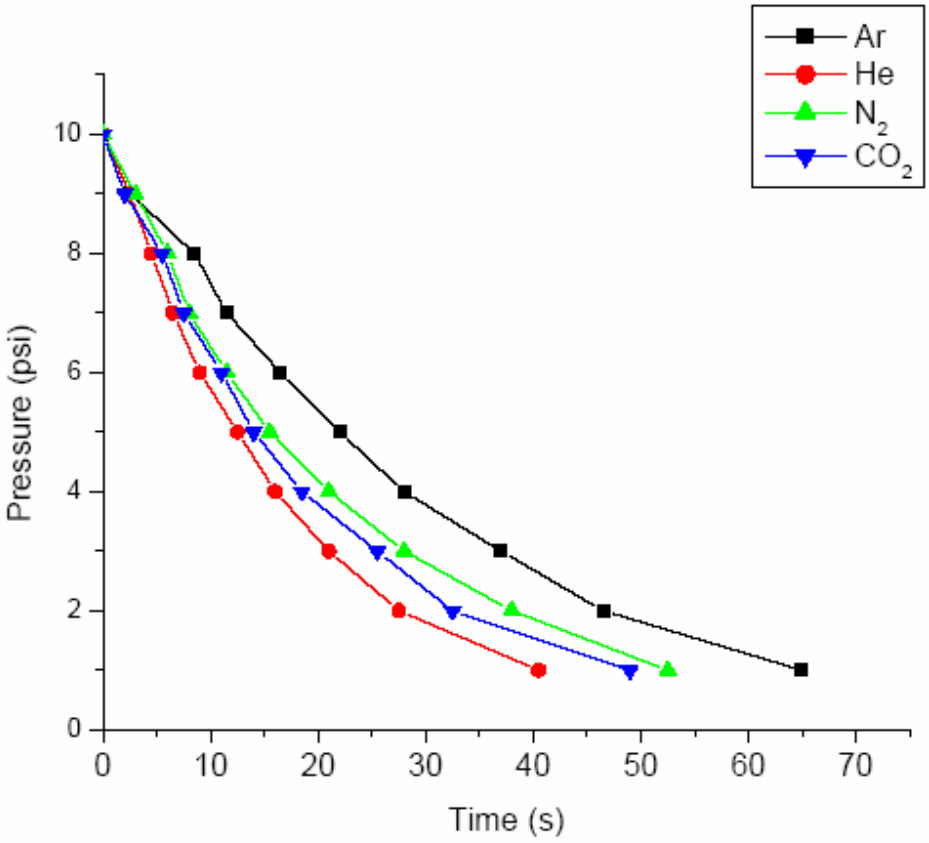

Figure 4.50 Pressure drop versus time of a constant volume of gas through ceramic membrane chlorinated at 350 °C.

Comparing to the gas pressure drop over time for the carbon/47M014 membrane system to the chlorinated 47M014, the order of the gas permeation is the same. However, the time required for permeation increases by approximately twice when the porous carbon layer is present, see Figure 4.51. This result suggests that gases can penetrate through the membrane, while at the same time the carbon layer has an effect on gas permeation. In principle then, multiple gases can permeate the multi-layer composite

membrane, thereby proving the carbon layer is capable of permeation.

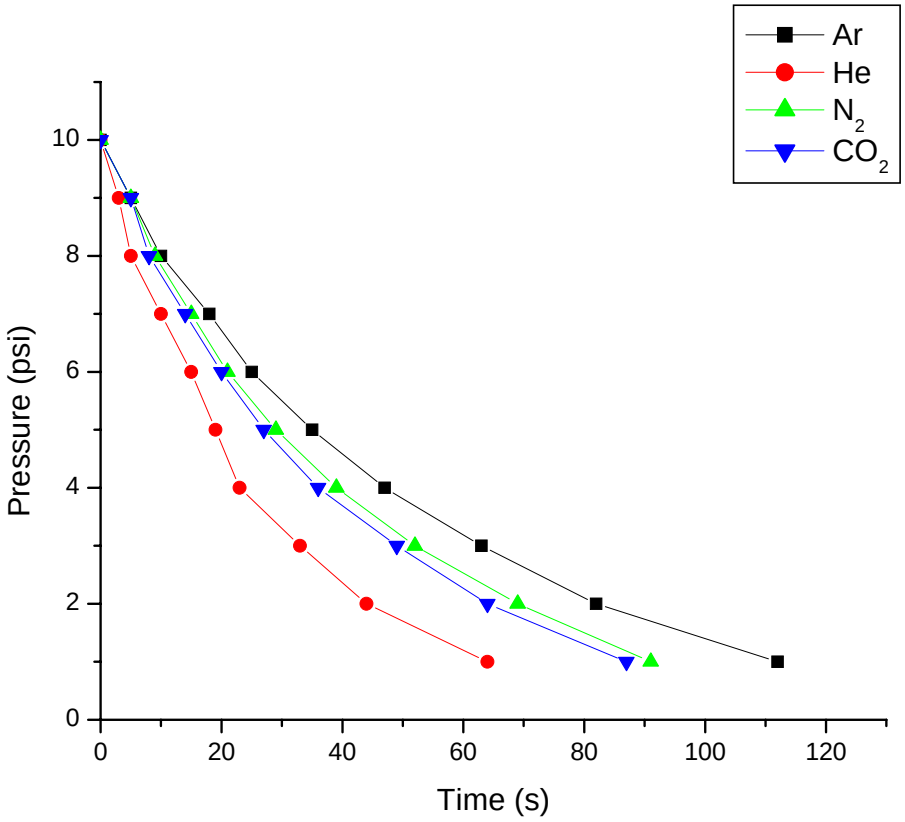

Figure 4.51 Pressure drop versus time of constant volume of gas through multilayer carbon/carbide membrane chlorinated at 350 °C.

4.6 Applications

CDCs, having tunable large surface area and pore volume, are ideal candidate materials for use in separation applications. The following applications in particular were investigated to understand CDC's adsorption and separation capabilities.

4.6.1 Protein Adsorption

Proteins TNF-α, IL-1β, IL-6, and IL-8 are inflammatory proteins produced in the body in the case of sepsis, a systematic response which leads to the death of over 1500

people worldwide each day. Cytokine removal from blood via hemoadsorption may help to bring under control the unregulated pro- and anti-inflammatory processes driving sepsis. To test CDC's ability to remove cytokines from blood plasma, two carbon sorbents were used as controls. Adsorba 300C is an activated carbon produced by Norit from peat, and coated with a 3-5 μm thick cellulose membrane for better hemocompatibility. It is commercially used in adsorbent-assisted extracorporeal systems manufactured by Gambro, Sweden. CXV, a carbon adsorbent manufactured by CECA (subsidiary of Arkema, France) was also used. Although currently unapproved for medical use, it has shown potential for sorption of cytokines and is considered a benchmark for cytokine adsorption. For this study, CDC produced from Ti_2AlC-CDC and Ti_3AlC_2-CDC chlorinated at 600, 800, and 1200 °C were compared to the control carbon sorbents.

4.6.1.1 Micro and Mesoporosity of Sorbents

The micro and mesoporosity of the CDC samples were determined by gas sorption techniques. Ar sorption analysis performed at 77K was used to compare the microporosity of the Adsorba 300C and CXV to the carbide derived carbon samples. Figure 4.52 shows the pore size distributions that were derived using NLDFT based on the Ar sorption isotherms.

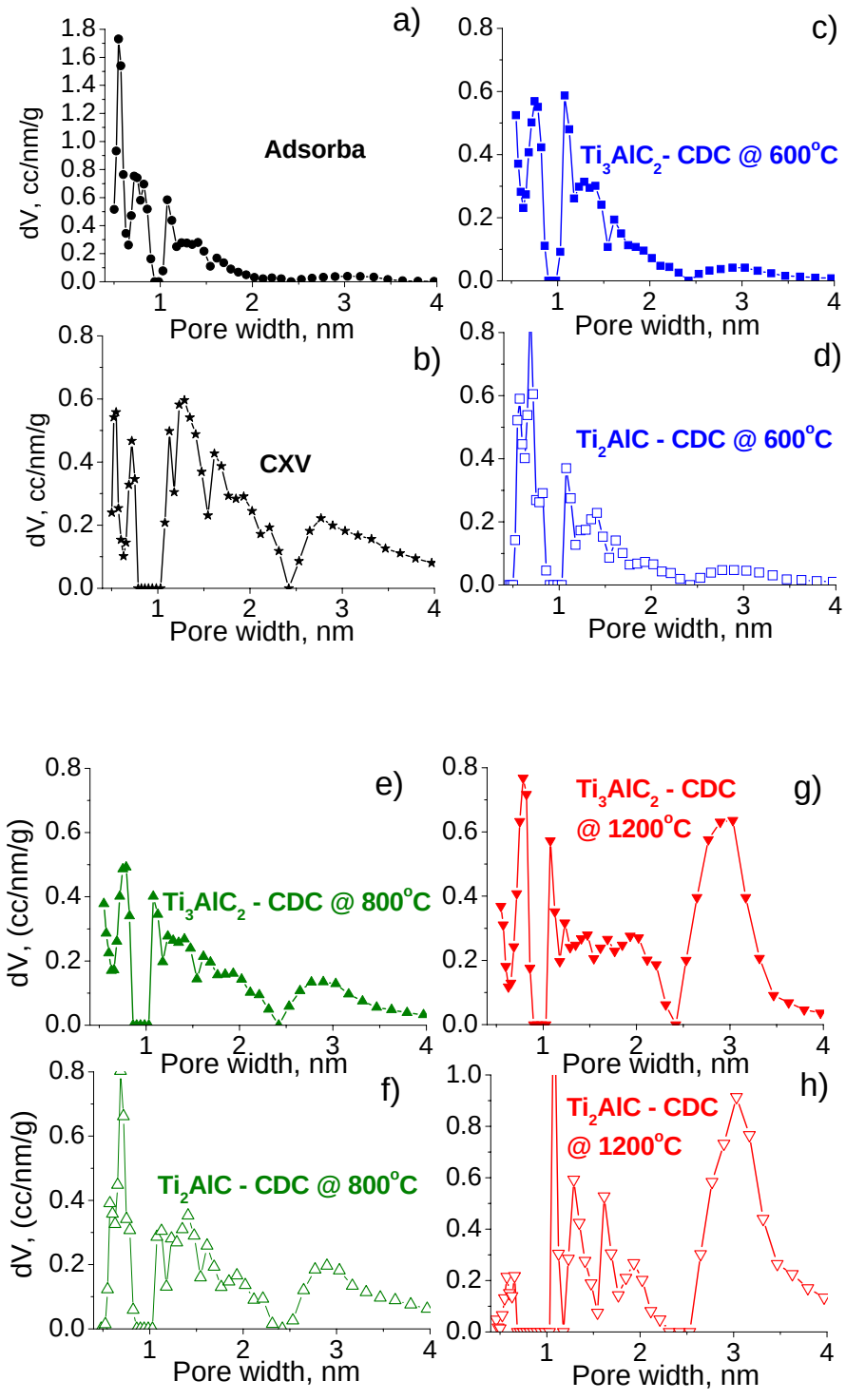

Figure 4.52 NLDFT pore size distributions from Ar sorption isotherms of carbon controls, (a) Adsorba 300C and (b) CXV, compared to CDC produced from Ti_2AlC and Ti_3AlC_2 chlorinated at (c and d) 600 °C, (e and f) 800 °C, and (g and h) 1200 °C.

The pore size distributions from Ar sorption isotherms of CDC confirm previous results in that the pore size distributions broaden with increasing chlorination temperature. Both Ti_2AlC and Ti_3AlC_2 derived carbon produced at 1200 °C show increased porosity at pore widths of 3 nm compared to the CDC produced at 600 °C.

The mesoporosity of the control carbons was compared to the CDC using the N_2 adsorption isotherms measured at 77K, Figure 4.53. A hysteresis is present in each of the isotherms of the Ti_2AlC-CDC series, with the largest hysteresis measured for CDC chlorinated at 800 °C, signifying the presence of mesopores. When comparing the isotherms of the CDC to the isotherm of CXV, which also shows a Type IV isotherm (Figure 4.53b), the total quantity of gas adsorbed, although higher than CDC chlorinated at 600 °C, does not reach the magnitude of the 800 or 1200 °C samples. The Adsorba 300C control, unlike the other carbon samples, shows a Type I isotherm, which suggests the absence of mesopores.

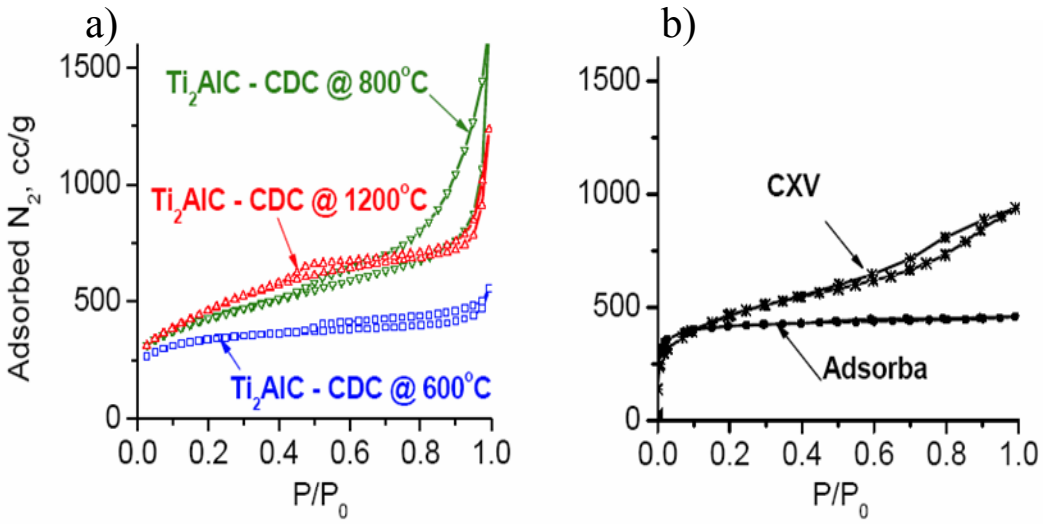

Figure 4.53 Nitrogen sorption isotherms of (a) Ti_2AlC CDC, (b) CXV and Adsorba 300C samples. N_2 isotherms for Ti_3AlC_2-CDC are very similar to the isotherms for Ti_2AlC-CDC synthesized at identical temperatures. (not shown)

Using NLDFT method, the N_2 adsorption at 77K isotherms were converted into pore size distributions, see Figure 4.54. A small volume of mesopores exist in the Adsorba 300C. CXV has significant amounts of pores with widths up to 15 nm. The CDC of both Ti_2AlC and Ti_3AlC_2 chlorinated at 600 °C has a small volume of pores greater than 5 nm in width.

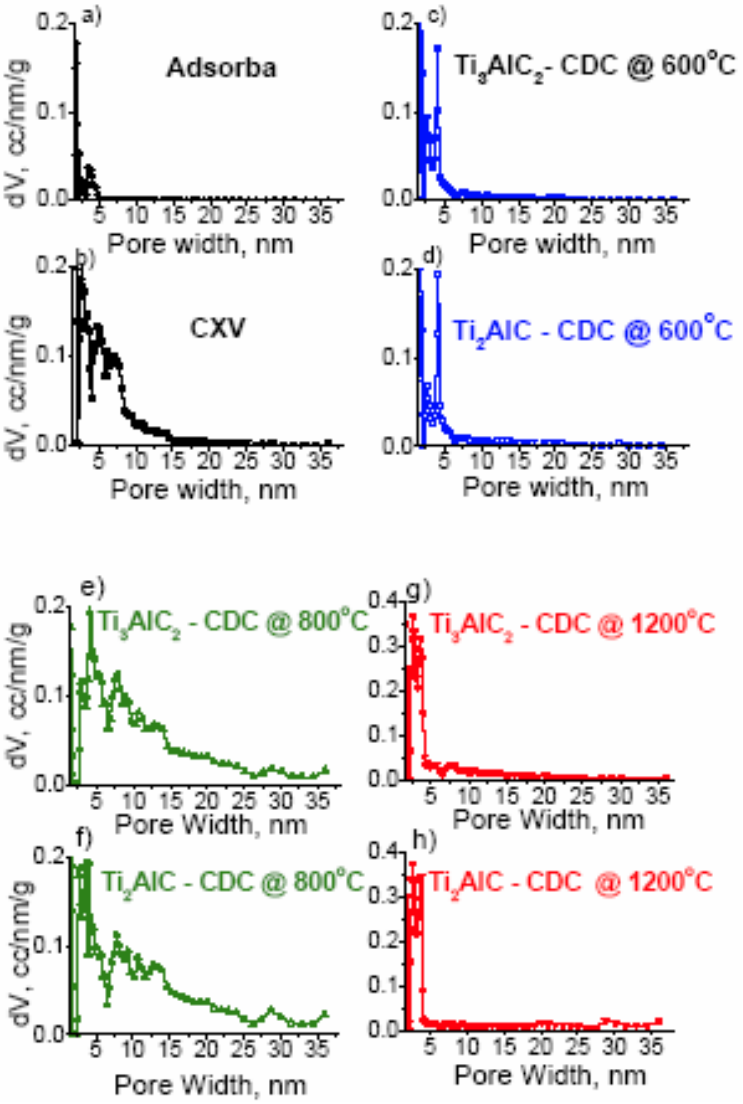

Figure 4.54 Pore size distributions derived from N_2 sorption isotherms of carbon controls Adsorba 300C (a) and CXV (b) compared to CDC produced from Ti_2AlC and Ti_3AlC_2 chlorinated at 600 °C (c and d), 800 °C (e and f), and 1200 °C (g and h).

A similar trend is found for CDC chlorinated at 1200 °C. For CDC chlorinated at 800 °C, however, a significant volume of pores exist up to pore widths of 35 nm, which is the limitation of the NLDFT analysis using N_2 as an adsorbate.

4.6.2 Protein Concentration

ELISA tests performed on CDC and control carbon samples resulted in a protein concentration difference amongst the carbon sorbents. Adsorba 300C and CDC produced at 600°C, which lack a large quantity of mesopores, did not noticeably change the IL-6 or TNF-α concentration over a 60 minute time period. CDC produced at 1200 °C and CXV also demonstrated limited success in the adsorption of TNF-α, decreasing its concentration by about 40 % after 60 minutes of adsorption, Figure 4.55. Note the log scale on the y-axis. In contrast, both CDC samples prepared at 800 °C decreased the protein concentration by over 13 times in the 60 minute time period. A minimal difference exists between the amount of protein adsorbed by Ti_3AlC_2 and Ti_2AlC derived carbons for a given chlorination temperature. However, Ti_2AlC-CDC outperformed Ti_3AlC_2-CDC at every temperature other than 600 °C. The slight difference in protein sorption can be linked to the N_2 pore size distributions, and is so slight that it may be a product of experimental error.

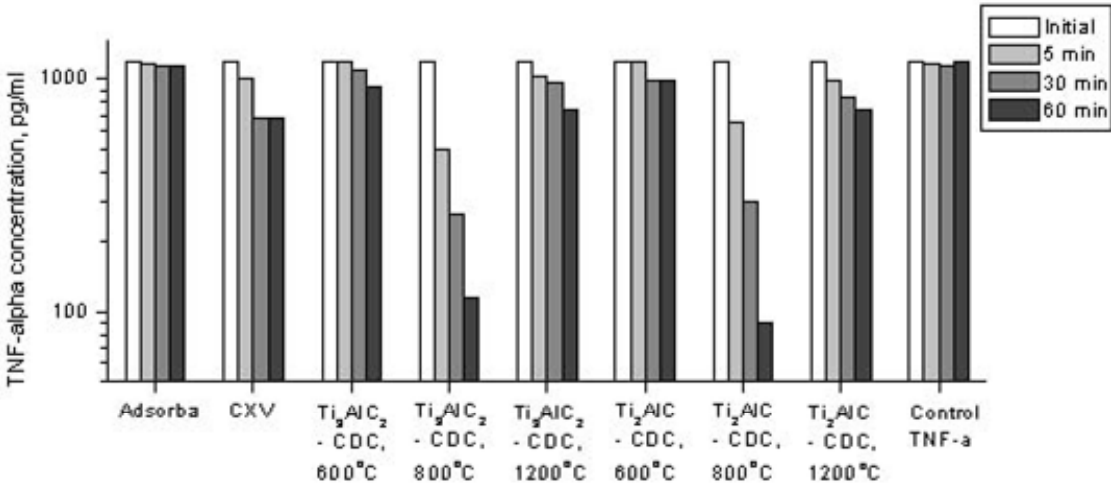

Figure 4.55 Concentration of TNF-α in the plasma solution initially and after 5, 30, and 60 minutes of adsorption.

Adsorption of TNF-α is known to be a challenge, due to the large size (> 9.4 nm) of the trimeric form of this cytokine. The adsorption capacity of CXV and 1200 °C samples were similar to that observed in advanced porous carbon hemoadsorption systems [89]. In the experiments involving CDC produced at 800 °C, the carbon material outperformed all other material or method for the efficient removal of TNF-α, and the results are comparable only to highly specific antibody-antigen interactions [90, 91].

Adsorption of the smaller cytokine IL-6 by most of the studied carbons was noticeably higher, but demonstrated similar trends, see Figure 4.56. Adsorba 300C was not successful in adsorbing this protein. However, CDCs prepared at 600 °C, having a limited amount of mesopores, adsorbed 66 to 77 % of the cytokines initially present in the solution in 60 minutes. The CDCs produced at 1200 °C demonstrated 97-98.5 % adsorption, which is comparable to the CXV sample, capable of adsorbing ~ 99 %. The CDCs prepared from Ti_2AlC at 800 °C, having the most developed mesoporosity, see

Figure 4.53, decreased IL-6 concentration by ~ 99.8 %; the remaining IL-6 was close to the detection limit of the ELISA used.

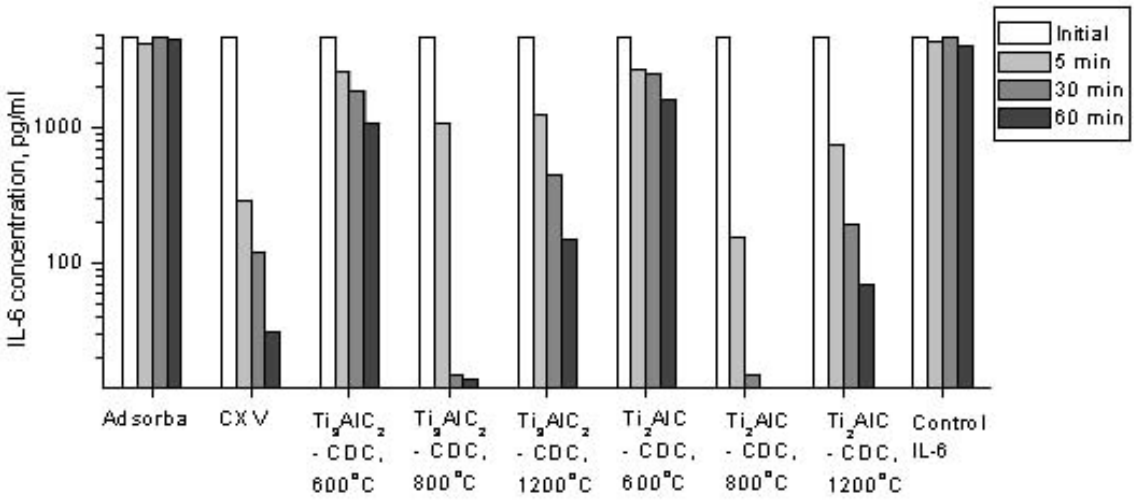

Figure 4.56 Concentration of IL-6 in the plasma solution initially and after 5, 30, and 60 minutes of adsorption.

The cytokine IL-6, being a smaller protein than TNF-α, was adsorbed with less difficultly than TNF-α presumably because it is capable of accessing a greater number of pores, resulting in a larger accessible surface area compared to the larger TNF-α. When plotting the amount of protein adsorbed as a function of the total specific surface area of the carbon materials, no trend is discernable (Figure 4.57).

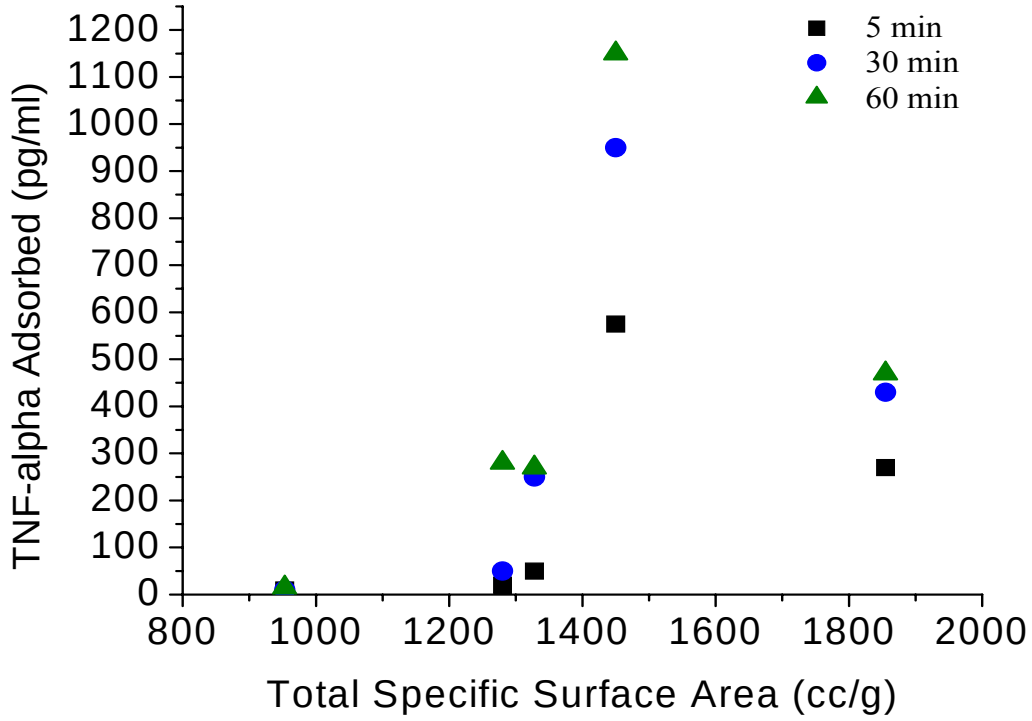

Figure 4.57: TNF-alpha adsorbed by Ti_2AlC-CDC and Ti_3AlC_2-CDC chlorinated at 600, 800, and 1200 °C, and Adsorba and CXV as a function of total specific surface area.

However, a clear dependence of protein removal efficiency on the PSDs of the porous carbons is seen by plotting protein adsorption as a function of the carbons' accessible surface area, which is approximated as the SSA of pores exceeding the smallest dimension in protein size, see Figure 4.58. The SSA was determined by the NLDFT of the N_2 adsorption isotherms shown in Figure 4.53. The dimensions of the investigated cytokines were assumed to be: 9.4 x 9.4 x 11.7 nm (trimer of TNF-α) [92], 5.5 x 5.5 x 7.7 nm (IL-1β) [93], 5 x 5 x 12.2 nm (IL-6) [94], 4 x 4 x 9 nm (IL-8) [95]. The larger the surface areas of the porous carbons accessible to a given cytokine, the more cytokines were adsorbed in a given time. Slight scatter in the results obtained could be explained by experimental errors in the estimation of the cytokine concentration and/or

the carbon pore size distribution. Depending on the cytokine and its initial concentration, values of the accessible SSA above 50-100 m^2/g were generally sufficient for fast and efficient cytokine removal. The relatively short and small IL-1β and IL-8 cytokines diffused so rapidly into the carbon pores that 5 min was sufficient to adsorb most of these proteins by carbons with accessible SSA exceeding 500 m^2/g. The existence of larger channels, which most likely formed due to the layered nature of MAX-phase carbides, should have further accelerated the adsorption process. IL-6 demonstrated slower adsorption, probably due to its longer dimensions and hence slower diffusion within the carbon pore structure. The TNF-α trimer, the largest adsorbate, demonstrated the slowest adsorption rate, as the amount of pores exceeding three times the adsorbate size needed for fast diffusion, was limited.

Essentially the difference in adsorption between highly sorbent CDC produced at 800 °C and minimally adsorbing Adsorba 300C is accessible surface area. In the case of Adsorba 300C, which is primarily microporous, the protein molecules are unable to access the surface area within the carbon particles. Therefore, molecules are only capable of using the outer surface of each particle. In the case of CDC produced from Ti_2AlC and Ti_3AlC_2, the protein molecules are capable of adsorbing both on the surface of the particles, as well as in the bulk of each particle through the mesopores, thereby greatly increasing the surface area accessible for sorption, see Figure 4.59. Therefore, when designing materials for optimum sorption of large molecules, such as cytokines, it is critical to optimize the mesopores volume.

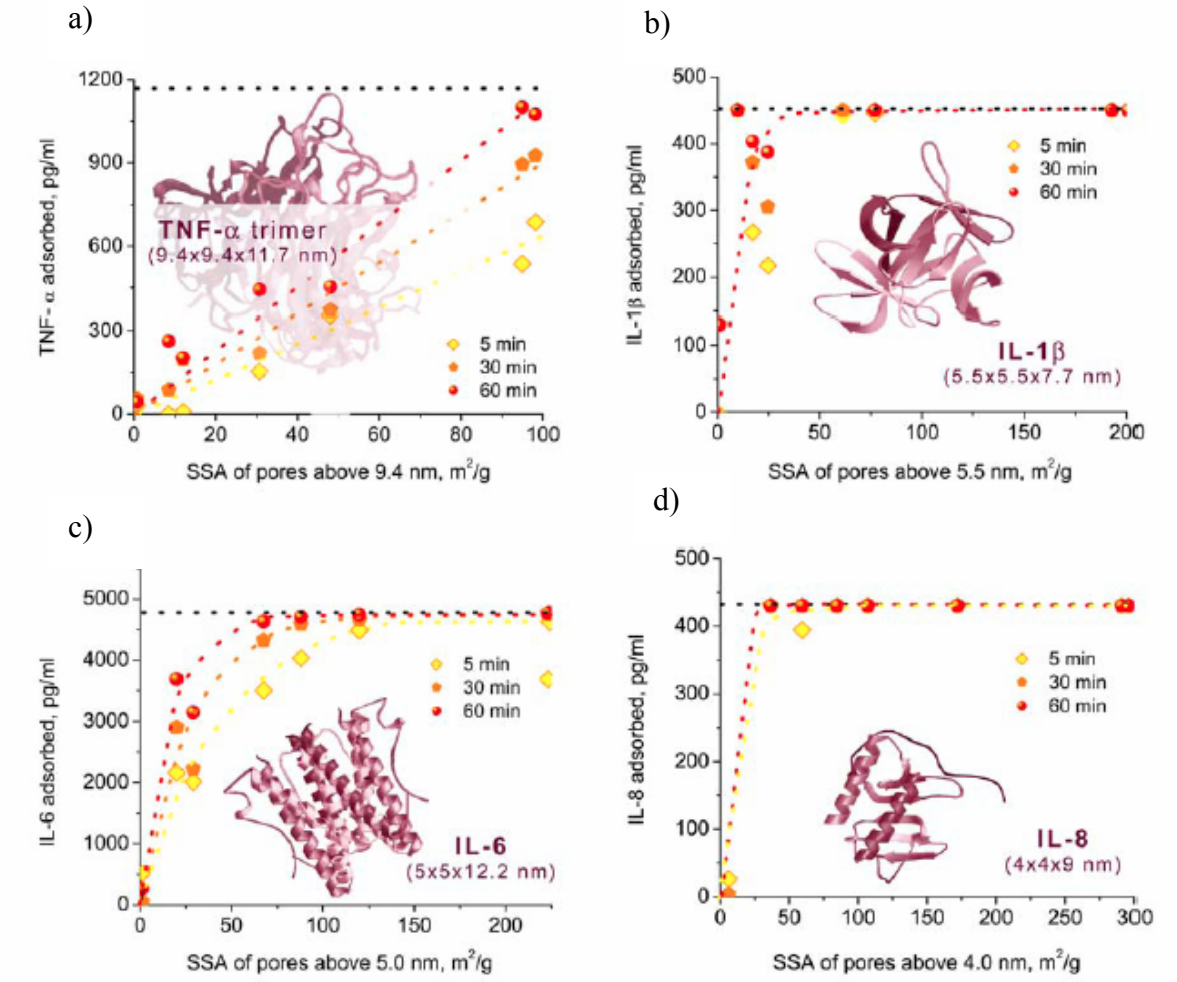

Figure 4.58 Adsorption of cytokines by porous carbons as a function of the surface area accessible to the cytokines. (A) TNF-α, (B) IL-1β, (C) IL-6, (D) IL-8. The accessible area is approximated as the SSA of pores exceeding the smallest protein dimension in size: 9.4 nm for TNF-α trimer, 5.5 nm for IL-1β, 5 nm for IL-6, and 4 nm for IL-8. Amount of the adsorbed cytokines was measured after 5, 30, and 60 min adsorption. Larger carbon surface area accessible to the cytokines clearly results in faster and more complete adsorption. The horizontal dotted black line on the top of each graph indicates the initial concentration of the cytokines in the plasma.

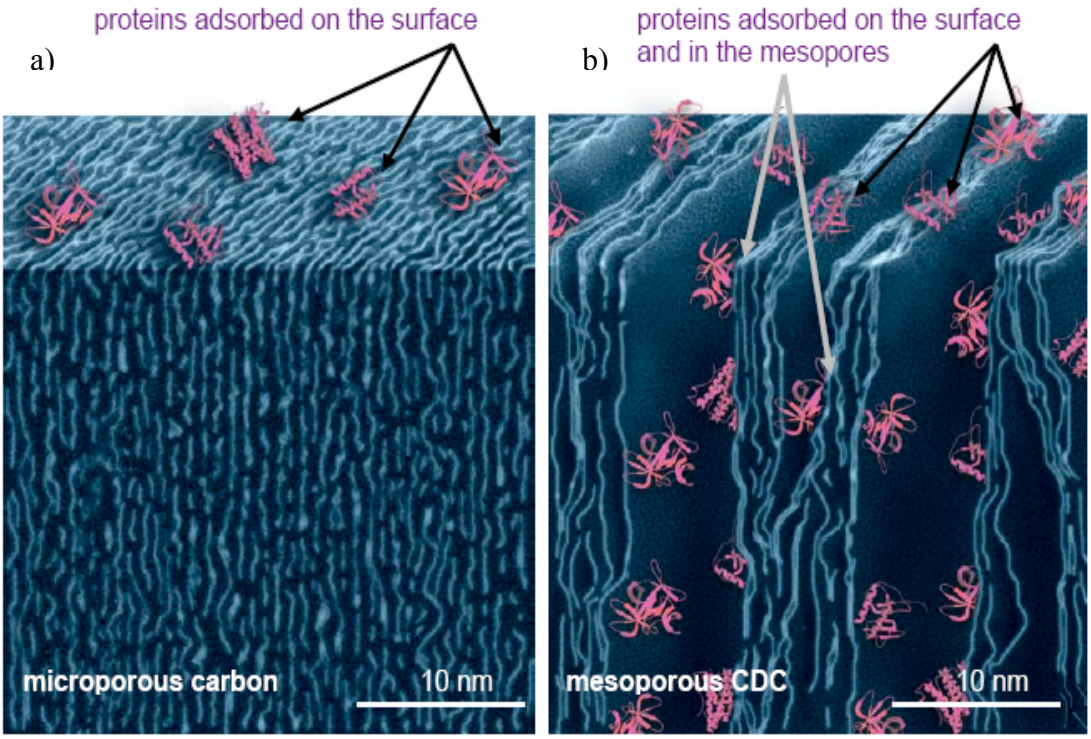

Figure 4.59 Schematics of protein adsorption by porous carbons. (A) Surface adsorption in microporous carbon. Small pores do not allow proteins (shown in pink) to be adsorbed in the bulk of carbon particles (shown in blue). (B) Adsorption in the bulk of mesoroporous CDC. Large mesopores are capable to accommodate most of the proteins. Carbon particles are shown in cross-section. Alignment of the slit-shaped pores drawn in both illustrations is a simplification.

A brief study of Ti_3SiC_2-CDC was also performed (Figure 4.60), however, the results are difficult to compare to the Ti_2AlC-CDC and Ti_3AlC_2-CDC materials due to the difference in synthesis temperatures between the two sets of materials and variations in the protein testing such as initial concentration of proteins and time for sorption analysis. However, based on the results, CDC produced from Ti_3SiC_2-CDC chlorinated at 300 and 1100 °C, particularly the one chlorinated at 1100 °C, result in increased TNF-α adsorbed compared to reference carbons Adsorba 300C and Carbon 1012.

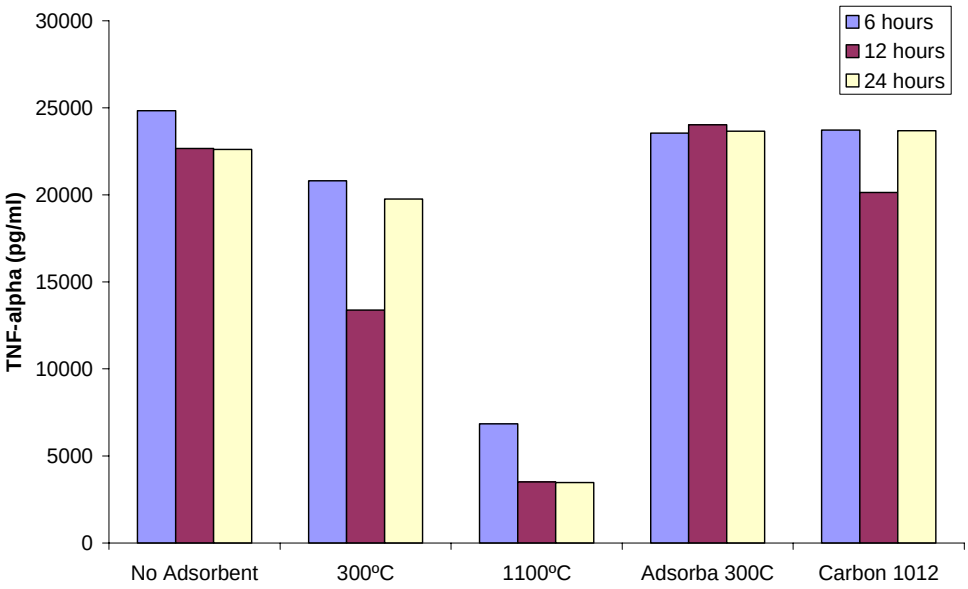

Figure 4.60: TNF-alpha concentration over 6, 12, and 24 h for Ti_3SiC_2-CDC chlorinated at 300 and 1100 °C compared to Adsorba 300C and Carbon 1012 reference carbons. An initial protein concentration of 1 µg/ml was used. (ELISA testing performed at University of Brighton)

4.6.3 Gas Separation

Using sorption analysis, Ti_3SC_2-CDC produced at 600 °C was tested using CH_4, CO_2, H_2, and SF_6 as adsorbates at 25 °C, see Figure 4.61. The adsorption of CO_2 was the highest with 125 cc/g adsorbed, while the adsorption of H_2 was the lowest with ~0 cc/g adsorbed. The maximum amounts of SF_6 and CH_4 absorbed were 105 and 55 cc/g, respectively. Sorption analysis was also tested on Ti_3SC_2-CDC produced at 600 °C, then H_2 annealed at 800 °C, see Figure 4.62. The sorption results are similar to those of the non-H_2 annealed material, however, SF_6 was the adsorbate with the maximum volume absorbed with 140 cc/g absorbed. CO_2 was not absorbed nearly as much compared to the non-annealed material, with 70 cc/g absorbed compared to 125 cc/g on the non-annealed material. CH_4 also had a lower adsorption with 20 cc/g adsorbed compared to 55 cc/g in the non-annealed material.

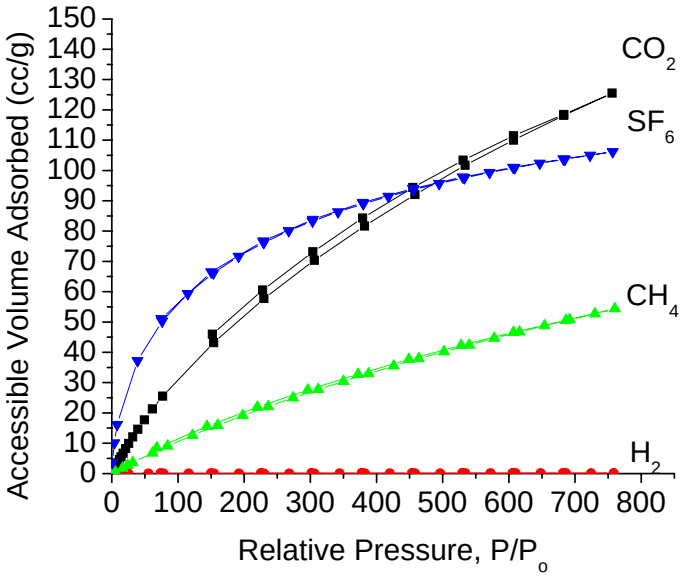

Figure 4.61 Sorption analysis of Ti_3SiC_2-CDC produced at 600 °C using CH_4, CO_2, H_2, and SF_6 as adsorbates.

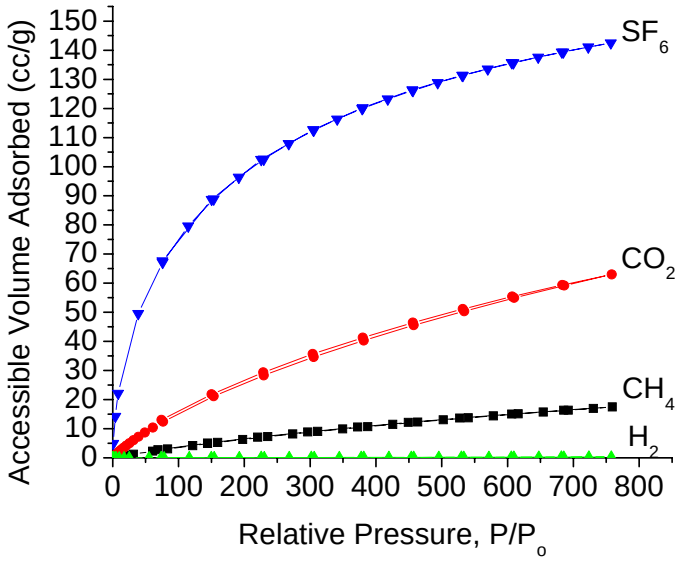

Figure 4.62 Sorption analysis of Ti_3SiC_2-CDC produced at 600 °C, then H_2 annealed at 800 °C for 5 h, using CH_4, CO_2, H_2, and SF_6 as adsorbates.

When the sorption results are compared to the kinetic diameters of the adsorbates, it is clear that both Ti_3SC_2-CDC samples are not absorbing relative to molecular size.

From the adsorption experiments, it is also clear that Ti_3SC_2-CDC does not act as a molecular sieve, but as a selective sorbent. The interaction between the carbon surface and the gas molecules has a greater dependence on the relative adsorption of the adsorbates. CDC adsorbs gases relative to the adsorbate boiling point, which is taken as evidence of equilibrium separation.

To understand the interaction between the carbon surface and the adsorbate gas molecules, the heat of adsorption for CO_2 and H_2, two of the extreme adsorbate gases, on Ti_3SC_2-CDC produced at 600 °C then H_2 annealed at 800 °C was measured. Higher values for the heat of adsorption represent a strong interaction between adsorbate and sorbent. The average heat of adsorption of CO_2 on the porous carbon was 13.5 kJ/mol calculated using 0 and 10 °C isotherms, see Figure 4.63. The average heat of adsorption for H_2 on the same material was 6.5 kJ/mol calculated using 77 and 87 K isotherms, see Figure 4.64. Previous studies on the heat of adsorption of H_2 on binary CDCs resulted in heat of adsorption values between 6.3-7.3 kJ/mol, with materials with larger pores resulting in lower heat of adsorption values [88]. The measured heat of adsorption for H_2 on Ti_3SiC_2-CDC of 6.5 kJ/mol falls within this range.

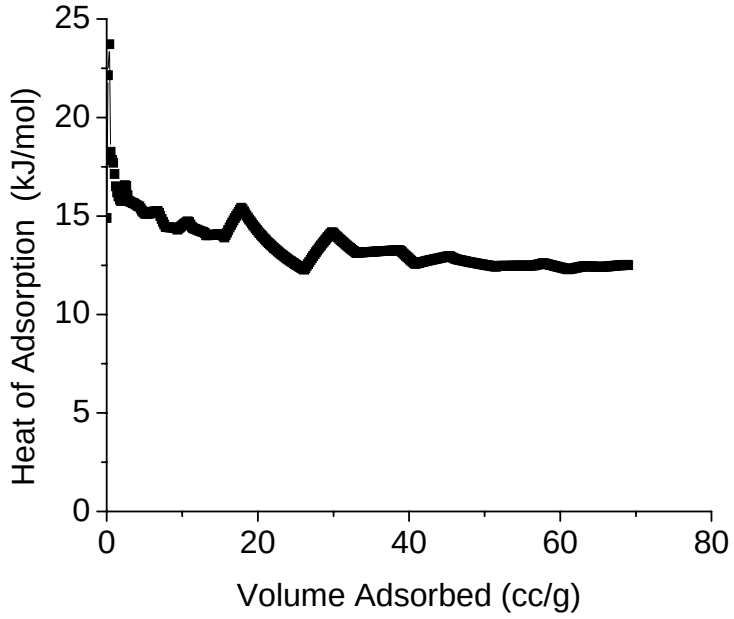

Figure 4.63 Heat of adsorption calculations for CO_2 in Ti_3SiC_2-CDC produced at 600 °C, H_2 annealed at 800 °C. Isotherms were measured at 0 and 10 °C.

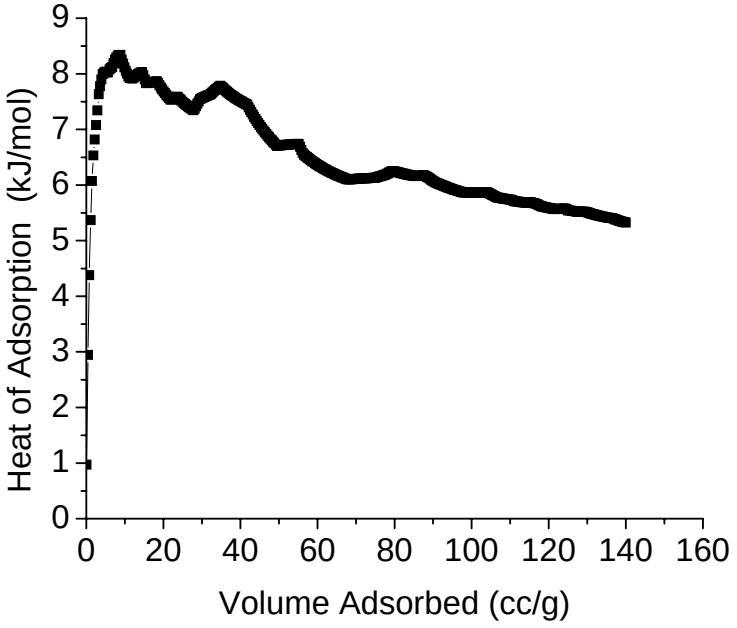

Figure 4.64 Heat of adsorption calculations for H_2 in Ti_3SiC_2-CDC produced at 600 °C, H_2 annealed at 800 °C. Isotherms were measured at 77 and 87 K

Relative to H_2, the higher heat of adsorption values for CO_2 on Ti_3SiC_2-CDC suggests that CO_2 is adsorbed more readily than H_2. Therefore, if a gas mixture of CO_2 and H_2, the interaction between the gases and the carbon surface would suggest that the CO_2 would permeate at a slower rate compared to H_2, thereby potentially separating the mixture based on selective adsorption.

The results obtained from the heat of adsorption measurements confirm that gas adsorption within Ti_3SC_2-CDC is related to surface interactions and the chemical affinity of adsorbate gases on the carbon surface, rather than a size exclusion effect.

5 Conclusions and Future Work

5.1 Conclusions

- Porosity of CDC can be varied by changing the chemistry of the initial ternary carbide as well as the chlorination temperature. CDCs produced from ternary carbides develop similar porosity trends as compared to their binary carbides. Increasing the chlorination temperature results in a broadening of the PSD. The stoichiometry was also found to affect the porosity of CDCs, with carbon produced from 312 phases having a greater volume of micropores as compared to the 211 phases.
- The larger the metallic atomic radii of the initial carbide the larger the accessible pore volume. This trend holds true for both ternary and binary carbides.
- Large cracks, which may be considered macropores, form due to a collapse in the structure of solids with extremely high theoretical pore volumes, and further promoted by the layered structure of the carbide precursors. The macropore volume is formed at the expense of the micro and mesopore volumes. Minimum carbon structure collapse occurs in samples containing a high carbon to metal/metalloid ratios, which provides ample C to support the porous carbon structure. Said otherwise, the lower the C-content in the precursors the more likely the collapse.
- Macropores are undetectable by gas sorption analysis, which explains why the measured pore volumes are less than the theoretical pore volumes.
- Cracking does not affect the shape of the CDC bodies at the macroscale.
- Hydrogen annealing aids in opening pores clogged due to metal chlorides in the CDCs produced at low chlorination temperatures. Metal chloride blocked pores are

another reason why the theoretical pore volume does not always match the measured pore volume.

- The CDCs produced behave as molecular sieve adsorbenst for large protein molecules (> 5nm). A direct correlation exists between the volume of pores of a diameter larger than the protein molecule and the amount of protein sorbed. Using CDC with large volumes of mesoporosity, the adsorption of large cytokine molecules, such as TNF-α, IL-1β, IL-6, and IL-8, surpasses the adsorption capacity of current benchmark carbon adsorbents Absorba and CXV.
- CDC adsorb gases relative to their boiling point temperatures which is taken as evidence of equilibrium separation.
- Thin-film carbon membranes have been developed on ceramic substrates via chlorination of a thin carbide layer deposited by a magnetron sputtering technique. Gas permeation through the multilayered membrane and CDC/PVDF membrane has been achieved.

5.2 Future Work

5.2.1 Carbide Derived Carbon Membrane Characterization

A crack and defect free carbide derived carbon membrane made by the chlorination of metal carbide layer deposited by magnetron sputtering must be characterized for permeation and selectivity of gases and aqueous solutions. The thickness of the CDC membrane may be varied to determine optimum thickness for selectivity and permeation.

Additionally, a CDC/polymer composite membrane should be characterized for permeation and selectivity and compared with the membrane developed through the magnetron sputtering technique.

5.2.2 Protein Sorption

Improving the selectivity and permeation of protein adsorption in the CDCs will be critical for potential applications. Improvements in selectivity and permeation can be investigated by modifying porosity, surface chemistry, and pH. Protein adsorption as a function of powder particle size is also important to investigate. Additionally, testing the CDC's ability of removing proteins in a membrane form compared to a powder form may be beneficial for minimizing the blood plasma contamination risk associated with using powder CDC, as well as opening new applications opportunities such as a CDC coated bandages for removal of cytokines in localized areas.

In addition to TNF-α, IL-1β, IL-6, and IL-8, other large molecules that are toxic to biological systems, for example proteins and enzymes associated with snake venom, may also be of interest to explore

5.2.3 Gas and Liquid Separation

Using a CDC membrane, separation of gas mixtures should be investigated. A mass spectrometer at the outlet would be ideal for detecting the permeating gases. Similar experiments should be conducted on aqueous solutions and mixtures of organic liquids with different sizes of molecules.

References

[1] Humphrey M, Keller GE. Separation Process Technology. New York: McGraw-Hill 1997.

[2] Yang RT. Adsorbents: Fundamentals and Applications. Hoboken, NJ: John Wiley and Sons, Inc. 2003.

[3] Lu GQ, Zhao XS. Nanoporous Materials: Science and Engineering. London: Imperial College Press 2004.

[4] Mattson JS, Mark HB. Activated Carbon: Surface Chemistry and Adsorption from Solution. New York: Marcel Dekker, Inc. 1971.

[5] Yushin G, Gogotsi Y, Nikitin A. Carbide Derived Carbon. In: Gogotsi Y, ed. *Nanomaterials Handbook*. Boca Raton, FL: CRC Press 2005:239-82.

[6] King CJ. Separation Processes. 2nd ed. New York, NY: McGraw-Hill 1980.

[7] Haselden GC. Gas Separation Fundamentals. 5th BOC Priestley Conference; 1989 1990; Birmingham: Royal Society of Chemistry; 1989.

[8] Cooney DO. Activated Charcoal: Antidotal and other Medical Uses. New York: Marcel Dekker 1980.

[9] Neuvonen P, P K, H V, V M. Activated charcoal in the treatment of hypercholesterolaemia: dose-response relationships and comparison with cholestyramine. Eur J Clin Pharmacol. 1989;37(3):225-30.

[10] Jankowska H, Swiatkowski A, Choma J. Active Carbon. New York, NY: Ellis Harwood 1991.

[11] Jagtoyen M, Thwaites M, Stencel J, McEnaney B, Derbyshire F. Adsorbent carbon synthesis from coals by phosphoric acid activation. Carbon. 1992;30(7):1089-96.

[12] Jagtoyen M, Derbyshire F. Some considerations of the origins of porosity in carbons from chemically activated wood. Carbon. 1993;31(7):1185-92.

[13] Solum MS, Pugmire RJ, Jagtoyen M, Derbyshire F. Evolution of carbon structure in chemically activated wood. Carbon. 1995;33(9):1247-54.

[14] Jankowska H, Swiatowski A, Oscik J, Kusak R. Adsorption from benzene-ethanol binary solutions on activated carbons with different contents of oxygen surface complexes. Carbon. 1983;21(2):117-20.

[15] Wennerberg AN, inventor patent 4624004. 1971.

[16] Wennerberg AN, O-Grady TM, inventors; patent 4082694. 1978.

[17] Baker RW. Membrane Technology and Applications. New York: McGraw-Hill 2000.

[18] Basmadjian D. The Little Adsorption Book: A Practical Guide for Engineers and Scientists. Boca Raton, FL: CDC Press 1997.

[19] Ash R, Barrer RM, Pope CG. Flow of Adsorbable gases and vapours in a microporous medium. Proceedings of the Royal Society A. 1963;271(19).

[20] Kusuki Y, Shimazaki H, Tanihara N, Nakanishi S, Yoshinaga T. Gas permeation properties and characterization of asymmetric carbon membranes prepared by pyrolyzing asymmetric polyimide hollow fiber membrane. Journal of Membrane Science. 1997;134(2):245-53.

[21] Fuertes AB, Centeno TA. Preparation of supported asymmetric carbon molecular sieve membranes. Journal of Membrane Science. 1998;144(1-2):105-11.

[22] Soffer A, Koresh JE, Saggy S, inventors; Separation Device patent 4,685,940 1987.

[23] Centeno TA, Fuertes AB. Carbon molecular sieve gas separation membranes based on poly(vinylidene chloride-co-vinyl chloride). Carbon. 2000;38(7):1067-73.

[24] Rao MB, Sircar S. Nanoporous carbon membrane for gas separation. Gas Separation & Purification. 1993;7(4):279-84.

[25] Shiflett MB, Foley HC. Ultrasonic Deposition of High-Selectivity Nanoporous Carbon Membranes. Science. 1999 September 17, 1999;285(5435):1902-5.

[26] Centeno TA, Vilas JL, Fuertes AB. Effects of phenolic resin pyrolysis conditions on carbon membrane performance for gas separation. Journal of Membrane Science. 2004;228(1):45-54.

[27] Fuertes AB. Adsorption-selective carbon membrane for gas separation. Journal of Membrane Science. 2000;177(1-2):9-16.

[28] Rao MA, Dukkipati RV, Tummala M. Finite element analysis of multilayered shells of revolution. Computers & Structures. 1993;47(2):253-8.

[29] Koresh J, Soffer A. A Molecular-Sieve Carbon Membrane for Continuous Process Gas Separation. Carbon. 1984;22(2):225-.

[30] Rao MB, Sircar S. Nanoporous Carbon Membranes for Separation of Gas-Mixtures by Selective Surface Flow. Journal of Membrane Science. 1993 Dec;85(3):253-64.

[31] Jones CW, Koros WJ. Carbon molecular sieve gas separation membranes-I. Preparation and characterization based on polyimide precursors. Carbon. 1994;32(8):1419-25.

[32] Hayashi J-i, Yamamoto M, Kusakabe K, Morooka S. Simultaneous improvement of permeance and permselectivity of 3,3 prime ,4,4 prime -biphenyltetracarboxylic dianhydride-4,4 prime -oxydianiline polyimide membrane by carbonization. Industrial & Engineering Chemistry Research. 1995;34(12):4364-70.

[33] Koresh JE, Sofer A. Molecular Sieve Carbon Permselective membrane. Part 1: Presentation of a new device for gas mixture separation. . Separation Science and Technology. 1983;18(8):723-34.

[34] Koros WJ, Mahajan R. Pushing the limits on possibilities for large scale gas separation: which strategies? Journal of Membrane Science. 2000;175(2):181-96.

[35] Fitzer E, Schaefer W, Yamada S. The formation of glasslike carbon by pyrolysis of polyfurfuryl alcohol and phenolic resin. Carbon. 1969;7(6):643-6.

[36] Fitzer E, Schafer W. The effect of crosslinking on the formation of glasslike carbons from thermosetting resins. Carbon. 1970;8(3):353-64.

[37] Nishiyama N, Dong Y-R, Zheng T, Egashira Y, Ueyama K. Tertiary amine-mediated synthesis of microporous carbon membranes. Journal of Membrane Science. 2006;280(1-2):603-9.

[38] Lee H-J, Yoshimune M, Suda H, Haraya K. Gas permeation properties of poly(2,6-dimethyl-1,4-phenylene oxide) (PPO) derived carbon membranes prepared on a tubular ceramic support. Journal of Membrane Science. 2006;279(1-2):372-9.

[39] Strano MS, Foley HC. Temperature- and pressure-dependent transient analysis of single component permeation through nanoporous carbon membranes. Carbon. 2002;40(7):1029-41.

[40] Carretero J, Benito JM, Guerrero-Ruiz A, Rodriguez-Ramos I, Rodriguez MA. Infiltrated glassy carbon membranes in [gamma]-Al2O3 supports. Journal of Membrane Science.In Press, Corrected Proof.

[41] Masmoudi S, Ben Amar R, Larbot A, El Feki H, Salah AB, Cot L. Elaboration of inorganic microfiltration membranes with hydroxyapatite applied to the treatment of wastewater from sea product industry. Journal of Membrane Science. 2005;247(1-2):1-9.

[42] Parks DJ, Scholl KL, Fletcher EA. A study of the use of Y2O3 doped ZrO2 membranes for solar electrothermal and solarthermal separations. Energy. 1988;13(2):121-36.

[43] Tsuru T, Kan-no T, Yoshioka T, Asaeda M. A photocatalytic membrane reactor for VOC decomposition using Pt-modified titanium oxide porous membranes. Journal of Membrane Science. 2006;280(1-2):156-62.

[44] Rajagopalan R, Foley HC. Study of the effect of morphology of nanoporous carbon membranes on permselectivity. Materials Research Society; 2003; 2003. p. 225-30.

[45] Fedorov NF. Untraditional solutions in chemical technology of carbon adsorbents. Journal of Russian Chemistry. 1995;39:73-83.

[46] Gordeev S, Kukushkin S, Osipov A, Pavlov Y. Self-organization in the formation of a nanoporous carbon material. Physics of the Solid State. 2000;42(12):2314-7.

[47] Babkin OE, Ivakhnyuk GK, Fedorov NF. Porous Structure of Carbon Adsorbents from Zirconium Carbide. Zhurnal Prikladnoi Khimii 1984;57:504-8.

[48] Hutchins O, inventor Method for the Production of Silicon Tetrachlorid. US patent 1271713. 1918.

[49] Mohun WA. A Novel Amorphous Carbon. 4th Biennial Conference on Carbon; 1959: Pergamon, Oxford; 1959. p. 443-53.

[50] Boehm HP, Warnecke HH. Structural Parameters and Molecular Sieve Properties of Carbons Prepared from Metal Carbides 12th Biennial Conference on Carbon; 1975: Pergamon, Oxford; 1975. p. 149-50.

[51] Leis J, Perkson A, Arulepp M, Kaarik M, Svensson G. Carbon Nanostructures Produced by Chlorinating Aluminium Carbide. Carbon. 2001;39:2043-8.

[52] Dash RK, Nikitin A, Gogotsi Y. Microporous Carbon Derived from Boron Carbide. Microporous and Mesoporous Materials. 2004;72:203-8.

[53] Fedorov NF, Ivakhnyuk GK, Tetenov vV, Matyuhin GV. Adsorbents based on silicon carbide. J Applied Chemistry USSR. 1981;54:1239-42.

[54] Gogotsi YG, Jeon I-D, McNallan MJ. Carbon Coatings on Silicon Carbide by Reaction with Chlorine-Containing Gases. J Mater Chem. 1997;7(9):1841-8.

[55] Zheng J, Eckström TC, Gordeev SK, Jacob M. Carbon with an Onion-Like Structure Obtained by Chlorinating Titanium Carbide. J Mater Chem. 2000;10:1039-41.

[56] Dash RK, Yushin G, Gogotsi Y. Nanoporous Carbon Derived from Zirconium Carbide. Microporous and Mesoporous Materials. 2005;86:50-7.

[57] Chen XQ, Cantrell DR, Kohlhaas K, Stankovich S, Ibers JA, Jaroniec M, et al. Carbide-derived nanoporous carbon and novel core-shell nanowires. Chemistry of Materials. 2006 Feb;18(3):753-8.

[58] Cambaz ZG, Yushin GN, Gogotsi Y, Vyshnyakova KL, Pereselentseva LN. Formation of carbide-derived carbon on beta-silicon carbide whiskers. Journal of the American Ceramic Society. 2006 Feb;89(2):509-14.

[59] Erdemir A, Kovalchenko A, White C, Zhu R, Lee A, McNallan MJ, et al. Synthesis and tribology of carbide-derived carbon films. International Journal of Applied Ceramic Technology. 2006;3(3):236-44.

[60] Ersoy DA, McNallan MJ, Gogotsi Y. Carbon coatings produced by high temperature chlorination of silicon carbide ceramics. Materials Research Innovations. 2001;5(2):55-62.

[61] Welz S, McNallan MJ, Gogotsi Y. Carbon structures in silicon carbide derived carbon. Journal of Materials Processing Technology.In Press, Corrected Proof.

[62] Dimovski S, Nikitin A, Ye HH, Gogotsi Y. Synthesis of graphite by chlorination of iron carbide at moderate temperatures. Journal of Materials Chemistry. 2004;14(2):238-43.

[63] Dash R, Chmiola J, Yushin G, Gogotsi Y, Laudisio G, Singer J, et al. Titanium carbide derived nanoporous carbon for energy-related applications. Carbon. 2006;In Press.

[64] Gogotsi Y, Nikitin A, Ye H, Zhou W, Fischer JE, Yi B, et al. Nanoporous Carbide-Derived Carbon with Tunable Pore Size. Nature Materials. 2003;2:591-4.

[65] Chmiola J, Yushin G, Dash R, Gogotsi Y. Effect of pore size and surface area of carbide derived carbons on specific capacitance. Journal of Power Sources. 2006;158(1):765-72.

[66] McNallan M, Ersoy D, Zhu R, Lee A, White C, Welz S, et al. Nano-Structured Carbide-Derived Carbon Films and Their Tribology. Tsinghua Science & Technology. 2005;10(6):699-703.

[67] Erdemir A, Kovalchenko A, McNallan MJ, Welz S, Lee A, Gogotsi Y, et al. Effects of high-temperature hydrogenation treatment on sliding friction and wear behavior of carbide-derived carbon films. Surface and Coatings Technology. 2004;188-189:588-93.

[68] Barsoum MW. The MN+1AXN phases: A new class of solids : Thermodynamically stable nanolaminates. Progress in Solid State Chemistry. 2000;28(1-4):201-81.

[69] Ferrari AC. Raman spectroscopy of amorphous carbon films: State of the art. New Diamond and Frontier Carbon Technology. 2004;14(2):87-108.

[70] Neimark AV, Ravikovitch PI. Calibration of pore volume in adsorption experiments and theoretical models. Langmuir. 1997 Sep;13(19):5148-60.

[71] Brunauer S, Deming LS, Deming WE, Teller E. On a Theory of the van der Waals Adsorption of Gases. 1940;62:1723.

[72] Webb PA, Orr C. Analytical Methods in Fine Particle Technology. Micrometric Instruments Corp. 1997.

[73] Pribylov AA, Kalinnikova IA, Regent NI. Features of sulfur hexafluoride adsorption on carbon adsorbents. Russian Chemical Bulletin. 2003;52(4):882-8.

[74] Ravikovitch PI, Neimark AV. Characterization of nanoporous materials from adsorption and desorption isotherms. Colloids and Surfaces A: Physicochemical and Engineering Aspects. 2001;187-188:11-21.

[75] Brunauer S, Emmett P, Teller E. Adsorption of Gases in Multimolecular Layers. Journal of American Chemical Society. 1938;60:309-19.

[76] Wendler B, Danielewski M, Przybylski K, Rylski A, Kaczmarek L, Jachowicz M. New type AlMo-, AlTi- or Si-based magnetron sputtered protective coatings on metallic substrates. Journal of Materials Processing Technology. 2006;175(1-3):427-32.

[77] Defife KM, Anderson JKYAASSKINNECJM. Adhesion and cytokine production by monocytes on poly(2-methacryloyloxyethyl phosphorylcholine-<I>co</I>-alkyl methacrylate)-coated polymers. Journal of Biomedical Materials Research. 1995;29(4):431-9.

[78] Nemanich RJ, Lukovsky G, Solin SA. In: Balkanski M, ed. *In Proc Int Conf on Lattice Dynamics*. Paris: Flammarion Press 1975:619-21.

[79] Tuinstra F, Koenig JL. Raman spectrum of graphite. J Chem Physics. 1970;53(3):1126-30.

[80] Ferrari AC. Determination of bonding in diamond-like carbon by Raman spectroscopy. Diam Related Mater. 2002;11:1053-61.

[81] Ferrari AC, Robertson J. Interpretation of Raman spectra of disordered and amorphous carbon. Phys Rev B. 2000;61:14095-107.

[82] Negri F, di Donato E, Tommasini M, Castiglioni C, Zerbi G, Mullen K. Resonance Raman contribution to the D band of carbon materials: Modeling defects with quantum chemistry. J Chem Phys. 2004;120(24):11889-900.

[83] Mapelli C, Castiglioni C, Meroni E, Zerbi G. Graphite and graphitic compounds: vibrational spectra from oligomers to real materials. J Mol Struct. 1999;481:615-20.

[84] Ferrari AC, Robertson J. Interpretation of Raman spectra of disordered and amorphous carbon. Physical Review B. 2000;61(14):95-107.

[85] Gogotsi Y, Kamyshenko V, Shevchenko V, Welz S, Ersoy DA, McNallan MJ. Nanostructured Carbon Coatings on Silicon Carbide: Experimental and Theoretical Study. In: Baraton M-I, Uvarova I, eds. *NATO ASI on Functional Gradient Materials and Surface Layers Prepared by Fine Particles Technology*. Dordrecht: Kluwer Academic Publishers 2001:239-55.

[86] Gamarnik MY, Barsoum MW. Bond length in the ternary compounds Ti3SiC2, Ti3GeC2 and Ti2GeC. J of Mater Sci. 1999;34:169-74.
[87] Kisi EH, J. A. Crossley, S. Myhra, M.W. Barsoum. Structure and Crystal Chemistry of Ti3SiC2. J Phys Chem Solids. 1998;59(9):1437-43.

[88] Dash R. Nanoporous Carbons Derived from Binary Carbides and their Optimization for Hydrogen Storage. Philadelpiha, PA: Drexel University; 2006.

[89] Kellum JA, Song MC, Venkataraman R. Hemoadsorption removes tumor necrosis factor, interleukin-6, and interleukin-10, reduces nuclear factor-kappa B DNA binding, and improves short-term survival in lethal endotoxemia. Critical Care Medicine. 2004 Mar;32(3):801-5.

[90] Hinterdorfer P, Baumgartner W, Gruber HJ, Schilcher K, Schindler H. Detection and localization of individual antibody-antigen recognition events by atomic force microscopy. PNAS. 1996 April 16, 1996;93(8):3477-81.

[91] Weber V, Linsberger I, Ettenauer M, Loth F, Hoyhtya M, Falkenhagen D. Development of specific adsorbents for human tumor necrosis factor-alpha: Influence of antibody immobilization on performance and biocompatibility. Biomacromolecules. 2005 Jul-Aug;6(4):1864-70.

[92] Reed C, Fu ZQ, Wu J, Xue YN, Harrison RW, Chen MJ, et al. Crystal structure of TNF-alpha mutant R31D with greater affinity for receptor R1 compared with R2. Protein Engineering. 1979;10:1101-7.

[93] Einspahr H, Clancy LL, Muchmore SW, Watenpaugh KD, Harris PKW, Carter DB, et al. Crystallization of Recombinant Human Interleukin-1-Beta. Journal of Crystal Growth. 1988 Jul;90(1-3):180-7.

[94] Somers W, Stahl M, Seehra JS. 1.9 angstrom crystal structure of interleukin 6: Implications for a novel mode of receptor dimerization and signaling. Embo Journal. 1997 Mar;16(5):989-97.

[95] Rajarathnam K, Clarklewis I, Sykes BD. H-1-Nmr Solution Structure of an Active Monomeric Interleukin-8. Biochemistry. 1995 Oct;34(40):12983-90.

Appendix A: Membrane Synthesis, Unsuccessful Methods

During the process of developing a carbon membrane, several attempts were made which were unsuccessful in producing a membrane. Below are descriptions of the unsuccessful attempts.

- *Bulk Disc*
  A disc of Ti_3SiC_2-CDC, 25 mm in diameter and 3 mm thick, was completely chlorinated as determined by weight measurements. However, since bulk CDC alone contains numerous large cracks (see Figure 4.21). These cracks provided minimal resistance paths though the CDC, bypassing the large surface area and porosity available for use.

- *Vacuum Assisted Polymer Infiltration using 2-Part Epoxy*
  CDC powders produced from Ti_3SiC_2 were placed on a filter paper, which was connected to a vacuum capable of pulling a vacuum. The vacuum was applied and an epoxy resin (Castolite 811-190, LECO) was poured over the CDC layer. Once the excess resin was pulled through the filter paper, the vacuum was stopped and 3 hardener drops were placed on the resin coated CDC. The CDC and epoxy did not wet well and the CDC tended to agglomerate to minimize contact with the epoxy, and despite the presence of excess hardener, the epoxy did not fully cure.

- *Polymer Infiltration using Polysulfone*
  Powder CDC produced from Ti_3SiC_2 was placed on a filter paper which was in turn placed on a filter support connected to a vacuum. The vacuum was applied and a solution of polysulfone was then poured over the CDC layer. The polysulfone solution was made using tetrahydrofuran (THF) (99.9% HPLC grade inhibitor free, Sigma Aldrich) and polysulfone beads (UDEL 1800, Solvay). The CDC and polysulfone mix

well. The vacuum was applied until the THF was fully evaporated. This method was difficult to form a disc with parallel sides for attachment to either a gas or aqueous supply due to the settling of the CDC powder and curing of the polysulfone.

Bulk CDC discs of 25 mm diameter and 3 mm thick were also infiltrated with a polysulfone/THF solution, which was produced using a weight ratio of 1:8. A disc of CDC with a flat surface was attached to vacuum. Drops of THF were added to "wet" the CDC, and were subsequently added until the THF was seen on the vacuum side of the CDC. Three drops of the polysulfone/THF solution were added, followed by THF drops as needed to keep a wet pool of polymer solution on top of the CDC. Drops of polysulfone solution, followed by wetting THF drops were continued until the polymer was noticed on the vacuum side of the CDC. Allowed infiltrated disc to dry overnight. Excess polysulfone was removed from the top and bottom surfaces of the disc using grinding paper until carbon deposits were observed. Although cracks within the CDC were nicely sealed due to the polysulfone infiltration, an aqueous solution was not able to penetrate through the disc, suggesting that micropores were blocked by the polymer as well.

Based on SEM images of both the powder and bulk CDC, it is unlikely for a gas or liquid to permeate the CDC composite membrane because the polysulfone would rap around each individual particle of CDC. The situation of two CDC particles directly in contact with each other was not observed.

- *Supercritical Evaporation*

A polymer solution was measured using 4,4′-methylenebiscyclohexanamine (PACM-20, Air Products), an epoxy resin diglycidyl ether of bisphenol A (EPON 828, Resolution), and THF (Aldrich) solvent. The solution was shaken after weighing the

amine, epoxy, and THF using a 4:1:2 mole ratio of THF/amine/epoxy. CDC powder weighing 0.3g was added and the solution was slightly agitated, upon which the solution color turned a uniform dark gray color. CDC powder was suspended in solution and did not settle to the bottom of the vial within a 15 minute time period, signifying straightforward dispersion. Sample vials were sealed with Teflon tape. The sample was then placed in an oven at 60 °C and stored at that temperature for 1 month. The formed CDC containing gel was dried under supercritical conditions to prevent the pores from being disturbed. A small sample chamber with a controlled flow of liquid CO_2 and temperature was used. The gel was immersed in liquid CO_2, replacing the THF in the gel with liquid CO_2. Once the solvents exchanged, the sample chamber was refreshed with additional liquid CO_2. This flushing process was repeated three times. Once the organic solvent was adequately replaced by liquid CO_2 the temperature of the sample chamber was increased above 31.1 °C, the supercritical temperature of CO_2. CO_2 was carefully removed.

The results of the supercritical evaporation resulted in a sample that did not have connecting CDC particles, but had CDC particles connected by porous polymer based on SEM images. This method, however, would provide an interesting composite with bimodal porosity. This method was performed using equipment in the laboratory of Dr Giuseppe Palmese, Chemical and Biological Engineering, Drexel University.

- *Rolling Technique*

  Modeling a process that was used for the development of electrochemical membranes, a rolling technique was used with CDC and polysulfone (UDEL, Solvay). Two different mixtures of CDC and polysulfone were measured using 44 wt% (batch #1)

and 22 wt% (batch #2) of polysulfone. For each batch, three rolling techniques were used.

Technique 1: Mix polysulfone and CDC together with mortar and pestle, add powder mixture to a silica coated Mylar carrier film, add THF solvent, and then roll the slurry of CDC, polysulfone, and THF.

Technique 2: Mix polysulfone and CDC together with mortar and pestle, add powder to silica coated Mylar carrier film, roll, add THF to rolled sheet.

Technique 3: Mix polysulfone and CDC together with mortar and pestle, roll, remove compressed CDC/polusulfone from silica coated Mylar carrier film to mortar, grind in mortar, add THF, mix, pour slurry onto silica coated Mylar carrier film, and allow THF to evaporate.

The results from the rolling experiments are as follows:

Batch #1, Technique #1: poor adhesion, remained somewhat powdery

Batch #1, Technique #2: created film that had numerous visible pores

Batch #1, Technique #3: created flakes of film rather than continuous piece

Batch #2, Technique #1: poor adhesion, remained somewhat powdery

Batch #2, Technique #2: created flakes of film rather than continuous piece

Batch #2, Technique #3: created flakes of film rather than continuous piece

- *Fiber spinning envelope*

A mat of polyacrulonitrile (PAN) polymer was made by fiber spinning using a voltage of 900 V/cm and a 15 minute spinning time. The CDC powder was deposited in the center of the mat, which was centered on an aluminum foil collection plate. Through a syringe, further PAN polymer was applied on top of the CDC to encase the CDC with the polymer mat. A voltage of 900 V/cm and time of 15 minutes was used to develop

the mat. Once the mat fully encased the CDC, it was found that the CDC was able to move about within the casing and that after minor ruffling, the CDC powder was able to break through the polymer mesh and no longer be contained.

- *Cold Press*

  CDC powder made from Ti_3SiC_2 was placed in a 1 inch circular mold and a pressure of 689 MPa was applied for 5 minutes. Once the pressure dropped to 634 MPa , the remaining pressure was slowly removed to prevent shock fracture. Once removed, the CDC was compressed to an extremely thin and brittle disc which was highly difficult to remove from the mold without fracture.

Vita

EDUCATION: Drexel University, Philadelphia, PA

*Ph. D in Materials Science and Engineering, (*NSF IGERT Fellow) August 2006

B.S. in Materials Science and Engineering, GPA: 3.84/4.0 June 2002

RESEARCH EXPERIENCE: Drexel University, Philadelphia, PA

Dissertation: MAX-Phase Carbide Derived Carbons for Separation Applications

Advisors: Dr. Michel W. Barsoum and Dr. Yury Gogotsi

Additional Research Topics:

- Spontaneous Growth of Soft Metallic Whiskers
- Ti_3SiC_2 as Solid Oxide Fuel Cell Anode
- Synthesis of Zr_2InC in Bulk via Reactive Hot Isostatic Pressing
- Particle Pinned Grain Growth in Aluminum

PATENTS:

- Y. Gogotsi, G. Yushin, **E.N. Hoffman**, M.W. Barsoum, Nanoporous Carbon Membrane Produced from Inorganic Precursors and the Method of Precursor Deposition
- Y. Gogotsi, G. Yushin, **E.N. Hoffman**, M.W. Barsoum, Process for Producing Nanoporous Carbide Derived Carbon with Large Specific Surface Area
- M.W. Barsoum, **E.N. Hoffman** and R.D. Doherty, Reduction of Spontaneous Metal Whisker Formation.

HONORS AND AWARDS:

- NSF Integrative Graduate Education and Research Traineeship (IGERT) 2004-Present
- *Young Member Award*, ASM Philadelphia Chapter, 2005
- *Outstanding Graduate Student Award*, Drexel University, 2005
- Unsolicited coverage of journal article, *Physical Review Letters*, **93** [20], 2004, printed *Physics Today* February 2005, Drexelink Newsletter, and Materials Science and Engineering Department Annual Report 2004-2005
- North American Membrane Society (NAMS) conference travel grant 2005
- American Ceramics Society (ACerS) *Graduate Excellence in Materials Science (GEMS) Sapphire Award* 2005
- SEM micrograph published back-cover of *Journal of the American Ceramic Society,* **87** [8], 2004
- ACerS travel grant to Pacific Rim Conference in Nagoya, Japan, 2003
- *National Science Foundation Fellowship*, Honorable Mention 2003

PUBLICATIONS

- G. Yushin, **E.N. Hoffman**, M.W. Barsoum, Y. Gogotsi, Carol A. Howell, Susan R. Sandeman, Gary J. Phillips, Andrew W. Lloyd and Sergey V. Mikhalovsky "Mesoporous carbide-derived carbon with porosity tuned for efficient adsorption of cytokines", *Biomaterials* (accepted for publication) (2006)
- B. Manoun, S.K. Saxena, G. Hug, A. Ganguly, **E.N. Hoffman,** and M.W. Barsoum. "Synthesis and Compressibility of $Ti_3(Al_{1.0}Sn_{0.2})C_2$ and a New Phase, $Ti_3Al(C_{0.5},N_{0.5})_2$", *Physical Review B* (submitted for review).
- **E.N. Hoffman**, G. Yushin, M.W. Barsoum, and Y. Gogotsi, "Synthesis of Carbide-Derived Carbon by Chlorination of Ti_2AlC", *Chem. Mater*. **17**, (2005), 2317-2322
- **E.N. Hoffman**, M.W. Barsoum, W. Wang, R.D. Doherty, and A. Zavaliangos, "On the Spontaneous Growth of Soft Metallic Whiskers", *Proceedings of the 51st IEEE Holm Conference on Electrical Contacts* (2005), 121-126.
- G. Yushin, **E.N. Hoffman**, A. Nikitin, H. Ye, M.W. Barsoum, and Y. Gogotsi. "Synthesis of Carbide Derived Carbon by Chlorination of Titanium Silicon Carbide", *Carbon*, **43** [10] (2005), 2075-2082.
- M.W. Barsoum, **E.N. Hoffman**, R.D. Doherty, S. Gupta and A. Zavaliangos, "Driving Force and Mechanism of Spontaneous Metal Whisker Formation", *Physical Review Letters*, **93** [20], 2004
- R. Doherty, **E.N. Hoffman**, C. Hovanec, A. Lens "Abnormal Grain Coarsening and Its Possible Relationship with Particle Limited Normal Grain Coarsening" *Materials Science Forum*, **467-470,** (2004) 843-852.